

Radiative Properties of Pair-instability Supernova Explosions

Luc Dessart,^{1,2*} Roni Waldman,³ Eli Livne,³ D. John Hillier,⁴ Stéphane Blondin,^{1,5}

¹: Aix Marseille Université, CNRS, LAM (Laboratoire d'Astrophysique de Marseille), UMR 7326, 13388, Marseille, France

²: TAPIR, Mail code 350-17, California Institute of Technology, Pasadena, CA 91125, USA

³: Racah Institute of Physics, The Hebrew University, Jerusalem, 91104, Israel

⁴: Department of Physics and Astronomy, University of Pittsburgh, 3941 O'Hara Street, Pittsburgh, PA 15260, USA

⁵: Centre de Physique des Particules de Marseille (CPPM), Aix-Marseille Université, CNRS/IN2P3, Marseille, France

Accepted 2012 October 22. Received 2012 October 19; in original form 2012 August 14

ABSTRACT

We present non-LTE time-dependent radiative-transfer simulations of pair-instability supernovae (PISNe) stemming from red-supergiant (RSG), blue-supergiant (BSG) and Wolf-Rayet (WR) star rotation-free progenitors born in the mass range $160\text{--}230\text{ M}_{\odot}$, at 10^{-4} Z_{\odot} . Although subject to uncertainties in convection and stellar mass-loss rates, our initial conditions come from physically-consistent models that treat evolution from the main-sequence, the onset of the pair-production instability, and the explosion phase. With our set of input models characterized by large ^{56}Ni and ejecta masses, and large kinetic energies, we recover qualitatively the Type II-Plateau, II-peculiar, and Ib/c light-curve morphologies, although they have larger peak bolometric luminosities ($\sim 10^9$ to 10^{10} L_{\odot}) and a longer duration ($\sim 200\text{ d}$). We discuss the spectral properties for each model during the photospheric and nebular phases, including Balmer lines in II-P and II-pec at early times, the dominance of lines from intermediate-mass-elements (IMEs) near the bolometric maximum, and the strengthening of metal line blanketing thereafter. Having similar He-core properties, all models exhibit similar post-peak spectra that are strongly blanketed by Fe II and Fe I lines, characterized by red colors, and that arise from photospheres/ejecta with a temperature of $\lesssim 4000\text{ K}$. Combined with the modest line widths after bolometric peak, these properties contrast with those of known superluminous SNe suggesting that PISNe are yet to be discovered. Being reddish, PISNe will be difficult to observe at high redshift except when they stem from RSG explosions, in which case they could be used as metallicity probes and distance indicators.

Key words: radiation hydrodynamics – stars: atmospheres – stars: supernovae – stars: evolution – stars: supernovae: individual: 2007bi, 2006gy

1 INTRODUCTION

About a decade ago, numerical simulations of star formation revealed that the first generation of stars may have been super-massive (Bromm et al. 2002), holding great promise to discover them, not as stars, but rather through their catastrophic explosions. Barkat et al. (1967) and Rakavy & Shaviv (1967) proposed that for stars sufficiently massive the production of e^-e^+ pairs from γ -ray annihilation would lead successively to an implosion, a thermonuclear runaway, and an explosion leaving no remnant behind. These events are termed pair-instability supernovae (PISNe). In the coming decade, the opportunity to identify PISNe and study them in detail may be realized with new observatories such as LSST and JWST (Scannapieco et al. 2005; Hummel et al. 2012). However, there is considerable uncertainty and speculation concerning

the first generation of massive stellar objects, impacting our understanding of their formation, their evolution, and their explosion.

Recent simulations for the formation of the first stars has significantly altered the original picture. The initial mass function seems no longer to be heavily biased towards super-massive stars. Instead, it stretches down to lower masses, even very low masses (Caffau et al. 2012), perhaps exhibiting a bimodal distribution (Stacy et al. 2011, 2012; Clark et al. 2011). Binaries should also be created (Stacy et al. 2010), although the binary fraction is largely unknown. Simulations including feedback, in particular in the form of UV radiation, suggest that the circumstellar disk feeding mass into the primordial star is evaporated soon after the onset of steady thermonuclear burning. This feedback leads to the truncation of mass accretion and sets an upper mass limit for the newly-formed star of $\sim 30\text{ M}_{\odot}$ (Hosokawa et al. 2011). Theoretically, primordial star formation does not seem to differ significantly from present-day star formation. Paradoxically, it fails to explain the existence in the Local Universe of super-massive stars like $\eta\text{ Car}$

* email: Luc.Dessart@oamp.fr

(Davidson & Humphreys 1997; Hillier et al. 2001), massive stars in the Galactic centre (Figer et al. 2002; Martins et al. 2008), or the spectacular R136 nursery (Crowther et al. 2010). Since super-massive stars in the Local Universe systematically belong to dense star clusters, they may form not in isolation but instead dynamically and chaotically from merger events (e.g., Bonnell & Bate 2005; Vanbeveren et al. 2009; Pan et al. 2012b).

More generally, the nature of superluminous SNe remains perplexing. The interaction between two separate shells, which converts kinetic energy to thermal and radiative energy, is one way to boost the luminosity of a SN, because standard SNe typically have a hundred times more kinetic energy than time-integrated luminosities. Another way of producing a bright display is by depositing magnetar radiation into the SN ejecta (Maeda et al. 2007; Kasen & Bildsten 2010; Woosley 2010). The energy lost by the magnetar leads to the spin down of the magnetar which eventually quenches the magnetar radiation. For a dipole field, the spin-down time scale is $t_{\text{sp}} \sim 4.8 B_{15}^{-2} P_{10}^2$ d, where B_{15} is the magnetic strength in units of 10^{15} G and P_{10} is the rotation period P in units of 10 ms. Depending on the magnetar parameters, its spin-down timescale may be comparable to the decay timescale of ^{56}Ni , making it an attractive substitute for models that require a larger-than-average production of ^{56}Ni for powering luminous SNe. While a PISN may synthesize a maximum of $57 M_{\odot}$ of ^{56}Ni (Heger & Woosley 2002), it is unclear how much a “standard” core-collapse SN can produce. This reflects the poorly known core properties at the time of death, and the viability of the neutrino and magneto-rotational explosion mechanisms. The collapsar model is one instance where copious amounts of ^{56}Ni may be produced (Woosley 1993), but the required core compactness to form such collapsars seem far more rarely matched by stellar evolution models, favoring instead the formation of proto-magnetars (Dessart et al. 2012d).

Restricting our focus to very low metallicity environments the ansatz of the current study is that super-massive stars do form, populating the mass range $140\text{--}260 M_{\odot}$. Provided they do not lose much mass during the hydrogen-burning stage, they form a helium core with a mass in the range $64\text{--}133 M_{\odot}$ that should experience the pair-production instability and lead to a thermonuclear explosion that completely disrupts the star (Heger & Woosley 2002; Waldman 2008). How often this occurs is completely speculative as it depends on the unknown formation rate of the progenitors as well as their evolution. A major component of this uncertainty is mass loss since it determines whether the star will explode as an extended blue-supergiant (BSG), as a very extended red-supergiant (RSG) star, or instead as a very compact Wolf-Rayet (WR) star. This, in turn, impacts the supernova (SN) light curve morphology and thus the potential detectability and reliable identification of these events (Scannapieco et al. 2005; Kasen et al. 2011). As we discuss here, a H-rich PISN from a RSG star at $10^{-4} Z_{\odot}$ leaves little ambiguity about the origin of the event while connecting a superluminous Type Ic event with a H-deficient PISN is more challenging. It is unclear today if we have seen either H-rich or H-deficient PISNe (Dessart et al. 2012c).

Mass-loss in metal poor massive stars is highly uncertain. Baraffe et al. (2001) found that metal-poor massive stars are pulsationally stable and, based on this analysis, should die with their hydrogen envelope. The metallicity dependence of radiation driving in massive-star winds suggests that this other form of mass loss, critical for OB and WR stars at solar metallicity, should be largely inhibited at very low metallicity (Castor et al. 1975). As is quite typical for proto-stellar collapse in star formation, the col-

lapsed core is endowed with a large amount of angular momentum at birth (Stacy et al. 2011), which may affect its evolution in a number of ways (Hirschi et al. 2004a; Hirschi 2007; Heger & Woosley 2010; Chatzopoulos & Wheeler 2012; Yoon et al. 2012). For example, by increasing the oxygen core mass, fast rotation can lower the minimum main-sequence mass needed to encounter the pair-production instability (Chatzopoulos & Wheeler 2012), thereby affecting the ^{56}Ni -mass to ejecta-mass ratio and the resulting PISN radiation properties (Dessart et al. 2012c). High luminosity poses a severe strain on the hydrostatic equilibrium of stars (Joss et al. 1973), especially near break-up rotation speeds (Maeder & Meynet 2000), establishing ideal conditions for centrifugally-driven mass loss (a disk) and/or a continuum-driven wind (Owocki et al. 2004). In this context, radiation- and/or rotation-driven mass loss may in fact compete with the episodic pulsations expected to occur in stars with a helium-core mass in the range $40\text{--}63 M_{\odot}$ (Heger & Woosley 2002; Woosley et al. 2007a).

Currently, the most promising PISN candidate is SN2007bi (Gal-Yam et al. 2009; Young et al. 2010), although this association raises several issues. The observations capture only the light-curve peak and beyond, making the explosion time uncertain, compromising the inference of the ejecta mass and ^{56}Ni mass. Furthermore, SN2007bi took place in an environment of $0.2\text{--}0.3 Z_{\odot}$; a hydrogen-deficient PISN at such a high metallicity seems difficult to accommodate with stellar evolution (Langer et al. 2007).¹ The nebular spectral analysis of Gal-Yam et al. (2009) suggests a large ejecta mass, i.e., much larger than in standard core-collapse SNe, but the accuracy of this inference does not unambiguously support a PISN — within the errors these masses are compatible with a progenitor that would not experience the pair-production instability.

The alternative core-collapse scenario of Moriya et al. (2010) for SN2007bi requires extreme properties, which may be acceptable given the scarcity of these events, but it is also in contradiction with the environmental metallicity. Their proposed model yields a $36 B$ ($1B \equiv 1\text{Bethe} = 10^{51}$ erg) ejecta kinetic energy, which, combined with the binding energy of the progenitor, requires the remarkable extraction of $\lesssim 50\%$ of the gravitational energy of a typical neutron star.

Kasen & Bildsten (2010) and Kasen et al. (2011) have fueled this controversy further by obtaining equally satisfactory fits to the SN 2007bi bolometric light curve using either a magnetar model or a PISN model. In contrast, in a recent study based primarily on the simulations presented here (Dessart et al. 2012c), we emphasized that PISN models systematically have red colors and narrow lines after light-curve peak — properties that are in strong contradiction with the observations of SN2007bi. Dessart et al. (2012c) suggest that delayed energy injection, as from a magnetar, into a lower mass ejecta would be more amenable to producing both blue colors and broad emission lines typical of such superluminous SNe.

An independent problem with PISNe, if they were to be the first chemical nurseries in the Universe, is that their distinctive nucleosynthetic yields (Heger & Woosley 2002; Umeda & Nomoto 2002; Chieffi & Limongi 2004) are in apparent contradiction with those inferred from extremely metal poor stars (Cayrel et al. 2004; Cohen et al. 2008). Such abundance studies suggest that the metals

¹ The lack of spatial resolution prevents the accurate inference of the metallicity at the actual site of SN2007bi, so one cannot exclude the possibility that the actual primordial cloud from which the progenitor of SN2007bi formed may be of lower metallicity than the inferred value of $0.2\text{--}0.3 Z_{\odot}$. In that case, a Type Ic PISN may not be excluded.

arose from “standard” core-collapse explosion of stars of moderate mass (Heger & Woosley 2010), although a contrived scenario involving a combination of SN with strong fallback and highly-energetic SNe was proposed by Nomoto et al. (2006).

In this work, we perform a quantitative study of PISN explosions arising from RSG, BSG, and WR star progenitors, investigating their photometric and spectroscopic signatures, and documenting in more details the results presented by Kasen et al. (2011) and Pan et al. (2012a). We allow for non-LTE at all times and include non-thermal processes, which are not just important for exciting helium atoms in SNe Ib (Lucy 1991) – they directly affect all species by driving level populations away from LTE. They also indirectly affect the thermodynamic state of the gas by channeling a fraction of the decay energy into excitation and ionization of ions and atoms rather than into heat. We compute the full time-dependent radiative transfer within the non-LTE framework, allowing the computation of the spectral evolution from the photospheric to the nebular phase. Multi-band light curves are obtained by integrating the resulting spectra over specified bandpasses. This unique approach allows to compute light curves and spectra simultaneously and with the same level of complexity. It also allows us to start from physically-consistent ejecta resulting from stellar evolution and explosion modelling. This detailed study aims at providing the key spectroscopic signatures of the three possible types of PISN explosions, with the hope of identifying the critical signatures that would help lifting the ambiguities surrounding the association of PISNe with events like SN 2007bi (Dessart et al. 2012c).

In the next section, we review the numerical setup for our calculations, including the pre-SN evolution from the main sequence (Sect. 2.1), the pair-instability explosion mechanism (Sect. 2.2), and the setup for the radiative-transfer calculations presented in this work (Sect. 2.3). We then describe the bolometric light curve of our PISN models, and compare them with those arising from “standard” core-collapse SN explosions of 15–25 M_{\odot} RSG, BSG, and WR stars evolved as single or binary stars (Sect. 3). In Sect. 4 we connect these light-curve properties to those at the photosphere. We then describe in detail the spectral evolution for each group of progenitors during the PISN photospheric and nebular phases (Sect. 5). We compare our simulations to PISN candidates SN 2007bi and SN 2006gy in Sect. 6; additional information, in particular the proposition that the SN 2007bi light curve is more compatible with magnetar power, can be found in Dessart et al. (2012c). We finally advocate the potential use of PISN explosions as a diagnostic of the environmental metallicity in Sect. 7. We summarize our results and discuss their implications in Sect. 8. To limit the length of the main body of the paper, we provide additional results in an appendix (provided as online material only), covering in more detail the evolution of the ejecta properties (e.g., ionization state and optical depth; Appendix A), the atomic data and model atoms (Appendix B), and the dependency of our results on model atoms (Appendix C). We finally provide tabulated values for the luminosity and magnitudes for all time sequences (Appendix D).

2 PRE-SN EVOLUTION, EXPLOSION, AND MODEL SETUP

The work presented in this paper was produced in several independent steps. First, a large grid of massive-star progenitors was evolved from the main sequence until all models underwent collapse due to the pressure deficit following pair production. These simulations were then remapped into a 1D radiation-

hydrodynamical code, with allowance for (explosive) nuclear burning and radiation transport, and followed through the explosion phase for a few years. A detailed discussion of the results from these two steps will be presented in a separate paper (Waldman et al., in prep.). Here, we focus on a subset of four PISN models from this large grid of models, and specifically arising from the explosion of a RSG star, two BSG stars, and a bare He core. This paper discusses the evolution of these ejecta and their radiation taking into account both non-LTE and time-dependent effects. In Sect. 2.1–2.2, we present briefly the first two steps and then present the setup for the radiative-transfer calculations in Sect. 2.3. Additional information is provided in the Appendix.

2.1 pre-SN evolution

Using the 1-D stellar-evolution code MESA (Paxton et al. 2011), we perform calculations of super-massive stars from the main-sequence until the onset of the pair-production instability. We focus on progenitors with main-sequence masses between 160 and 230 M_{\odot} , adopt a metallicity of $10^{-4} Z_{\odot}$ and neglect rotation. In this paper, we focus on a small sample of PISN progenitors that synthesize a large amount of ^{56}Ni suitable to produce a superluminous SN. We thus ignore the less massive progenitors that encounter the pair-production instability but produce low explosion energies with a small ^{56}Ni mass (see, e.g., Kasen et al. 2011). We treat convection by the well known mixing length theory (MLT) using the Schwarzschild criterion and a mixing length parameter of 1.6, and ignore convective overshoot. During core hydrogen and helium burning the “basic” 8-species nuclear reaction network of MESA is used, including the following isotopes: ^1H , ^3He , ^{12}C , ^{14}N , ^{16}O , ^{20}Ne , ^{24}Mg . From the onset of core carbon burning, the nuclear reaction network is expanded. For the He100 model (see details below) the α -chain elements are added, while for the other models, in order to account for more nuclei that may manifest in the resulting spectra, we use a more elaborate nuclear reaction network provided with MESA. In addition to the α -chain elements, it includes the intermediate elements linking those through $(\alpha, p)(p, \gamma)$ reactions, namely: n, p, ^3He , ^{12}C , ^{13}C , ^{14}N , ^{16}O , ^{19}F , ^{20}Ne , ^{23}Na , ^{24}Mg , ^{27}Al , ^{28}Si , ^{31}P , ^{32}S , ^{35}Cl , ^{36}Ar , ^{39}K , ^{40}Ca , ^{43}Sc , ^{44}Ti , ^{47}V , ^{48}Cr , ^{51}Mn , $^{52,54,56}\text{Fe}$, $^{55,56}\text{Co}$, ^{56}Ni . Pair creation is treated in the equation of state used in MESA, as well as in $\dot{\text{I}}\text{d}$ (see below and, e.g., Cox & Giuli 1968).

A crucial ingredient in the models is mass-loss. Apart from the He100 model, which was evolved without mass loss, we use two standard mass-loss prescriptions that are functions of the effective temperature, T_{eff} , of the stellar model. For cool stars, defined by $T_{\text{eff}} < 10^4$ K, we use the formula of de Jager et al. (1988), multiplied by the metallicity-dependent factor $(Z/Z_{\odot})^{0.5}$ (Kudritzki et al. 1987). For hotter stars, we use the formula of Vink et al. (2001), which contains a $(Z/Z_{\odot})^{\alpha}$ metallicity dependence, where $0.64 < \alpha < 0.69$ depending on the effective temperature. Using these mass-loss prescriptions, the pair-instability is encountered when the star is a RSG. Our representative model for this scenario is R190. None of our models, evolved from the main sequence, lose enough mass to become a WR star, defined by $X_{\text{surface}} < 0.4$ and $T_{\text{eff}} > 10^4$ K. This is expected – at the low metallicity of $10^{-4} Z_{\odot}$ adopted here, radiation-driven winds will be significantly inhibited during the object’s life as an O star.

To allow for uncertainties in mass loss (as well as for giant-eruptions, such as that associated with η Car, which are not covered by the above procedures), we perform additional simulations. To mimic the possibility of a stronger mass loss, we artificially

Table 1. Summary of the composition, in solar masses, for each model immediately before the onset of the pair-instability explosion.

Model	M_i	M_f	^1H	^4He	^{12}C	^{16}O	^{20}Ne	^{24}Mg	^{27}Al	^{28}Si
R190	190.0	164.1	23.6	46.1	5.3	78.4	8.6	2.2	0.06	0.05
B190	190.0	133.9	5.7	33.8	5.3	78.4	8.6	2.2	0.06	0.05
B210	210.0	146.7	3.7	30.8	5.9	92.5	10.8	3.0	0.08	0.06
He100	100.0	100.0	0.0	8.5	5.6	75.4	8.1	2.1	0.00	0.07

truncate the hydrogen envelope of the RSG progenitor immediately before explosion, reducing the total mass and surface radius, and producing a BSG progenitor (models B190 and B210). To mimic an even greater mass-loss rate by means not understood today (although mass-transfer in a binary may be an option), we also evolve objects directly from a bare helium core (model He100). We summarize the properties for these four models in Table 1. In our nomenclature, RX, BX, and HeX refer to explosions as RSG, BSG, and He (WR) stars, where X is the initial mass.

The evolution is generally followed using MESA’s hydrostatic mode. When an hydrodynamic instability is encountered, which occurs invariably at central carbon exhaustion, the code is automatically switched to the hydrodynamic mode, and the run is continued until ^{20}Ne is exhausted at the stellar center. At this time, before ^{16}O burning turns on, the profile is remapped into the 1D radiation hydrodynamical code VID (Livne 1993). We find that the nucleosynthetic outcome is insensitive to the remapping epoch between hydrodynamic instability and neon exhaustion, but does change for later remapping epochs, mainly due to differences in the reaction networks used in the two codes.

Our models typically reside on the main sequence for about 2.5 Myr, gradually cooling from an O-star of about 80,000 K and $\sim 10 R_\odot$, finally settling by the end of core helium burning, which lasts about 0.2–0.3 Myr, as a K-type supergiant of about 4300 K and $4000\text{--}5000 R_\odot$. Throughout its evolution, the luminosity of the star does not experience dramatic changes – it is $3\text{--}4 \times 10^6 L_\odot$, on the ZAMS, gradually growing by about a factor of 1.5 towards the end of the main sequence, and remaining virtually constant through the rest of the evolution. The star burns hydrogen and helium in shells for a period on the order of 10^4 yr, while its core contracts, until carbon is ignited at the center at $T_c \sim 10^9$ K, $\rho_c \sim 2 \times 10^4 \text{ g cm}^{-3}$. Since the carbon mass fraction is relatively low (on the order of 0.06) the energy release cannot prevent the continued contraction of the core. Central carbon is exhausted in less than a year. An hydrodynamic instability, which typically starts at $T_c \sim 1.2 \times 10^9$ K and $\rho_c \sim 6 \times 10^4 \text{ g cm}^{-3}$, then occurs and this is followed by central neon exhaustion that takes several hours to be achieved. At this stage $T_c \sim 2 \times 10^9$ K and $\rho_c \sim 4 \times 10^5 \text{ g cm}^{-3}$, while infalling velocities typically reach several 100 km s^{-1} . The main properties of the models at the onset of the hydrodynamic instability are given in Table 1. We also show a Kippenhahn diagram for the RSG model R190 that illustrates the evolution of the internal structure and surface properties prior to the pair-production instability (Fig. 1).

With our small grid, we thus cover the 3 different stellar types under which massive stars may explode, i.e., as RSG, BSG, or WR stars, resulting in explosions as SNe II-P, II-pec, and Ib/c. The only configuration not considered here is SN IIn, which could stem from interaction between consecutively ejected shells following pair instability pulses (Woosley et al. 2007b).

Table 2. Summary of the main properties for the four hydrodynamical input models B190, R190, B210, and He100 explored in this study. All CMFGEN models are run assuming either local energy deposition, or non-local energy deposition (model name is then appended by “NL”).

Model	Type	M_i [M_\odot]	M_f [M_\odot]	R_* [R_\odot]	E_{kin} [B]	M_{ejecta} [M_\odot]	$M_{^{56}\text{Ni}}$ [M_\odot]
B190(NL)	BSG	190.0	133.9	186	34.5	133.9	2.99
R190(NL)	RSG	190.0	164.1	4044	33.2	164.1	2.63
B210(NL)	BSG	210.0	146.7	146	65.9	146.7	21.3
He100(NL) ^a	WNE	100.0	100.0	1	37.6	100.0	5.02
He100K ^b	WNE	100.0	100.0	...	40.9	100.0	5.00

Notes: For all stellar-evolution models, the environmental metallicity is $10^{-4} Z_\odot$. Type stands for the progenitor stellar type. ^a: The He-star model is run with two different sets of model atoms: He100 uses the same model atoms as B190, R190, and B210. He100ion1 is identical in all ejecta and model parameters as He100 except that it is modeled with the additional neutral species Mg I, Si I, S I, and Ca I (Appendix C). ^b: Corresponding properties of the He100 model of Kasen et al. (2011), which we name He100K to avoid confusion.

2.2 Explosion

To model the explosion phase, we use a more extended reaction network, which in addition allows for (α, n) reactions up to calcium, for (n, γ) reactions up to nickel, and for the radioactive decay of $^{56}\text{Ni} \rightarrow ^{56}\text{Co} \rightarrow ^{56}\text{Fe}$. In total, we include the isotopes: n, p, ^4He , ^{12}C , ^{14}N , ^{16}O , $^{20\text{--}22}\text{Ne}$, ^{23}Na , $^{23\text{--}26}\text{Mg}$, ^{27}Al , $^{27\text{--}30}\text{Si}$, ^{31}P , $^{31\text{--}34}\text{S}$, ^{35}Cl , $^{35\text{--}38}\text{Ar}$, ^{39}K , $^{39\text{--}42}\text{Ca}$, ^{43}Sc , $^{44\text{--}46}\text{Ti}$, ^{47}V , $^{48\text{--}50}\text{Cr}$, ^{51}Mn , $^{52\text{--}54,56}\text{Fe}$, $^{55\text{--}56}\text{Co}$, $^{56\text{--}58}\text{Ni}$, ^{59}Cu , ^{60}Zn .

Following central neon exhaustion, oxygen is ignited, and consumed in less than a minute. At this stage the typical central conditions are $T_c \sim 3.5 \times 10^9$ K and $\rho_c \sim 10^6 \text{ g cm}^{-3}$, while the infall velocities reach several 1000 km s^{-1} . In the subsequent ~ 10 s, central silicon is exhausted, and the implosion turns into an explosion. The central conditions reached at bounce depend on the mass of the model and the binding energy of the star, but are typically $T_c \sim 3.5\text{--}6 \times 10^9$ K and $\rho_c \sim 2\text{--}6 \times 10^6 \text{ g cm}^{-3}$.

During this explosive-burning phase most of the energy is released by oxygen burning, and some by neon and carbon burning. For example, in our $190 M_\odot$ model, $\sim 40 M_\odot$ of fuel are burnt, split between $30 M_\odot$ of oxygen, $7 M_\odot$ of neon, and $4 M_\odot$ of carbon, with a total energy release of 44 B. This fuel is converted primarily into silicon ($20 M_\odot$) and sulphur ($13 M_\odot$), the remainder being argon ($3 M_\odot$), calcium ($2 M_\odot$) together with $\sim 3 M_\odot$ of ^{56}Ni . In contrast, our heavier model B210 burns about 70% more fuel, namely $50 M_\odot$ of oxygen, $9 M_\odot$ of neon, and $5 M_\odot$ of carbon, releasing in the process 75 B. This moderately increases the production of IMEs ($23 M_\odot$ of silicon, $16 M_\odot$ of sulphur, $4 M_\odot$ of argon, and $3 M_\odot$ of calcium), but dramatically increases the ^{56}Ni production to $21 M_\odot$.

The energy liberated through explosive burning causes a huge increase in the ejecta internal energy (in the form of radiation) and kinetic energy. As the envelope expands and cools, radiative pressure gradients accelerate the material to its asymptotic velocity on timescales of hours to days. The energy lost to unbind the star is considerable, on the order of 10 B in all PISN models. Asymptotically, the ejecta kinetic energy is 34.5 B for model B190, 33.2 B for model R190, 65.9 B for model B210, and 37.6 B for model He100 (Table 2). The mass-weighted average velocity for each model is, in the same order, 4200, 4000, 6100, and 5500 km s^{-1} — this value can be used to infer a representative ejecta kinetic energy (that differs from the exact value by $\lesssim 30\%$) of 23, 26, 54, and 30 B.

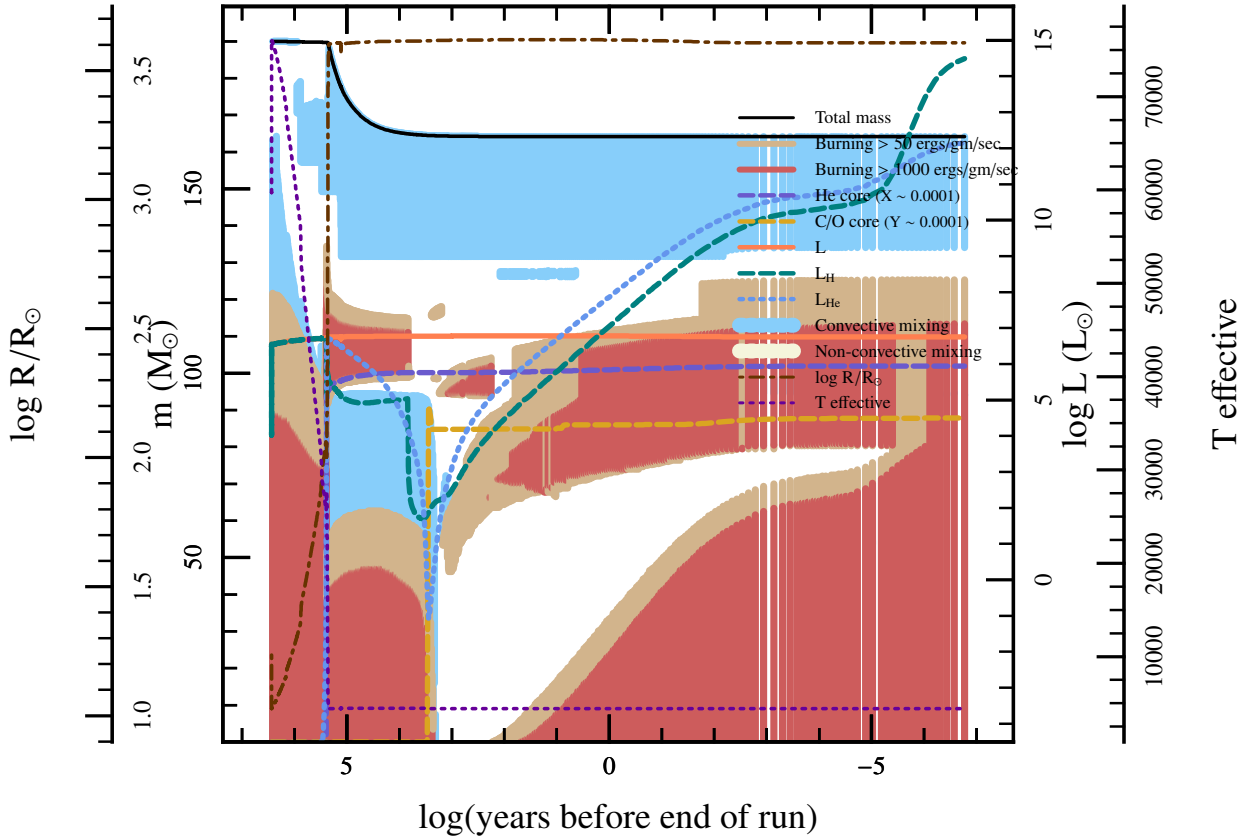


Figure 1. Kippenhahn plot of the $190 M_{\odot}$ RSG model (i.e., R190), showing burning and convective regions, core sizes, mass, luminosity, radius and effective temperature as a function of the remaining time before the onset of the pair-production instability. The “luminosities” L_H and L_{He} correspond to the nuclear-energy generation rates associated with H and He burning — there is also a strong neutrino luminosity (not shown here). Convective mixing refers to convective regions *per se*, while non-convective mixing corresponds to regions where semi-convection, overshoot and/or thermohaline mixing occur.

Table 3. Summary of the chemical composition in ejecta models B190, R190, B210, and He100, immediately after explosive nucleosynthesis stops and prior to decay of unstable isotopes (specifically ^{56}Ni). We limit the table entries to H and He, CNO elements, the main IMEs, and finally Fe, Co, and Ni. The total mass of ^{56}Ni synthesized in the explosion is given in Table 2. The top half of the table shows the cumulative yields, and the bottom half the mass fractions at the progenitor surface. The ^{56}Ni surface mass fraction is zero for all models. All models assume an original metallicity of $10^{-4} Z_{\odot}$. Numbers in parenthesis correspond to powers of ten.

Model	M_H [M_{\odot}]	M_{He} [M_{\odot}]	M_C [M_{\odot}]	M_N [M_{\odot}]	M_O [M_{\odot}]	M_{Ne} [M_{\odot}]	M_{Mg} [M_{\odot}]	M_{Si} [M_{\odot}]	M_S [M_{\odot}]	M_{Ar} [M_{\odot}]	M_{Ca} [M_{\odot}]	M_{Fe} [M_{\odot}]	M_{Co} [M_{\odot}]	M_{Ni} [M_{\odot}]
R190	2.36(1)	4.53(1)	1.06(0)	5.06(-3)	4.81(1)	2.03(0)	2.87(0)	1.96(1)	1.30(1)	2.69(0)	2.36(0)	1.81(-1)	5.09(-3)	2.64(0)
B190	5.72(0)	3.30(1)	1.05(0)	5.56(-3)	4.81(1)	1.99(0)	2.81(0)	1.96(1)	1.31(1)	2.72(0)	2.39(0)	2.03(-1)	2.53(-3)	3.01(0)
B210	3.72(0)	3.04(1)	6.73(-1)	7.35(-3)	3.96(1)	1.43(0)	2.49(0)	2.34(1)	1.58(1)	3.52(0)	3.19(0)	4.35(-1)	6.15(-4)	2.15(1)
He100	5.22(-7)	7.91(0)	1.36(0)	5.05(-3)	4.36(1)	2.11(0)	2.52(0)	1.94(1)	1.27(1)	2.54(0)	2.41(0)	2.67(-1)	6.27(-3)	5.04(0)
Model	X_H	X_{He}	X_C	X_N	X_O	X_{Ne}	X_{Mg}	X_{Si}	X_S	X_{Ar}	X_{Ca}	X_{Fe}	X_{Co}	X_{Ni}
R190	5.93(-1)	4.07(-1)	1.23(-7)	1.10(-6)	3.89(-7)	1.74(-7)	6.47(-8)	6.99(-8)	3.65(-8)	1.02(-8)	6.44(-9)	1.40(-7)	3.43(-10)	7.32(-9)
B190	5.93(-1)	4.07(-1)	1.23(-7)	1.10(-6)	3.89(-7)	1.74(-7)	6.47(-8)	6.99(-8)	3.65(-8)	1.02(-8)	6.44(-9)	1.40(-7)	3.43(-10)	7.32(-9)
B210	5.78(-1)	4.22(-1)	1.14(-7)	1.14(-6)	3.48(-7)	1.74(-7)	6.47(-8)	6.99(-8)	3.65(-8)	1.02(-8)	6.44(-9)	1.40(-7)	3.43(-10)	7.32(-9)
He100	1.00(-15)	1.00(0)	3.37(-7)	9.87(-8)	9.16(-7)	1.74(-7)	2.76(-7)	6.99(-8)	3.65(-8)	1.02(-8)	6.44(-9)	1.41(-7)	3.43(-10)	7.32(-9)

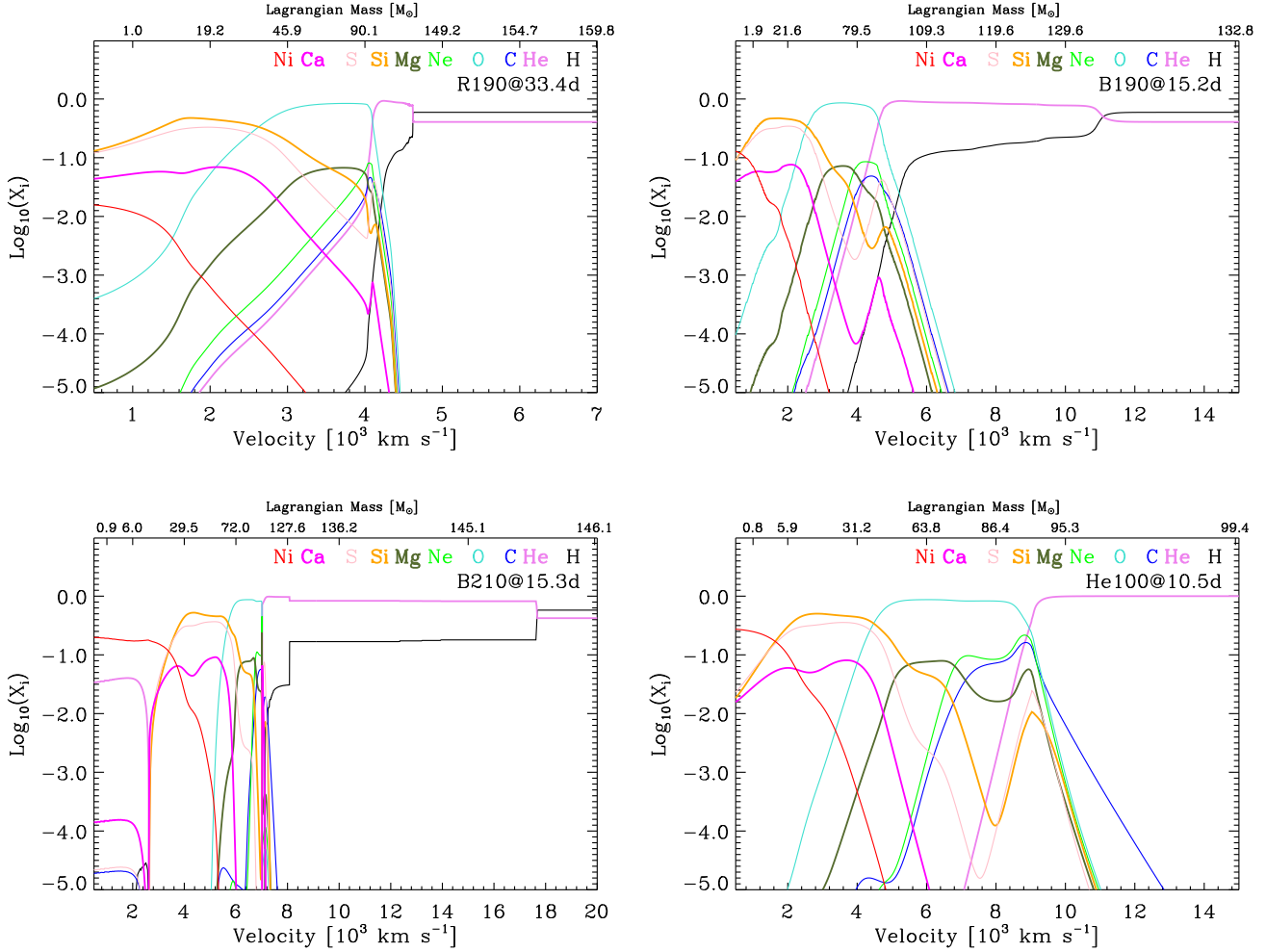


Figure 2. Illustration of the chemical stratification in velocity space (bottom axis) and in mass space (top axis) for the four models discussed in this study (B190: Top left; R190: Top right; B210: Bottom left; He100: Bottom right). The stratification shown is not that of the original models – rather we illustrate the models used as input for CMFGEN in which the composition gradients were softened (except for B210). For better visibility, we limit the range and thus do not show the outer (homogeneous) regions. We also only show a selection of important species, rather than all species included in the calculations.

The yields and the chemical stratification are described in Table 3 and Fig. 2. Although PISNe are thermonuclear explosions, the bulk of the burning takes place in the inner envelope of the progenitor, yielding a chemical stratification more reminiscent of core-collapse Type Ic SNe: The ^{56}Ni is produced at the base of the ejecta, remains confined to the lowest expanding material with velocities less than 4000 km s^{-1} (Fig. 2), and the decay energy has to diffuse from there through the overlying mass to influence the outer ejecta and the light curve.

The density profiles for each model, at the start of the radiative-transfer simulations, are shown in Fig. 3. We stitch an outer density region to all models to ensure an optically-thin outer boundary. With this procedure, the outer ejecta velocity for each model is 42000 km s^{-1} (B190), 24000 km s^{-1} (R190), 50000 km s^{-1} (B210), and 52000 km s^{-1} (He100). The structure for model He100 is quite smooth, with a density exponent of ~ 8 beyond 5000 km s^{-1} . There is a fair amount of structure in the density profiles for the BSG models and even more so in the RSG model, in part associated with the formation and propagation of

reverse shocks at shell interfaces and exacerbated by the 1-D treatment.

Hydrodynamical instabilities in PISNe have been investigated by Joggerst & Whalen (2011). They find that mixing in Pop III $150\text{--}250 M_{\odot}$ SNe explosions is negligible compared to that obtained in $15\text{--}40 M_{\odot}$ Pop II counterparts, although their investigation does not contain H-deficient compact progenitors and they treat nuclear burning through an initial phase performed in 1D. More recently, Chen et al. (2012) have repeated such simulations and found that the treatment of nuclear burning in multi-D can enhance the level of mixing significantly. Since this issue is not settled, we decided to soften the composition discontinuities by mixing over adjacent mass shells, producing a mild smearing of the (high-resolution) 1D input structures produced by 1d. This is done more as a convenience than aimed at describing the physical effect of mixing seen in multi-D simulations. The chemical stratification of the models used as input to CMFGEN is shown in Fig. 2. Based on the present work, we however anticipate that mixing will not significantly alter the observables we describe here. Non-local energy deposition

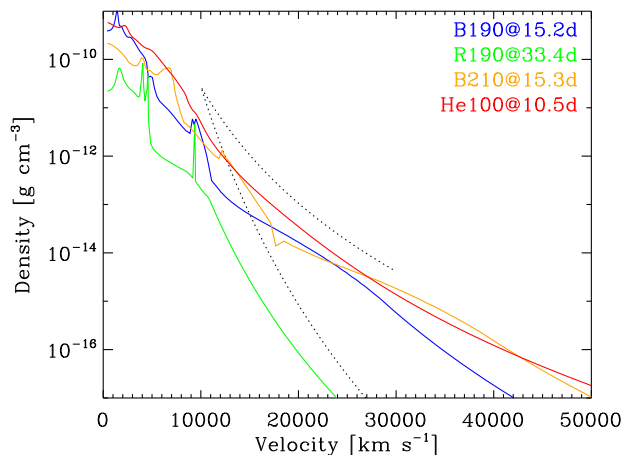


Figure 3. Ejecta density distribution for the PISN Models B190, R190, B210, and He100 at the onset of our CMFGEN calculations at 15.2, 33.4, 15.3, and 10.5 d after explosion. For comparison, we overplot as a dotted line the slope for a power law with exponent 8 and 15.

at very late times partly mimics the effect of mixing since γ -rays are then able to travel from their deeply located emission site in the ejecta to the O-rich, the He-rich, and possibly the H-rich outer ejecta (Sect. 5.4).

2.3 Radiative-transfer calculations

Apart from the different hydrodynamic inputs, the numerical procedure adopted in this work on PISN radiative-transfer simulations is the same as that employed previously for the simulations of SN II-peculiar and in particular SN 1987A (Dessart & Hillier 2010; Li et al. 2012), SNe II-Plateau (Dessart & Hillier 2011a), SNe IIb/Ib/Ic (Dessart et al. 2011, 2012b). Hillier & Dessart (2012) have recently given a full description of the code CMFGEN for SN applications, detailing the important components for the radiative transfer in SN ejecta. Since the code can naturally handle a wide range of composition mixtures (all important elements up to Nickel can be treated), the extension to treat PISN ejecta requires no specific adjustment compared to the modeling of standard CCSNe or SNe Ia.

We perform time-dependent simulations for the full ejecta at all times, and start by re-mapping the ejecta chemical stratification and structure (radius, density, temperature) computed with $\ddot{1}d$ once homologous expansion is reached. In practice, we start the He100 model at 10.5 d, the B190 model at 15.2 d, the B210 model at 15.3 d, and the R190 model at 33.4 d after explosion. This time increases with progenitor radius because for larger stars, the corresponding ejecta takes longer to significantly expand beyond its original spatial extent.² Given the long duration of the high-brightness phase for these events and the low early SN luminosity for the BSG and WR star explosions, starting this late is not a

² In the RSG explosion model R190, the helium-rich shell, near 4000 km s^{-1} , and sandwiched between the inner O-rich shell and the outer extended H-rich envelope has still not settled into homology. Here, enforcing homology leads to an artificial increase in velocity (and hence in radius) for the corresponding layer, producing a higher ejecta mass by 7%. The CMFGEN model R190 is then in fact $176 M_{\odot}$. The BSG and He models are not affected by this issue.

strong limitation here. For a description of the shock breakout and early light-curve signatures, the reader should consult Kasen et al. (2011) or Waldman et al. (in prep.).³

While the 1D Lagrangian hydrodynamical model computed with $\ddot{1}d$ contains about 2000 mass shells, the radiative transfer calculations are performed with a much smaller number of depth points. The critical scale to resolve is not mass but optical depth and we find that we obtain converged results with typically 5–7 points per optical-depth decade (Dessart & Hillier 2010). In these PISN simulations, we use a fixed number of 150 depth points at all times, providing a satisfactory resolution of $\sim 100 \text{ km s}^{-1}$ near the base of the ejecta, decreasing to $\sim 1000 \text{ km s}^{-1}$ at the fast-expanding outer edge.

The bulk of the ejecta is located at high optical depth at early times and its base remains optically-thick until 200–300 d after bolometric maximum. However, for consistency and simplicity, we treat the entire ejecta in non-LTE at all times. This is not optimal in terms of memory requirements, but it turns out that the optically thick layers are close to LTE and converge very fast. It also allows us to smoothly handle the phase when the ejecta starts to thin out in the continuum – when this occurs some spectral regions may still be thick (e.g., in the UV where many lines overlap, blanket efficiently the radiation, and drive the photons towards a blackbody distribution locally) while other spectral regions are already transparent (e.g., in the IR where the distribution of line opacity is more sparse). In general, numerous lines will remain optically thick for weeks after the continuum has become optically thin. Because we model the full ejecta, we adopt a zero-flux inner boundary.

We explicitly treat non-thermal processes associated with radioactive decay. This is particularly important given the large mass of ^{56}Ni (we only consider the decay of ^{56}Ni and ^{56}Co in this study) and the low ionization conditions we obtain in PISN ejecta. Through a solution of the Spencer-Fano equation (Spencer & Fano 1954), we compute the contributions to non-thermal excitation and ionization for all elements as well as the contribution to heating, and incorporate this in the non-LTE rate equations and the energy equation. A detailed presentation and application of this non-thermal treatment is given by Li et al. (2012); Dessart et al. (2012b). For the computation of non-thermal rates, we proceed by injecting all the decay energy as high-energy electrons of 2 keV and solve for the electron-degradation function at 2000 linearly-spaced energy bins down to 1 eV. At each of the 150 ejecta depth points, we construct and solve an upper diagonal matrix of 2000×2000 , which is trivial, but does require up to 30 minutes in these PISN simulations. We reduce the computational burden of our non-thermal solver by considering in the computation only the most important ions of each species. As the electron density is the main quantity modulating the magnitude of non-thermal processes in a given calculation, and since it varies slowly between consecutive iterations, we recompute the non-thermal electron-degradation function every ten iterations. With this procedure, the treatment of non-thermal processes increases the total computational time of a model typically by a few percent.

The γ -ray escape from the ejecta is minute for all times considered here, but the huge scale and mass of the ejecta combined

³ We note that given all the uncertainties on the PISN progenitors and the extreme sensitivity of the breakout signature on the progenitor atmospheric scale height, the presence of an optically-thick wind, or simply the stellar radius, the shock breakout signal is far from a clean signature to constrain the progenitor and explosion properties.

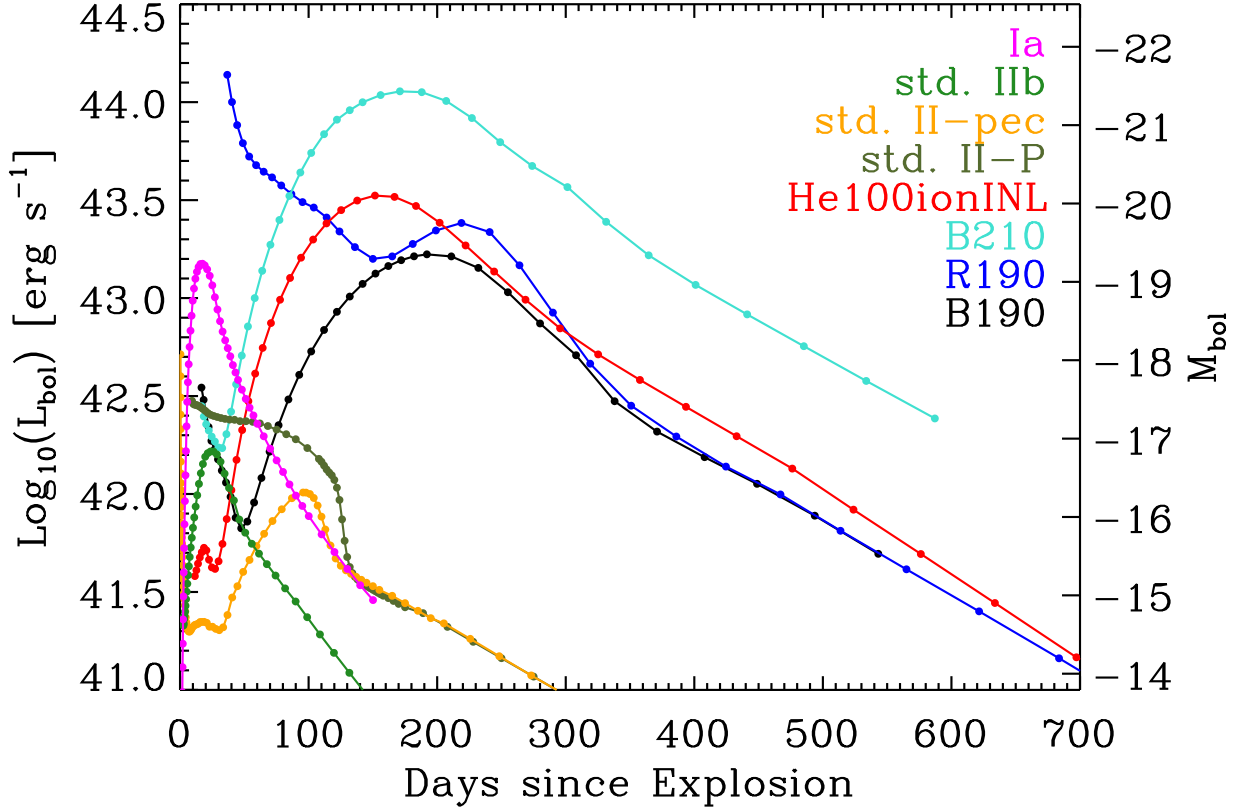


Figure 4. Synthetic bolometric light curves extracted from our non-LTE time-dependent CMFGEN simulations. Shown are our results for the PISN simulations discussed in this work: B190 (black), R190 (blue), B210 (turquoise), and He100ionINL (red). To better reveal the extraordinary properties of these PISN models, we also show our recent results for a “standard” SN II-P (olive; evolved at solar metallicity from a single $15 M_{\odot}$ main-sequence star; model s15e12 of Dessart & Hillier 2011a), a “standard” II-pec (orange; evolved at the LMC metallicity from a single $18 M_{\odot}$ main-sequence star; model “lm18a7Ad” of Dessart & Hillier 2010), a “standard” IIb SN (green; evolved at solar metallicity from a binary $18 M_{\odot}$ main-sequence star; model 365A2 of Dessart et al., in prep), and a SN Ia produced by the delayed-detonation in a Chandrasekhar-mass white dwarf with $0.67 M_{\odot}$ of ^{56}Ni (magenta; Dessart et al., in prep). In these last two models, γ -ray transport is solved for, predicting the fast decline rate during the nebular phase through γ -ray escape. Here, we use the term “standard” to stress that such II-P, II-pec, and IIb models match closely the bolometric light curve for the representative SN of each type observed routinely in the local Universe. Although B190(NL) and B210(NL) correspond spectroscopically to a SN II-pec, R190(NL) to a SN II-P, and He100(NL)/He100ionI(NL) to a SN Ic, their photometric properties are obviously extraordinary. For each sequence, small filled circles indicate the actual post-explosion times at which the computations are performed. For reference, we give the bolometric magnitude on the right-hand-side ordinate axis.

with the increasing γ -ray mean free path leads to non-local energy deposition within the ejecta. We find that this effect leads to the appearance or strengthening of H I or He I lines at nebular times, and more generally tends to cause the broadening of line profiles with time as the SN progresses into the nebular phase. Hence, we typically adopt local energy deposition up to 200 d after explosion and employ a γ -ray transport code (Hillier & Dessart 2012) to compute the non-local energy-deposition profile subsequently. The energy deposition from γ -rays is calculated once at the start of the simulation since it depends only on density, radius, time, and composition (i.e., quantities that are not affected by the radiative-transfer solution or the ionization state of the gas) of the ejecta. Hence, CMFGEN models are run assuming either local energy deposition, or non-local energy deposition (model name is then appended by “NL”, e.g., models R190 and R190NL).

The model atoms adopted for all simulations in this work are comparable to that used in Dessart & Hillier (2011a) and are presented in the appendix, in Table B1, together with the relevant references. Not all simulations were performed at the same time and not all have the same model atoms. Simulations B190, R190, B210,

and He100 were performed first, ran with the same model atoms, and neglected the neutral ions Mg I, Si I, S I, and Ca I. We added these in the second-generation simulation He100ionI. We in fact use that simulation to compare to observations of the Type Ic SN 2007bi, as well as to gauge the blanketing effects from these neutral species. As we discuss in Appendix C, they have a significant influence on the spectra and colors, but hardly influence the bolometric light curve. Hence, most properties of model He100 apply to model He100ionI; when these differences are significant, we specifically address them.

The completeness of the model atoms is always an issue in our approach since we cannot blindly incorporate millions of lines from an extended list. Our line opacity enters the computations through the specific treatment of atomic/ionic levels and so we have to compromise between completeness and tractability. Each of the four simulations we present here requires about 40 steps each taking about 3 days on 12 cores. The memory is mostly taken by the matrix to invert (Hillier & Miller 1998; Hillier & Dessart 2012), which contains all the terms from the linearized statistical and radiative equilibrium equations. The total memory allocated is typi-

cally $NT^2 \times (N_{\text{bands}} + 1) \times ND$ where NT is the total number of equations (variables), N_{bands} is 1 (3) for a diagonal (tridiagonal) operator, and ND is the number of depth points. We typically use $NT = 2000$ (as in Table B1), $N_{\text{bands}} = 1$, and $ND = 150$, corresponding to a memory of $2000^2 \times 2 \times 150 \times 8 \sim 9.6$ Gb.

Radiative-transfer simulations for PISNe have been performed in the past. Scannapieco et al. (2003, 2005) focused on RSG star progenitors giving rise to SNe II-P, with approximations for the transfer such as flux-limited diffusion and blackbody spectra. Their bolometric light curves should therefore be accurate but their spectral colors are uncertain. Gal-Yam et al. (2009) performed similar simulations but focusing on a range of He cores and explosion characteristics to model the observations of SN 2007bi (they model the light curve and one nebular-phase spectrum). As we discuss in Dessart et al. (2012c), non-LTE line-blanketed simulations of PISN ejecta (which we present in detail in this work) yield a suitable match to the SN 2007bi light curve, but are in conflict with numerous observed spectral characteristics of SN 2007bi. Kasen et al. (2011) did an extended study of PISN light curves, including RSG, BSG, and WR star progenitors. As in our grid of models, they do not have a well motivated mechanism for predicting PISN explosions from BSG or WR stars so the final masses and stellar types at death remain rather speculative and thus represent exploratory material. With their radiative transfer, they considered both the multi-band light curves and spectra, highlighting for example the striking dependency on metallicity or the signatures for shock breakout, but their assumption of LTE for the gas, their approximate treatment of line opacity, and their focus on early-time photospheric-phase spectra limit the applicability of their models for confrontation to observations of PISNe candidates like SN 2007bi. This SN, like most superluminous events today, are still discovered at or beyond the peak of the LC, expected to occur weeks to months after explosion. At this phase, the SN ejecta has considerably expanded and starts becoming optically thin in the continuum, while the potential presence of a large amount of IGE may maintain a high optical depth in lines for many months still. This configuration requires a detailed non-LTE line-blanketed treatment, which we adopt here.

The radiative-transfer calculations performed with CMFGEN yield the level populations, electron density, and temperature as a function of depth and time. Summing over level populations gives the ion and atom populations as well as the ionization state of the gas. Concurrently, the properties of the radiation field are computed as a function of depth, frequency, and angle. In the next sections, we describe both the gas and the radiation properties, in an attempt to identify the photospheric-phase and nebular-phase signatures of PISNe. In the next section, we start by discussing the bolometric light-curve properties.

3 LIGHT CURVE EVOLUTION

One important output of CMFGEN is the emergent spectrum in the observer's frame. By integrating this flux over frequency at each time step, we recover the bolometric light curve. We show the synthetic bolometric luminosity for PISN models B190, R190, B210, and He100ionINL in Fig. 4. The fundamental signatures of these PISN models is the very long duration of the high-brightness phase, typically of a few hundred days, reaching peak luminosities on the order of $10^{10} L_{\odot}$ at 150–200 d after explosion. Specifically, we find a bolometric maximum at 196, 220, 177, and 156 d for models B190, R190, B210, and He100ionINL. In the same order, the bolometric maximum luminosities are 4.4×10^9 , 6.3×10^9 ,

3.0×10^{10} , and $8.8 \times 10^9 L_{\odot}$. Allowing for non-local energy deposition changes these values by a few percent over this timespan. In the lower mass model He100ionINL, γ -ray escape starts being visible at ~ 500 d after explosion, introducing a slight downward tilt of the fading rate below 0.01 mag d^{-1} , while for all other models (with an ejecta mass in the range 130–160 M_{\odot}), full γ -ray trapping holds exactly. Note that PISN explosions may not systematically be super-energetic and superluminous (Kasen et al. 2011), but our set of models was selected to be so, with kinetic energies of a few tens of B and nucleosynthetic yields including a few M_{\odot} of ^{56}Ni .

The morphology of these light curves is analogous to the SNe we observe in the local Universe: the Type II-Plateau class (R190), arising from a RSG progenitor (Falk & Arnett 1977), the Type II-pec class (B190 and B210) arising from a BSG progenitor (Arnett et al. 1989), and the Type Ib/c class (He100) arising from a WR star progenitor (Ensmann & Woosley 1988; Dessart et al. 2011, 2012b).

The anomalously large initial radius and kinetic energy of model R190 yields a “plateau” brightness over 10 times more luminous than obtained in the SN II-P model resulting from a 1.2 B 15 M_{\odot} RSG progenitor (olive curve; model taken from Dessart & Hillier 2011a). The 2.63 M_{\odot} of ^{56}Ni originally made in the explosion causes a strong re-brightening at 200 d after explosion, following the recession of the photosphere to deeper layers and the outward migration of a heat wave powered by ^{56}Co decay. This hump is never seen in SNe II-P produced from lower mass RSG progenitors because they produce too little ^{56}Ni in their explosion. Beyond 350 d, model R190 radiates at the instantaneous rate of decay energy deposition, even when allowance for γ -ray escape is made. The ejecta remains optically thick to γ -rays throughout the evolution modeled here, so that γ -rays may escape from the original site of emission but are eventually trapped somewhere else in the ejecta.⁴

The light curve morphology for model B190 and B210 is explained in the same terms as for standard SNe II-pec like SN 1987A (Blinnikov et al. 2000; Dessart & Hillier 2010; Li et al. 2012). However, as for R190, the light curve is much brighter and broader than for a standard II-pec model (orange; model evolved at the LMC metallicity from a rotating single 18 M_{\odot} main-sequence star; Dessart & Hillier 2010; Li et al. 2012). The luminosity falloff after shock breakout is much more gradual and extended and the onset of re-brightening, due to heating by radioactive decay, occurs later at about 50 d after explosion. The bright peak is much bigger due to the larger mass, optical depth, and hence diffusion time of the corresponding ejecta. In model B210, which synthesized 21.3 M_{\odot} of ^{56}Ni , the peak luminosity is $10^{44} \text{ erg s}^{-1}$ — ~ 7 times larger than in model B190 which synthesized only $\sim 3 M_{\odot}$ of ^{56}Ni . As in model R190, the larger ejecta mass prevents the rapid luminosity evolution seen in lower mass Type II SNe.

The light curve morphology for model He100ionI (and He100; see Appendix C) is typical of a Type I CCSN, with a faint post-breakout plateau, followed by a steep rise due to decay heating at depth. The strong re-brightening starts ~ 30 d after explosion in this model, thus significantly later than in SNe IIb/Ib/Ic models (Ensmann & Woosley 1988; Dessart et al. 2011). Provided mixing is

⁴ The use of a coarser grid and the successive re-mappings in the R190 time sequence introduce a 10% change in the total mass and the ^{56}Ni mass as time progresses. This causes model R190 to have the same nebular luminosity as model B190, although the initial amount for ^{56}Ni is respectively 2.63 and 2.99 M_{\odot} . This resolution problem affects negligibly models B190, B210, and He100. See footnote 2.

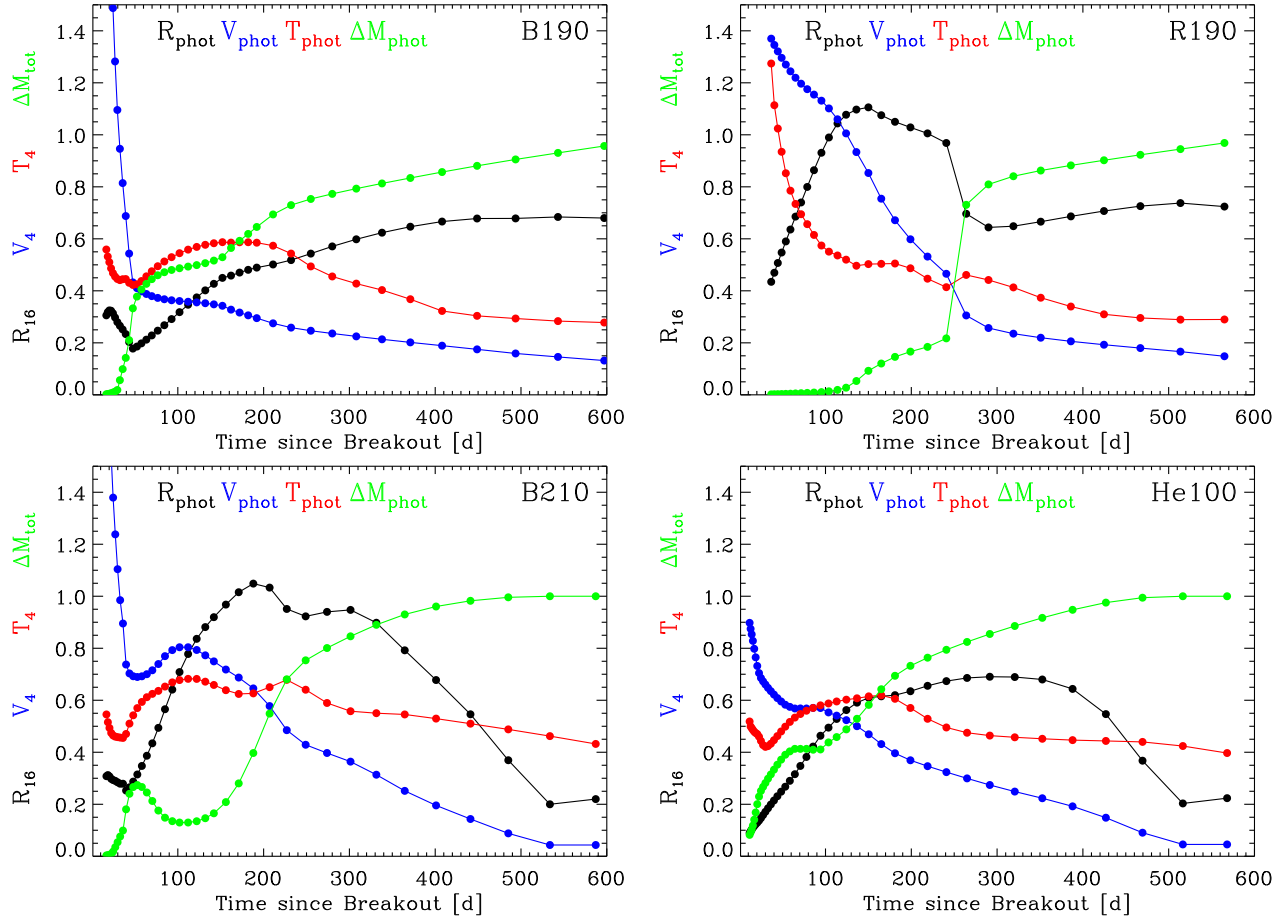


Figure 5. Evolution of properties at the electron-scattering photosphere, and specifically the radius (black; in units of 10^{16} cm), the velocity (blue; in units of 10000 km s^{-1}), the temperature (red; in units of 10000 K), and the overlying mass (normalized to the total ejecta mass; green) for model B190 (top left), R190 (top right), B210 (bottom left), and He100 (bottom right). The dots correspond to the actual times computed with CMFGEN. All ejecta models are optically-thin to electron scattering at $\gtrsim 550$ d (see Tables A1–A4).

weak in these PISNe (Joggerst & Whalen 2011; but see Chen et al. 2012), the rise to peak should not start much earlier than obtained here (Dessart et al. 2012b). As for models B190 and B210, the peak of the light curve is broad and luminous and qualitatively analogous between all three models. Although B190 and B210 correspond to a SN II-pec, R190 to a SN II-P, and He100ionI/He100 to a SN Ic, their photometric properties are obviously special and it makes sense to retain the PISN calling for these models.

Figure 4 comprises all the SN types studied so far with CMFGEN, and thus includes PISNe, SNe II-P, SNe II-pec, and SN Ib/c. To complete the set, we add results from on-going SNe Ia simulations for a delayed detonation in a Chandrasekhar-mass white dwarf synthesizing $0.67 M_{\odot}$ of ^{56}Ni (Dessart et al., in prep). In terms of peak brightness, such a SN Ia rivals luminous PISNe but its much lower mass prevents a sustained luminosity beyond ~ 30 d after explosion.

4 PHOTOSPHERIC PROPERTIES

As can be seen in Fig. 5, the photospheric⁵ temperature is rather low in all models at all times, although a higher temperature is found for the R190 model because it starts from a much more extended configuration that dwarfs cooling from expansion (associated with the PdV term in the energy equation; Dessart & Hillier 2011a). Since the photosphere is rather cool, PISN ejecta achieve a tremendous luminosity by remaining optically thick out to large distances – the maximum photospheric radii in models R190 and B210 exceed 10^{16} cm, while the maximum photospheric radii for B190 and He100 reach 5×10^{15} cm. These radii are typically ten times larger than predicted for SNe resulting from the explosion of lower-mass massive stars, whatever their type (Dessart et al. 2008; Dessart & Hillier 2010, 2011a; Dessart et al. 2011).

⁵ Here, we define the photosphere as the ejecta location where the inward integrated electron-scattering optical depth is $2/3$. At early times, when there is little line opacity, most photons will originate (i.e., be created) below the “electron-scattering” photosphere. At later times, the ejecta is metal rich and will have considerable line opacity and so using the Rosseland-mean or the flux-mean opacity would yield a location for the photosphere that is further out. Hence, our discussion of the “photosphere” is merely illustrative.

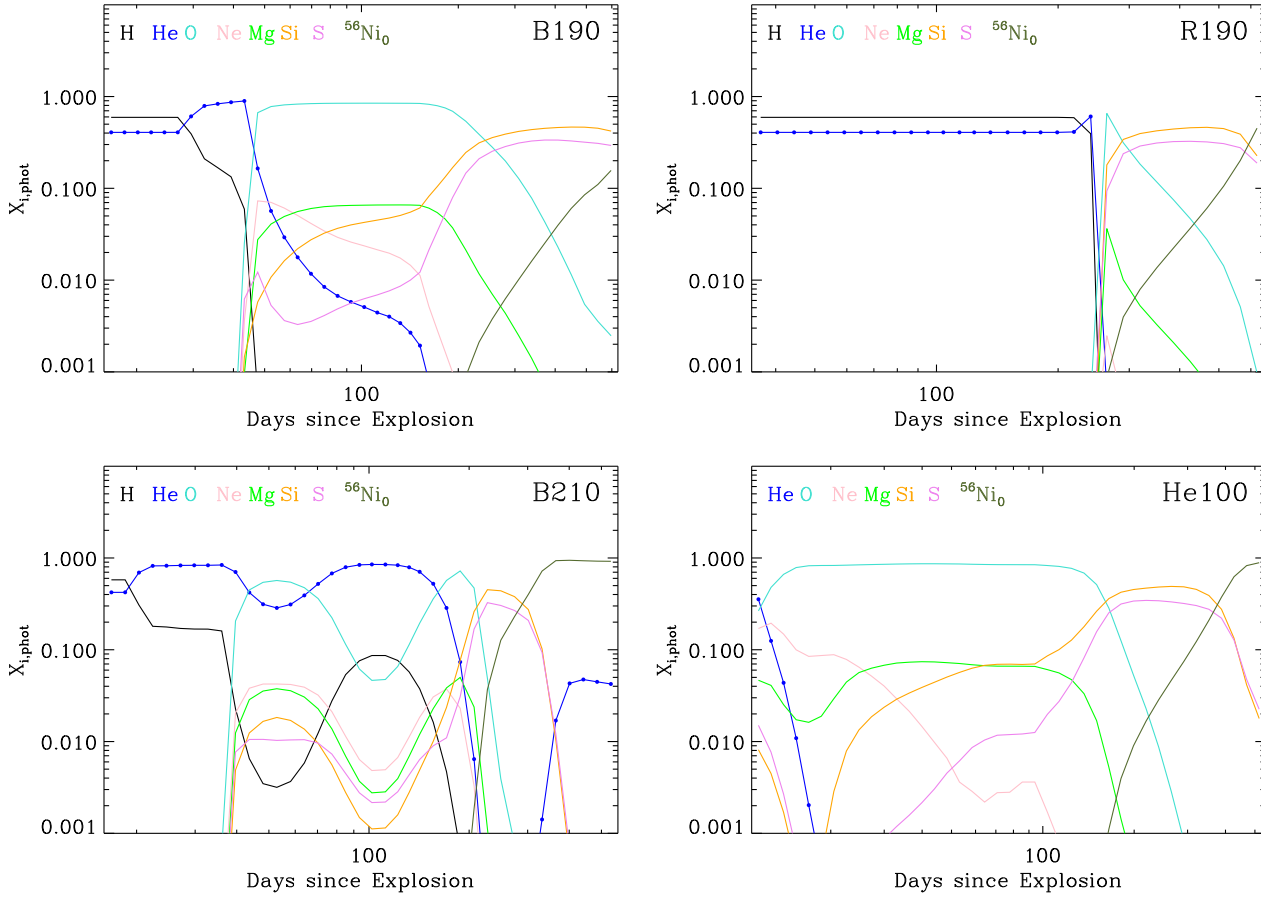


Figure 6. Evolution of the composition for representative species at the electron-scattering photosphere for model B190 (top left), R190 (top right), B210 (bottom left), and He100 (bottom right). $^{56}\text{Ni}_0$ refers to the sum of the mass fractions for the ^{56}Ni -decay products (it thus corresponds to the initial ^{56}Ni mass fraction in the corresponding mass shell). Most simulations have a short photosphere residence time in the H-rich envelope (B190 and B210), or none at all for He100 in which the compact and H-deficient progenitor produces a photosphere in the O-rich shell up to 200 d. In model R190, up to 250 d is spent in the H-rich extended progenitor envelope, but by the time the photosphere reaches its base, the He-rich and O-rich shells are fully recombined and transparent so the photosphere moves directly into the Si/S/IGE-rich inner ejecta.

Beyond 50 d after explosion, and thus well before the light-curve peak for all models, the photosphere is at the recombination temperature for the dominant ion (H, C, or O), which happen to have a similar ionization potential of 11–14 eV, and is on the order of 5000–6000 K. We thus expect red colors and spectra dominated by neutral and once- and twice-ionized ions (Appendix A & Fig. A1).

As the evolution proceeds the photosphere generally migrates to deeper layers – this is best seen by looking at the photospheric velocity, or the mass that lies above the photosphere (Fig. 5). The speed of recession is connected to the ability of the SN to remain hot and ionized because free electrons can contribute significantly to the opacity at the photosphere through electron scattering. Model R190 shows a slow progression of the photosphere inwards initially, which remains in the outer 1% of the ejecta (in mass coordinate), before showing a prompt recession at the end of the plateau phase at ~ 230 d when it enters the core (this phase could have been better resolved with our simulations). The photosphere then crosses 60% of the ejecta mass in about 10 d as the ejecta becomes thin, essentially crossing the entire O-rich shell. In models B190 and He100, the recession to deeper layers is fast early on and slows down as the decay heating becomes effective, halting temporarily

the photospheric recession. In B210 the heat wave is so fierce that it makes the photosphere move *outward* through $\sim 27 M_\odot$ of ejecta material between days 50 and 100 (Fig. 5). As a consequence of this phenomenon the photospheric velocity does not vary monotonically.

The migration of the photosphere to deeper layers leads to the complete probing of the ejecta, from the progenitor surface to its core, over a time span of about 300 d. Because of the large ejecta mass and the presence of shells of distinct composition, exacerbated by the low-primordial metallicity, this migration reveals an unprecedented chemical evolution at the photosphere (Fig. 6).

The enormous energy of a few tens of B released through burning (Sect. 2.2) is compensated in PISN explosions by the huge ejecta mass. This is largely independent of the mass loss prescription since the pair-production instability can only occur if the core mass is greater than $\sim 60 M_\odot$ (Heger & Woosley 2002). No matter what, the ejecta mass will be huge, well above that of any CCSN progenitor identified or inferred so far. A representative ejecta velocity is $v_{\text{rep}} \equiv \sqrt{2E/M} \sim 3200 \sqrt{E_1/M_{10}} \text{ km s}^{-1}$, where E_1 is the kinetic energy in units of B and M_{10} is the ejecta mass in units of $10 M_\odot$. A typical value for a RSG or BSG explosion in the local Universe is $E_1 = 1$ and $M_{10} = 1$, i.e., $v_{\text{rep}} \sim 3200 \text{ km s}^{-1}$.

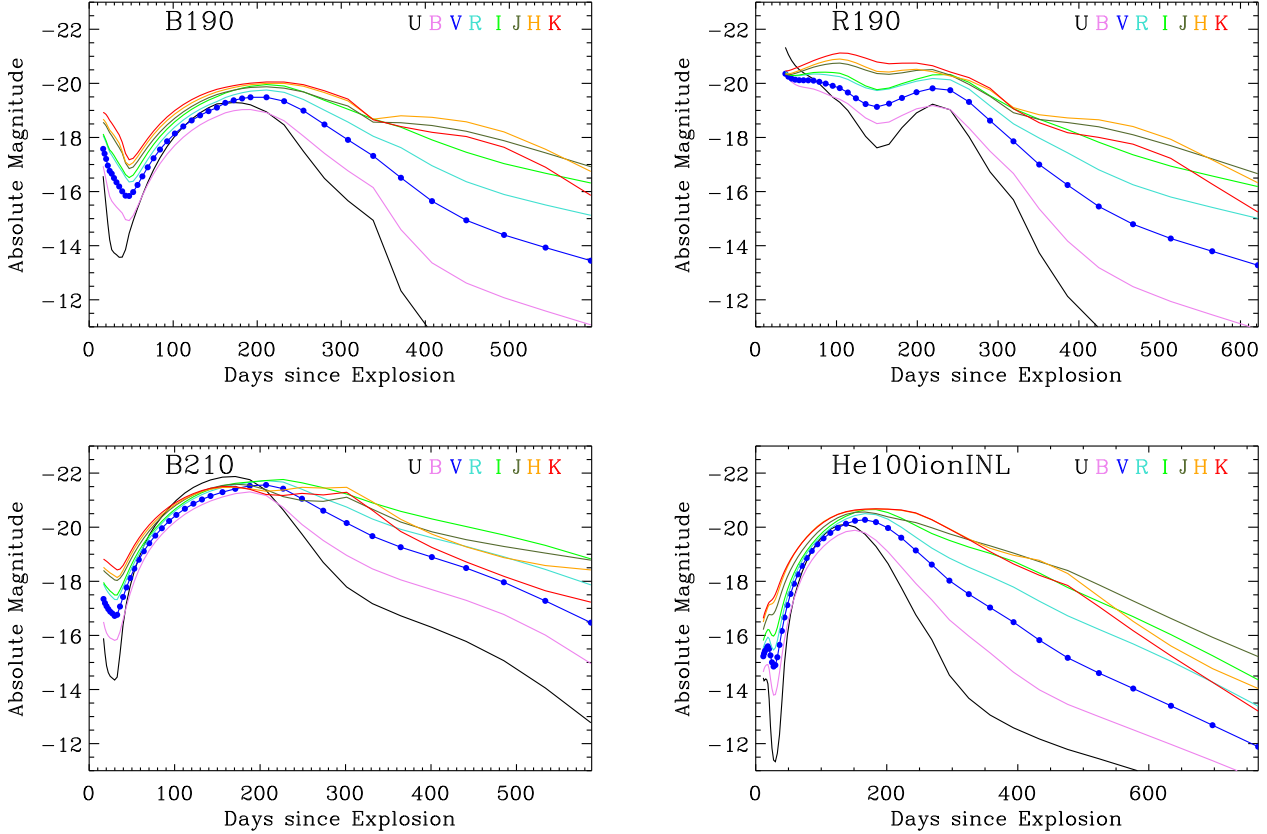


Figure 7. Multi-band light curves for our PISN simulations obtained by integrating at each epoch the synthetic spectra over the band pass of filters U, B, V, R, I, J, H, and K. The absolute magnitude is shown. Magnitudes plotted here are also logged into Tables D1–D4. In each sequence, we obtain slight kinks in the magnitudes (especially in bands U, J, H, and K, where little flux is emitted) that do not occur in bolometric luminosity. These are tracked down to changes in parameters at the corresponding time, e.g., as the medium turns optically thin (switch to nebular inner boundary), change in SL assignment (split the lower 5 to splitting the lower 10 levels for all ions), or change in model atoms (e.g., switch to a big Fe I model atom). While these glitches are not physical, the ejecta relax to the new proper solution at the next time step.

For our PISN models, the increase in explosion energy more than compensates for the increase in ejecta mass and we have $v_{\text{rep}} \sim 5000 \text{ km s}^{-1}$, comparable to SNe Ib/c (Dessart et al. 2011) from intermediate-mass binary stars, but a factor of two lower than in a Chandrasekhar-mass white-dwarf explosion. Although both PISN and SN Ia are thermonuclear explosions, the bulk of the burning takes place in the inner envelope in a PISN, yielding a chemical stratification more typical of core-collapse Type Ic SNe: The ^{56}Ni is produced at the base of the ejecta, remains confined to the lowest expanding material with velocities less than 4000 km s^{-1} (Fig. 2), and the decay energy has to diffuse from there through the overlying buffer of mass to influence the outer ejecta and the light curve.

The various properties described above for the bolometric luminosity and the photospheric properties assist the interpretation of the multi-band light-curves presented in Fig. 7. All models reach absolute visual magnitudes on the order of -20 to -22 mag. Model R190 exhibits a quasi-plateau in the V band, together with a hump at 250 d caused by decay heating. The higher photospheric temperature makes the spectral-energy distribution (SED) peak short-ward of the Balmer jump for about two months following explosion. This evolution is typical of RSG explosions, with the magnitudes dropping fast in the blue but leveling for a long time in the red. After the secondary bolometric peak, all magnitudes become fainter with

time, but continue to ebb faster in the blue. The evolution of colors for models B190, B210, and He100 are very different from model R190 at early times. The fading after shock emergence is more obvious, and so is the re-brightening as the heat wave reaches the receding photosphere. The colors become bluer on the rise to peak before fading again as the ejecta becomes thin. This fading is again faster in the blue.

An important feature of these multi-band light curves is that the colors are systematically red after the peak of the light curve. Figure 8 illustrates this color evolution for model He100ionI, which is representative of BSG/WR star progenitors models at all times — for RSG star progenitor models, this similarity holds for a few 100 d after explosion and beyond. Before the peak, all models from BSG and WR star explosions are getting bluer: This is because the photosphere is getting hotter due to the heating from decay *at depth* but without the “reddening” effects associated with high metal content at the photosphere (the photosphere still lies outside of these metal rich layers before the peak). The switch from red to blue and back to red as the SN evolves from the re-brightening to the peak, and eventually fading into the nebular phase is a distinctive signature of ^{56}Ni powered PISNe. This trend is somewhat similar to SNe Ia, with an additional re-hardening of the spectrum as the ejecta turn

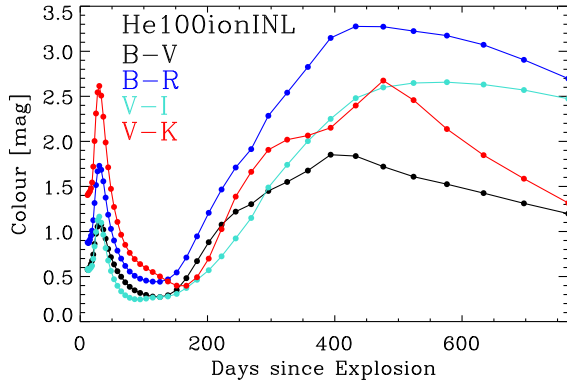


Figure 8. Same as Fig. 7, but now showing selected colours for model He100ionINL. An important feature of PISN model He100/He100ionI, shared with PISN models R190, B190, or B210 presented here, is the red colour of their spectra, especially at and beyond peak.

transparent. We will return to this issue when comparing our PISN models to the observations of SN 2007bi (Sect. 6.1).

5 SPECTRAL EVOLUTION: GENERAL PROPERTIES

From the preceding sections, we see that the four PISN models B190, R190, B210, and He100 show significant differences in their light curves (peak brightness, time to peak, presence or not of a post-breakout plateau), which are easily connected to the fundamental differences between the progenitors. We also expect the early spectra to differ significantly between models because of the differences between the progenitor envelopes. However, despite the different mass loss histories these models have similar supermassive helium cores and systematically produce large amounts of IMEs and IGEs from O burning (Sect. 2.1–2.2). Consequently, we expect the nebular phase properties to be rather similar due to the similarities of the progenitor cores. Thus we describe the spectral evolution during the photospheric phase for each progenitor type separately (RSG, BSG, WR) before grouping them to discuss their nebular-phase properties.

All our PISN models have a very large oxygen mass (39.6 to 48.1 M_{\odot}). However, as a consequence of the large ionization energy (13.6 eV) and the cool photospheric temperatures, O lines generally only have a weak direct influence on the spectra. The only exceptions are [O I] 6303–6363 Å, which is seen in nebular-phase spectra, and a few lines of O I which weakly influence the early photospheric spectra of He100.

Initially all models present a true continuum in the optical – that is the observed spectra consist of (broad) lines superimposed on an underlying background which is formed via continuum (i.e., bound-free and free-free) processes. However, eventually the photosphere recedes into layers where IMEs (primarily Si and S) dominate the composition of the ejecta. At this, and later times, the true continuum flux weakens and then disappears. However, before the true nebular phase, a pseudo continuum, not generated by true continuum processes, continues to be seen. It is generated by the huge number of lines associated first with IMEs and later on with IGEs. In some cases this allows, for as long as 500–600 d, the formation of P-Cygni profiles associated with line transitions from ions present in overlying mass shells.

5.1 Spectral evolution during the photospheric phase of PISN model R190

The large progenitor radius ($\sim 4000 R_{\odot}$) and explosion energy (33.2 B) for model R190 yield a SN which is photometrically (Fig. 4) and spectroscopically (Fig. 9) similar to a superluminous SN II-P. At early times, the outer ejecta and photospheric layers remain fully ionized (Fig. 5; Table A2) producing a blue continuum (red curve in the montage of Fig. 9). The relative high velocity and steep density profile of the photospheric layers (Fig. 3) yield broad but weak P-Cygni profiles (Dessart & Hillier 2005b; Dessart et al. 2008). At such times, the photosphere reside in the outer 1% of the ejecta mass, which is essentially pure hydrogen and helium (the metallicity is $10^{-4} Z_{\odot}$). Consequently, we find only H I Balmer lines and a weak He I 5875 Å. These are in fact typical spectral signatures of early-time SNe II-P (Pastorello et al. 2006; Quimby et al. 2007; Dessart et al. 2008), but there are some critical differences. To facilitate the analysis and line identifications we overplot in Fig. 9 (right panel) the synthetic spectra computed by omitting a given species.⁶

As the ejecta expands helium quickly becomes neutral – the inefficient mixing of ^{56}Ni from greater depths prevent any non-thermal effects at the photosphere (Dessart et al. 2012b) at these times in these PISN models. The adopted metallicity of $10^{-4} Z_{\odot}$ impacts all species other than hydrogen and helium so that CNO, IMEs, and IGEs have little (direct) influence on the spectrum – up to 200 d after explosion, we can only see (identify) H I Balmer lines. As the ejecta evolve, we do not see the appearance of Fe II lines, Ca II H&K or Ca II triplet at 8500 Å that are usually associated with Type II-P spectra.

The lack of metals in the Hydrogen-rich envelope completely quenches the effect of line blanketing. As can be seen in Fig. 9, the continuum (red curve) follows closely the total synthetic flux, except over spectral regions where the H I Balmer lines reside. However, by 200 d, a pseudo-continuum is visible in the full spectrum – a large number of lines, with no noticeable signature in the full spectrum, are contributing to the total flux, even in regions apparently devoid of lines. At this time, the spectral formation region is receding into layers containing IMEs. However, the photosphere is so cold that the emergence of line blanketing on the very weak flux short ward of 4000 Å is difficult to see. By 300 d after explosion, the spectrum has retained a similar color to that at 200 d. However, the pseudo-continuum is no longer produced by genuine continuum processes (the red curve is down at zero flux) but instead by line opacity from Fe II. By 400 d, the main ion contributing to this background line-opacity switches from Fe II to Fe I and produces an even redder pseudo-continuum (red and green curves in Fig. 9, right panel). By 600 d after explosion, the spectrum has visibly turned nebular.

In Fig. 10 (left panel), we illustrate the contrast between the spectrum from the explosion of a 15 M_{\odot} RSG progenitor at solar metallicity (model s15e12; Dessart & Hillier 2011a) and that from the R190 model at $10^{-4} Z_{\odot}$. The line profiles are broader in the

⁶ The other option is to include only the selected species. However, this procedure becomes dicey when continuum processes weaken and/or when line opacity dominates – both effects occur at nebular times in PISN explosions. In this case, taking out a dominant species completely alters the spectrum and the result is unusable. So, for consistency, we adopt the same procedure at all epochs and show these illustrations with the selected species omitted. This manipulation is done only for post-processing and analysis – all CMFGEN simulations are obviously performed with all species included.

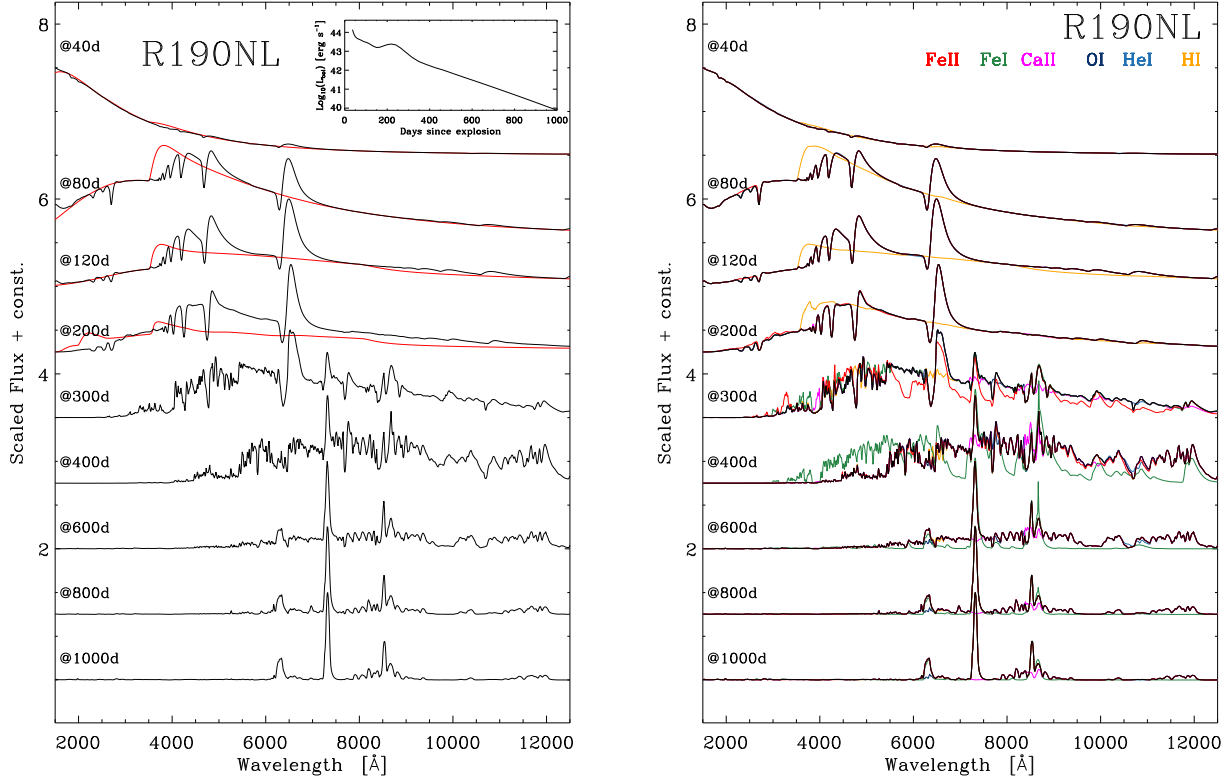


Figure 9. *Left:* Montage of synthetic spectra for the RSG model R190NL, showing the full spectrum (black) as well as the contribution from continuum processes only (i.e., bound-free and free-free processes; red). For completeness, we include an inset for the R190NL bolometric light curve. The emergent flux, scaled for better visibility (see inset for the absolute bolometric flux scale), is computed with CMFGEN by simulating the time-dependent non-LTE transport for the full ejecta from 36 until 1000 d after explosions. The sequence thus covers from times when the ejecta is optical thick until times when it is optically thin and nebular-line emission is strong. *Right:* Same as left, but we now overplot the corresponding spectra obtained by *neglecting* an ion (see color coding and labels at top-right). We illustrate the effect for ions that have a large impact on synthetic spectra.

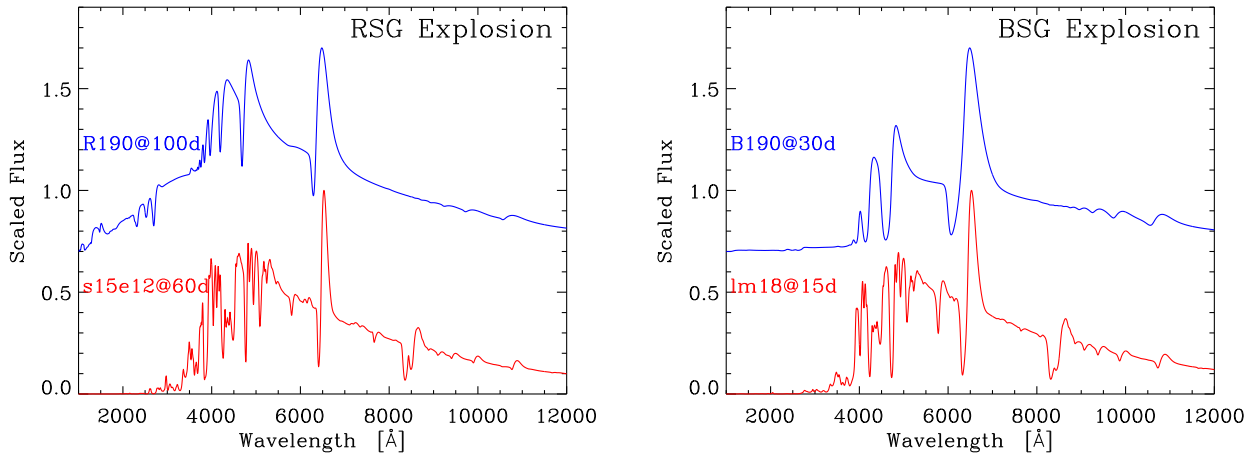


Figure 10. The left panel shows a comparison between the RSG PISN model R190 and the equivalent explosion from a lighter massive star at Z_{\odot} ($15 M_{\odot}$ s15e12 SN II-P model), while the right panel shows a comparison between the model B190 and the $18 M_{\odot}$ “lm18a7Ad” SN II-pec model at the LMC metallicity. The spectral morphology is similar, except that the PISN explosions at $10^{-4} Z_{\odot}$ show no metals lines (not even Na I D or the Ca II triplet generally seen in all Type II SNe) at times when their equivalent solar/LMC explosions show strong line blanketing throughout the UV and optical ranges.

PISN model, but the contrast with the low-mass SN II-P model is small due to the modest increase in E/M . Although the colors and H I Balmer lines appear similar, metals visibly affect the low-mass SN II-P spectrum in the UV (strong line blanketing) and optical (weaker blanketing, primarily due to Fe II, Ti II, and Sc II) but have little effect on the PISN spectrum. This makes H β easily recognized as a P-Cygni profile in the PISN spectrum while in the solar-metallicity spectrum, H β overlaps with numerous metal lines (e.g., Fe II), and appears only as an absorption feature. A similar effect was discussed by Kasen et al. (2011). Such RSG explosions in the early Universe could be used to constrain the environmental metallicity (or set an upper limit on the metallicity in case no metal lines are seen), either by means of the reduced blanketing in the UV or the weakness of metal lines (e.g. Fe, Ca) in the optical (see also Fig. 9 of Dessart & Hillier 2005b). The absence of Ca II lines at the recombination epoch is a unique feature of model R190, never seen in SNe II-P models, and never yet observed in SNe II-P.

The Doppler velocity at maximum absorption in the broad H I Balmer lines tracks closely the decreasing photospheric velocity, although weaker Balmer lines from higher up in the series may underestimate it (Fig. 11; left column). This apparently peculiar finding is well explained by the line formation process in the homologically expanding ejecta of SNe (Dessart & Hillier 2005a). Non-LTE and time-dependent effects also contribute to maintain a significant line optical depth at large velocities, producing persistent, strong and broad lines for H α and H β (Utrobin & Chugai 2005; Dessart & Hillier 2008).

5.2 Spectral evolution during the photospheric phase of PISN models B190 and B210

The spectral evolution of model B190 and B210 reflects the typical explosions from BSG stars, objects characterized here by a surface radius of 186 and 146 R_{\odot} (Figs. 12–13). As for model R190, the large explosion energies of 34.5 and 65.9 B, respectively, produce high representative ejecta velocities of $\sim 5100 \text{ km s}^{-1}$ and 6800 km s^{-1} , well in excess of the value of 2800 km s^{-1} inferred for SN 1987A (Arnett et al. 1989). At early times, the spectral evolution for these two models is qualitatively similar to the SN II-pec model of Dessart & Hillier (2010); Li et al. (2012) and the observations of SN 1987A.

Up to the phase of re-brightening (~ 50 d), the optical spectra are comparable to those of model R190 at the recombination epoch and are composed exclusively of H I Balmer lines. The lack of metals in the primordial gas, and the absence of mixing into the outer ejecta layers by enriched material (arising from steady or explosive burning), prevents any line blanketing in the UV or the optical. However, the smaller initial radius causes a much stronger cooling due to expansion, which induces early recombination at the photosphere and a fast recession of the photosphere (Fig. 6). While it took ~ 250 d to reach the helium core in model R190, the photosphere recedes to the base of the He-rich shell as early as ~ 50 d after explosion in models B190 and B210. As seen before for model R190, this corresponds to the appearance of new lines (from O I or Ca II) and the onset of line-blanketing effects, at this time primarily from IMEs.

The photosphere recession to the helium core quenches the emission in H α and other Balmer lines – a consequence of the small $\mathcal{O}(0.1)$ hydrogen mass fraction in the He-rich shell and the lack of non-local γ -ray energy deposition into the H-rich envelope at such early times.

In model B210, the larger ^{56}Ni mass causes a reversal of the

photosphere, which moves back into the helium shell, but in model B190, decay heating merely stalls the recombination wave halfway through the ejecta (in mass), within the O-rich shell. It is around the light curve peak and beyond that the decoupling layers for the radiation recede to the IGE-rich layers, causing the appearance of iron line blanketing at ~ 200 d after explosion.

In the right panel of Fig. 10, we show a comparison, at the recombination epoch, for models B190 at 30 d after explosion and the SN II-pec model of Dessart & Hillier (2010) at 15 d after explosion. As for the R190/s15e12 comparison, the PISN models B190 and B210 have systematically broader Balmer lines and lack the strong lines from Ca II, Na I, Sc II, and Fe II, present in the “1m18a7Ad” model at LMC metallicity. At such epochs these theoretical BSG explosions are relatively faint, and would be more difficult to detect than the much brighter R190 model.

For models B190/B210, the Doppler velocity at maximum absorption in the H I Balmer line is initially large, and declines as the photosphere recedes inward through the H-rich envelope (Fig. 11; right column, shown only for model B210). The decline is much more rapid than in R190, since the time scale for the photosphere to pass through the lower-mass H-rich envelope is ~ 50 d, much less than the ~ 250 d for model R190. In models B190/B210, the H I Balmer lines present a maximum absorption at a Doppler velocity that strongly overestimates (by a factor of ~ 2) the photospheric velocity at early times – the same effect is seen in SN 1987A (Dessart & Hillier 2010). However, as the model re-brightens and its photosphere leaves the H-rich envelope, the maximum absorption of the H I Balmer lines track a unique Doppler velocity, which corresponds to the velocity at the base of the hydrogen envelope.

5.3 Spectral evolution during the photospheric phase of PISN model He100

In this section, we describe the spectral evolution of a PISN arising from a WR progenitor using model He100ionI, which differs from model He100 by the treatment of additional neutral ions found to be important (Mg I, Si I, S I, and Ca I). We discuss specific differences between He100 and He100ionI in Appendix C, which are essentially confined to the colors in the first few weeks following explosion, and additional line features and blanketing.

At the start of the simulation, the He100ionI and He100 models are at 10.5 d after explosion and the photosphere has already receded to the base of the $\sim 8 M_{\odot}$ He-rich outer shell (Fig. 6) at $\sim 9000 \text{ km s}^{-1}$ (Fig. 5). The composition is still He-rich but the O, Ne, Mg and Ca are also abundant, with mass fraction for IMEs that are orders of magnitude larger than for a solar mixture at a metallicity of $10^{-4} Z_{\odot}$. This explains the dominant role of line-blanketing from IMEs, including Si and S, from such early times up to the peak of the light curve. It also explains the early appearance of strong Ca II lines.

This chemical stratification, although not as obvious as in the H-rich models discussed in the preceding sections, is reflected in the spectral evolution of model He100ionI (Fig. 14). Despite representing $\sim 8\%$ of the total mass of the ejecta, He is only present in the outermost ejecta shells. By 10 d after explosion, the photosphere has already crossed these He-rich regions so that there is no visible signature of He during the remaining part of the photospheric phase. This is consistent with the $\mathcal{O}(0.1)$ mass fraction of He in the outer layers (Dessart et al. 2011) together with the negligible non-thermal excitation/ionization at such epochs in the outer ejecta (Dessart et al. 2012b). We find Si I to be an important source of blanketing at the cool photosphere (for up to about

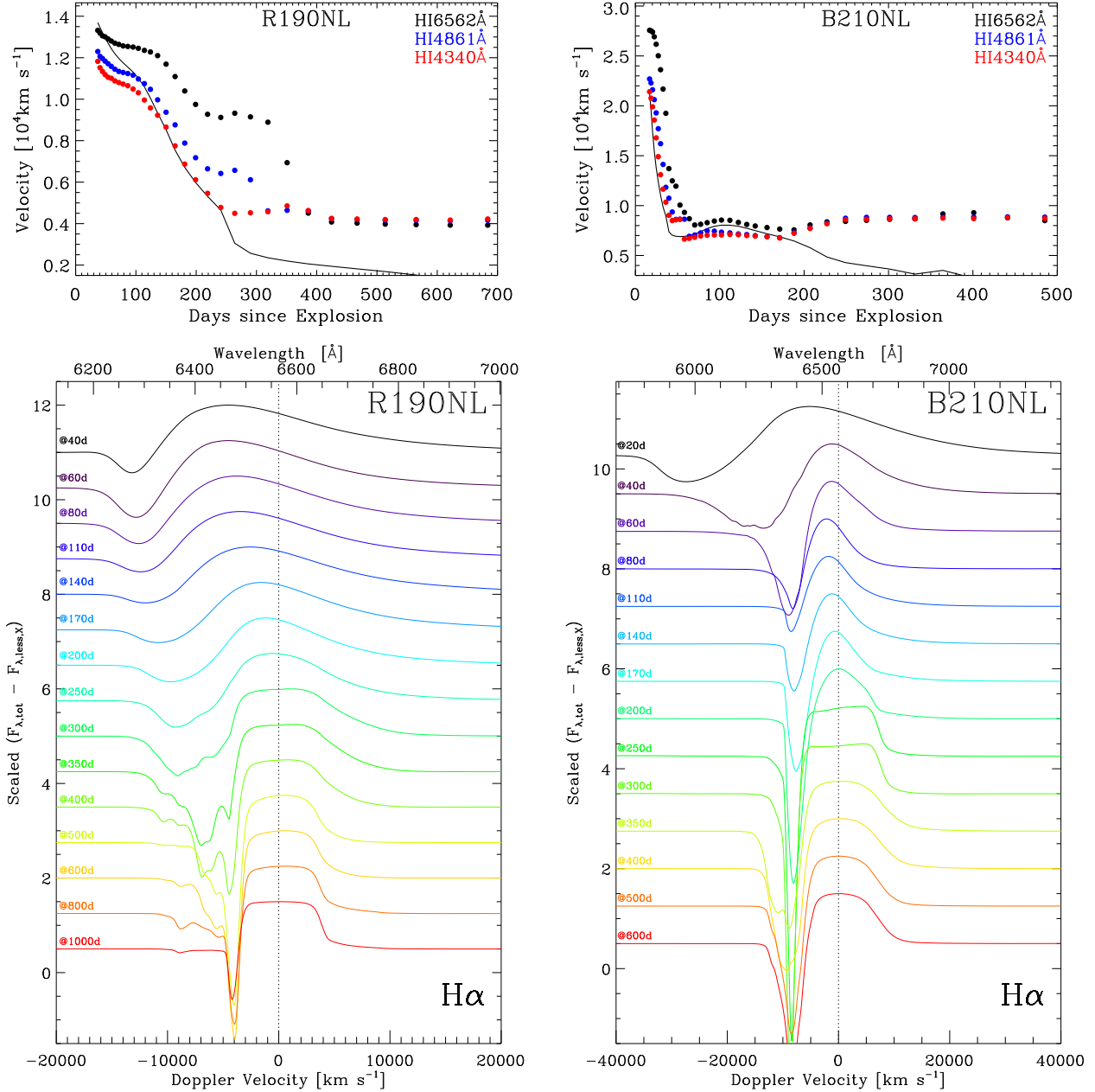


Figure 11. *Top Row:* Doppler velocity of the maximum absorption (filled dots) in H α (black), H β (blue), and H γ (red) for model sequence R190NL (left) and B210NL (right). For comparison, we overplot the evolution of the photospheric velocity (black line). *Bottom Row:* Evolution of the H α line profile in model R190NL (left) and B210NL (right). Notice the typical P-Cygni profile morphology, already discussed in Dessart & Hillier (2005b), with a maximum absorption that may underestimate or overestimate the photospheric velocity, and the blue shifted peak emission. At nebular times, the line profile evolves towards a flat topped emission with a P-Cygni profile absorption fixed at $\sim 4000 \text{ km s}^{-1}$ (R190NL) and $\sim 8000 \text{ km s}^{-1}$ (B210NL), which in each case corresponds to the velocity at the base of the hydrogen envelope (see Fig. 2).

50 d). The continuum flux testifies for the presence of important photo-ionization cross sections (e.g., from Mg I with an important edge at 3757 \AA) and the absence of strong line blanketing in the optical, since the continuum flux closely follows the total flux for up to a month (Fig. 14). To be complete about these line identifications, we find O I lines at $6157, 6454, 7002, 7254, 7777, 7990$, and 9260 \AA ; Mg I lines at $5167\text{--}5183 \text{ \AA}$; Mg II lines at 4481 and 7890 \AA ; Si I lines at $3905, 4102, 5500\text{--}5800$ (numerous

lines), 5948 \AA , $7250, 7289, 7410, 7742\text{--}7799, 8648, 9413, 10585, 10694, 10827, 10870, 10885, 10982 \text{ \AA}$; Si II lines at $4129, 5056, 5957\text{--}5978, 6239, 6347\text{--}6371, 7849 \text{ \AA}$; S I lines at $6052, 6750, 8712.44, 8874.48, 9228, 9421, 9650\text{--}9681, 10457, 10633$; and Ca II H&K, $7103, 7162, 8133, 8201, 8248, 8498, 8542, 8662 \text{ \AA}$. The strong Mg I 5167 \AA is a striking feature of He100 model around the peak of the LC.

The larger photospheric temperature on the rise to bolometric

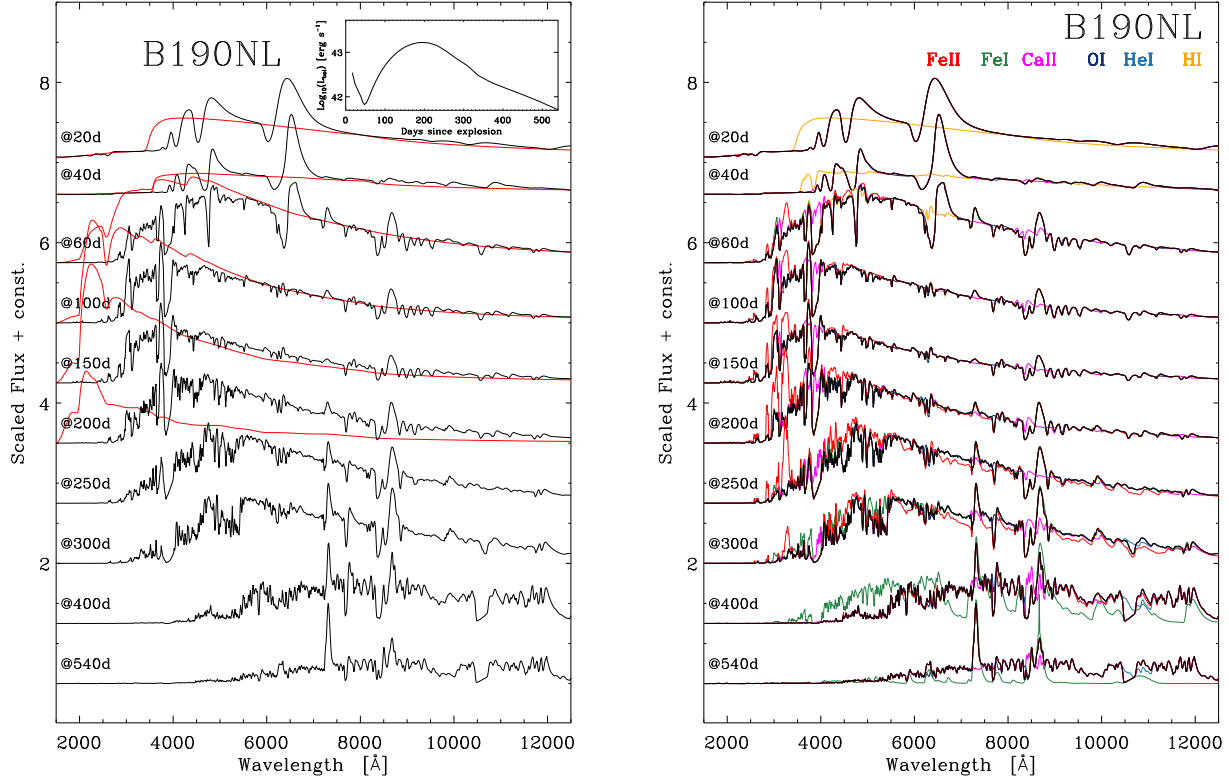


Figure 12. Same as Fig. 9, but now for BSG model B190NL with $190 M_{\odot}$ on the main sequence.

maximum (Fig. 5) is visible in the hardening of the spectra (see also Fig. 7) and the temporary weakening of blanketing from neutral IMEs. During that phase, the photospheric velocity is around 5000 km s^{-1} , and the optical line profiles appear relatively narrow (i.e., compared to the RSG/BSG progenitor models discussed above), apart from more optically-thick lines like Ca II. Numerous lines have a velocity at maximum absorption that underestimates the photospheric velocity (Fig. 15). As noted before and in Dessart & Hillier (2005a), this is caused by a projection effect in homologous ejecta since for increasing impact parameters, the location of maximum absorption tends to follow an iso-density contour, intersecting planes of ever smaller projected velocity. During this brightening phase, the continuum synthetic flux is again a good diagnostic for this heating and increased blanketing from earlier times.

By ~ 150 d after explosion (i.e., the light curve peak), the photosphere has now receded halfway through the ejecta, into the layers dominated by Si/S/IGEs, and its temperature goes through a maximum (of ~ 6000 K). From then onwards, the spectrum reddens, the blanketing from IGEs strengthens, initially through the effects of Fe II and eventually Fe I. The spectrum starts again showing strong lines of low-ionization and neutral species (as it did at ~ 50 d), but with the additional contribution from metal line blanketing. We also see the appearance of [Ca II] at 7291–7323 Å. As seen before for the B190 and B210 models, the spectra at and be-

yond light-curve peak are red, not blue, with the bulk of the flux emerging at 5000 Å , and progressing to longer wavelength as time proceeds. Throughout this phase, no He I line is visible, which again confirms the notion that a Type Ic classification is not a guarantee of helium deficiency (Dessart et al. 2012b). The fundamental feature of these PISN spectra are the ubiquitous and concomitant presence of lines from O, Mg, Si, and Ca, in a much more pronounced fashion than generally seen in Type Ic SNe. The low metallicity of the environment is not as obvious as for the R190 model, but noticeable after inspection from the lack of Fe II blanketing in the 5000 Å region; it is clear that the blanketing occurs but it is not IGEs like Ti or Fe that cause it here but instead IMEs and in particular Si.

To illustrate more vividly the blanketing caused by the numerous lines of metals, as well as its evolution with time, we show in Fig. 16 the distribution of the flux versus wavelength and velocity (equivalently the depth in the ejecta). Overplotted, we draw the photospheric location obtained for various opacity sources (electron-scattering, Rosseland-mean opacity, and flux-mean opacity). These photospheric velocities/radii are systematically smaller than obtained when accounting for the additional opacity of lines (red curve). Moving from the light-curve peak to ~ 300 d, the blanketing is even stronger in the UV and optical, and it continues to strengthen as the ejecta cools and recombines. This blanketing enhances the likelihood of interaction with a line for a photon emitted short ward of $\lesssim 5000 \text{ Å}$. Through fluorescence, this photon can give rise to multiple lower energy photons, which, being subject to

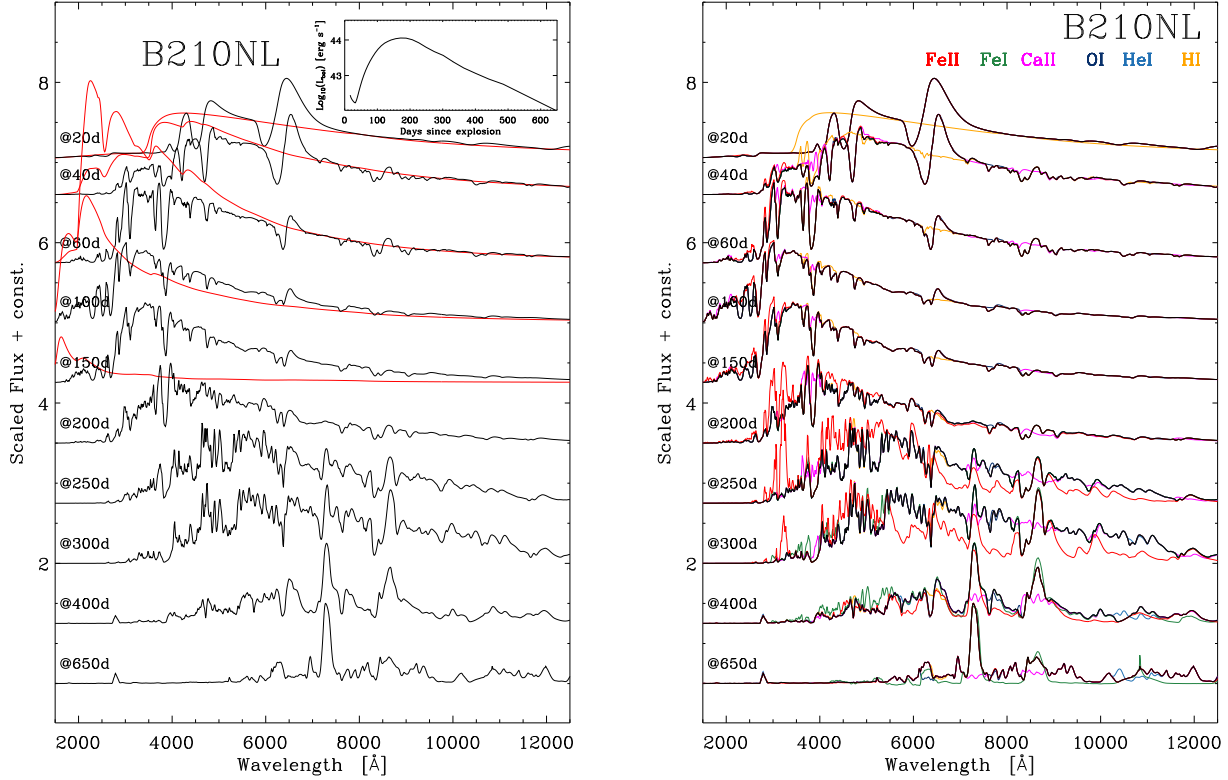


Figure 13. Same as Fig. 9, but now for BSG model B210NL with $210 M_{\odot}$ on the main sequence. Notice, in particular, the presence of He I 10830 Å at nebular times and the red colors at all post-peak epochs, despite the huge ^{56}Ni mass synthesized in this explosion.

a smaller opacity, can escape. Alternatively, blanketing lengthens the photon-residence time at depth, and thus enhances the probability for absorption. Because of the decrease in temperature outwards,⁷ this would translate into emission but now of lower energy photons. Both effects tend to deplete the flux where blanketing is strong, “reddening” the spectrum. Indeed, where the blanketing is strong, the flux is weak.

5.4 Nebular phase spectral evolution of all four PISN models

The transition to the nebular phase is not sudden, but occurs gradually as the intensity of weaker lines become less and less strong compared to the lines normally associated with the nebular phase of SN spectra (e.g., [O I] 6303–6363 Å, [Ca II] 7290–7290 Å and the triplet lines of Ca II at 8500 Å; and H α when H is present).

This outer ejecta, which contains few tens of solar masses of IMEs, O, He, and in some cases H, is like a nebula on top of a centrally illuminating source. This persistent incoming radiation is complemented by non-local deposition of decay-energy from γ -rays escaping the core emission sites, which occurs when the γ -ray mean-free-path becomes sizable compared to the ejecta extent. This can resurrect the outer ejecta which had earlier on become

completely transparent and invisible. Hence, in PISN models that were faint initially, the nebular phase represents a means of probing the outer ejecta again.

The strongest nebular line is [Ca II] 7290–7290 Å – it has a moderate critical density of $\sim 10^6 \text{ cm}^{-3}$, is easily excited by collisions with electrons, and for most of the SN evolution discussed in this paper Ca^+ is the dominant ionization stage of Calcium. [Ca II] 7290–7290 Å appears as a single broad feature at late times in all models – in fact it appears before the complete transition to the nebular phase, at 250 ± 50 d. In models B190 and B210, it is even present for a few weeks near ~ 50 d. In R190NL (which is representative of the whole set), we find that emission is limited to the regions below 4500 km s^{-1} in that model (except for H α), thus limited at all times to the progenitor He-core. It peaks at 4000 km s^{-1} at 200 d and systematically recedes with time down to $\sim 1500 \text{ km s}^{-1}$ at 1000 d. In contrast to Type II-SNe at near solar metallicity, there is no Ca II emission/absorption from the H envelope. This occurs because of the Ca deficiency outside of the core where Ca has a mass fraction of only 6.44×10^{-9} . The low metallicity of the PISN progenitors in our set quenches any outer-ejecta (i.e., the H or He envelope) emission/absorption from species other than H/He. We note at nebular times the overlap of the [Ca II] 7300 Å doublet with Ca I lines at 7148 and 7326 Å (see Appendix C).

The Ca II triplet is initially absent during the photospheric phase, appears as a relatively narrow P-Cygni profile as the pho-

⁷ In the optically-thin regions, the temperature distribution can be quite complex in practice due to density and composition changes, as well as the effects of non-local energy deposition.

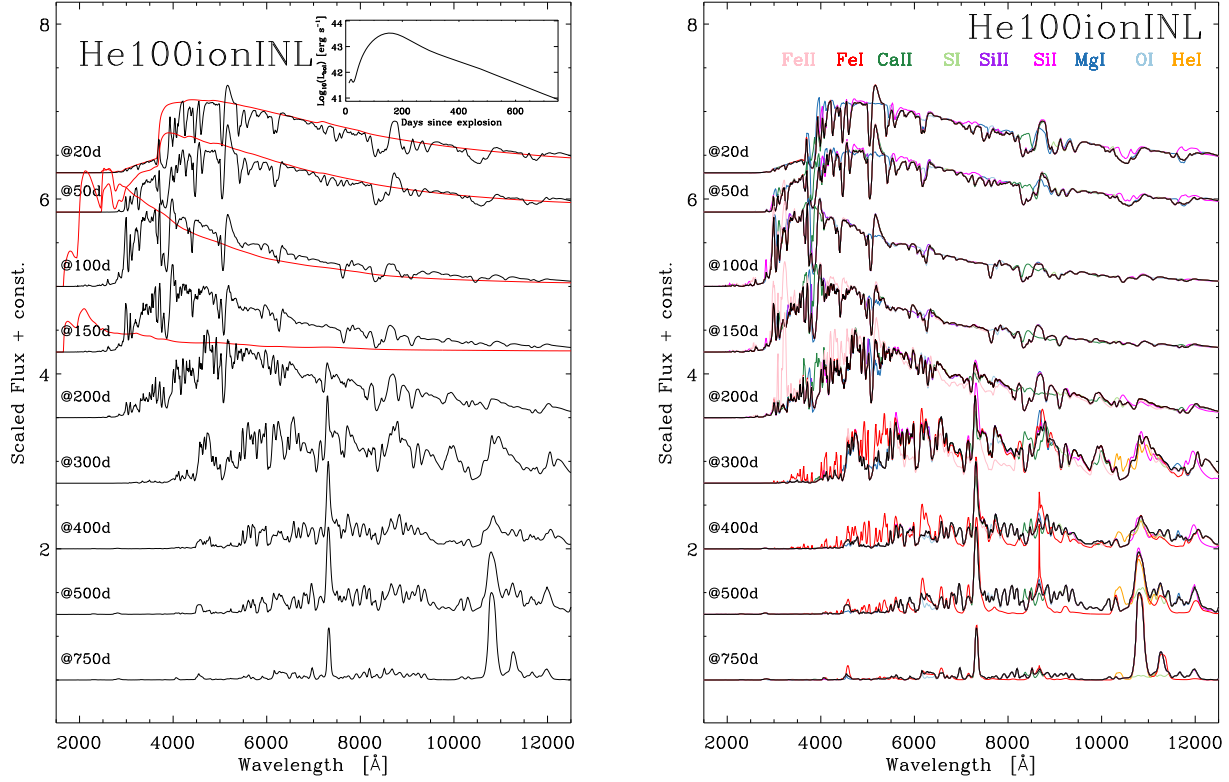


Figure 14. Same as Fig. 9, but now for $100M_{\odot}$ He-star model He100ionINL (same PISN model as He100, but the radiative transfer is computed with allowance for Mg I, Si I, Si II, and Ca I; we also allow for non-local energy deposition).

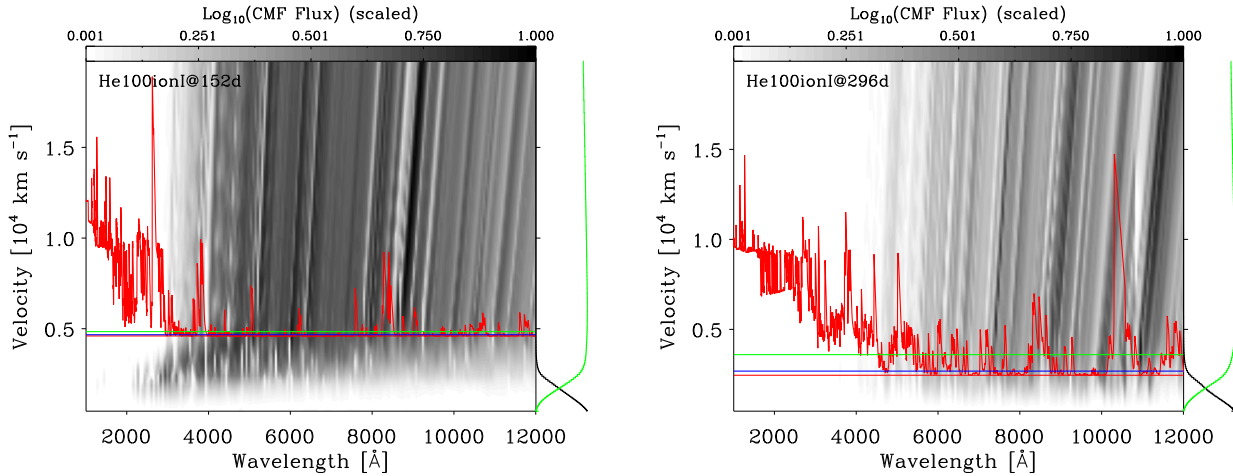


Figure 16. Variation of the co-moving frame flux versus wavelength and velocity (or depth in the ejecta) for model He100ionI at 152 (left) and 296 d after explosion (right). We also overplot the location of the photosphere that results when including all sources of opacity (jagged red line), electron scattering only (bottom red line), the Rosseland-mean opacity (blue line), or the flux-mean opacity (green line). Finally, for illustration, we show on the right side of each panel the local energy deposition from radioactive decay of ^{56}Ni nuclei (black; in $\text{erg s}^{-1} \text{cm}^{-3}$; normalized to its maximum value which occurs in the innermost shell) and the frequency-integrated CMF flux versus velocity (green). While the ^{56}Ni distribution is a given of the hydrodynamical input and thus fixed, the distribution of the energy deposition extends farther outward as time progresses and as the photospheres recedes.

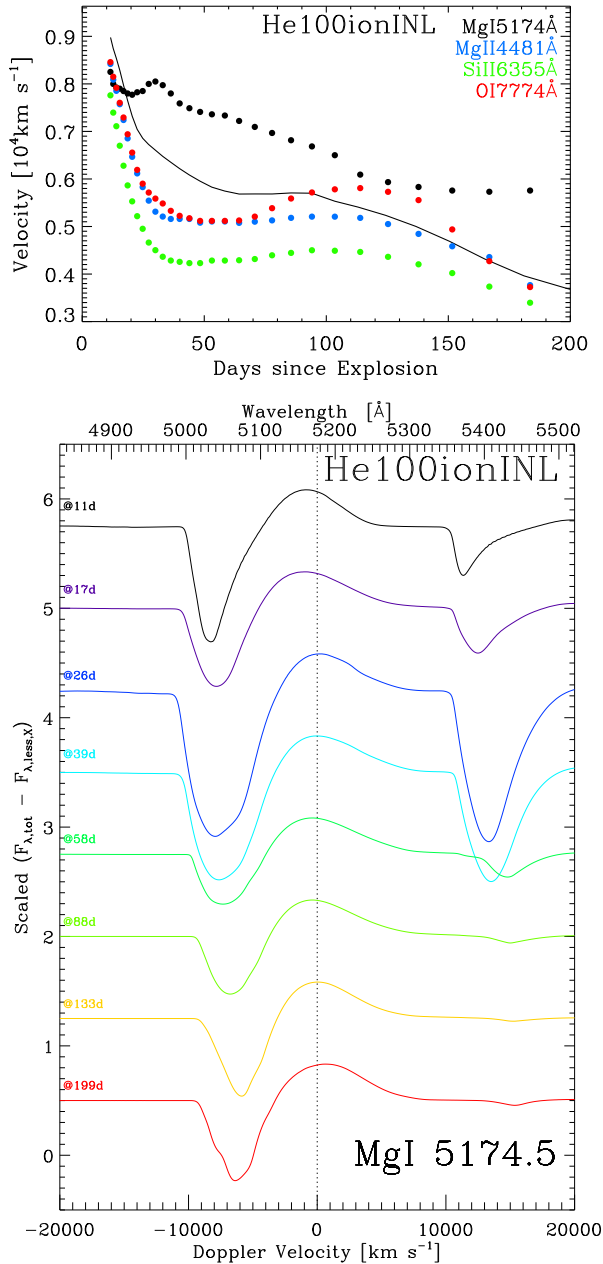


Figure 15. Same as Fig. 11, but now showing the results for model He100ionINL. We focus on early times when these lines remain optically thick.

tosphere recedes into the helium core, before it turns into a set of relatively narrow emission lines at very late times. In model B210, the larger expansion rate causes the individual emissions to overlap and form a unique emission feature — different ejecta kinetic energies and stratification yield different velocities for this emission region but the principle holds the same in all.

Interestingly, some lines appear or re-appear at the nebular phase following the revival from non-local energy deposition. The most striking example of this is the re-appearance and persistence of $H\alpha$ in model B210NL beyond 200 d, after the line had been weakening since the start of the simulations at 15 d (Fig. 13). Over

the time span 200–500 d, $H\alpha$ shows a strong P-Cygni profile, in particular with a strong and broad absorption component. We show a montage for the complete evolution of $H\alpha$ in Fig. 11 for models R190NL (left column) and B210NL (right column). At nebular times, the Doppler velocity at maximum absorption remains constant (see also the top panel in Fig. 11) and equal to the velocity at the base of the H envelope. The emission component is flat topped and its half-width also matches closely the velocity at maximum absorption. The H-deficiency in the inner ejecta (Fig. 2) together with the non-local energy deposition from γ -rays explains these properties. Note that due to strong line overlap with metal lines, $H\alpha$ is not easily seen in all RSG/BSG models. Only B210 with its enhanced heating shows it unambiguously.

In Fig. 17, we show the time evolution of the formation region for some of these lines in models R190NL and He100ionINL. The emission regions are ultimately bounded by the abundance distribution of the species under consideration, which reflect the pre-SN evolution, the regions where explosive burning took place, and the additional smearing we apply to all models (except for B210) — see Fig. 2 for details. For example, [O I] 6303–6363 Å is present in all models at very late times. The lower the model E/M , the lower the expansion velocity of the O-rich shell. We obtain representative velocities of 4000 km s^{−1} (R190 and B190), 6000 km s^{−1} (B210), and 7000 km s^{−1} (He100). Oxygen emission thus arises from regions where both the O mass fraction and the mass density are large. This emission is also influenced by optical depth effects. In model R190, O emission comes from regions with velocities extending from 1400 to 4500 km s^{−1}, while in model He100 O emission is confined to regions with velocities between 3500 and 10,000 km s^{−1}. At early times, the emission is weighted towards the outer regions because the high opacity limits the emission from the inner regions. At later times emission tends to be weighted towards the inner regions where the power source (the decay of ⁵⁶Co) resides.

In Fig. 18, we compare this segregation of line emission at nebular times in model R190. The regions of emission for the main lines evolve little with time and reflect directly the chemical stratification, yielding broad H I lines, intermediate width O I, and narrow Ca II. This is in contrast to solar-metallicity CCSNe at nebular times in which a significant fraction of the nebular line flux stems from the envelope unaffected by any nuclear burning, and thus at the primordial composition (Dessart & Hillier 2011a; Maguire et al. 2012). Similarly, in nebular-phase spectra of Type II CCSNe, $H\alpha$ generally shows a narrow profile and requires mixing into the core (Utrobin 2007; Li et al. 2012), while here the $H\alpha$ profile stems entirely from the outer H-rich shell. Mixing in those PISNe, which is expected to be inefficient (Joggerst & Whalen 2011; but see also Chen et al. 2012), should not alter this result.

6 COMPARISON TO OBSERVATIONS OF PISN CANDIDATES

6.1 SN 2007bi

Given the numerous uncertainties affecting the modeling of PISNe, our goal is to identify critical signatures from our simulations that will allow PISN candidates (e.g., SN 2007bi) to be confirmed or dismissed as a PISN. An important result of the present study has already been presented in the broader context of superluminous SNe, where we argue that PISN explosions have probably not yet been discovered (Dessart et al. 2012c).

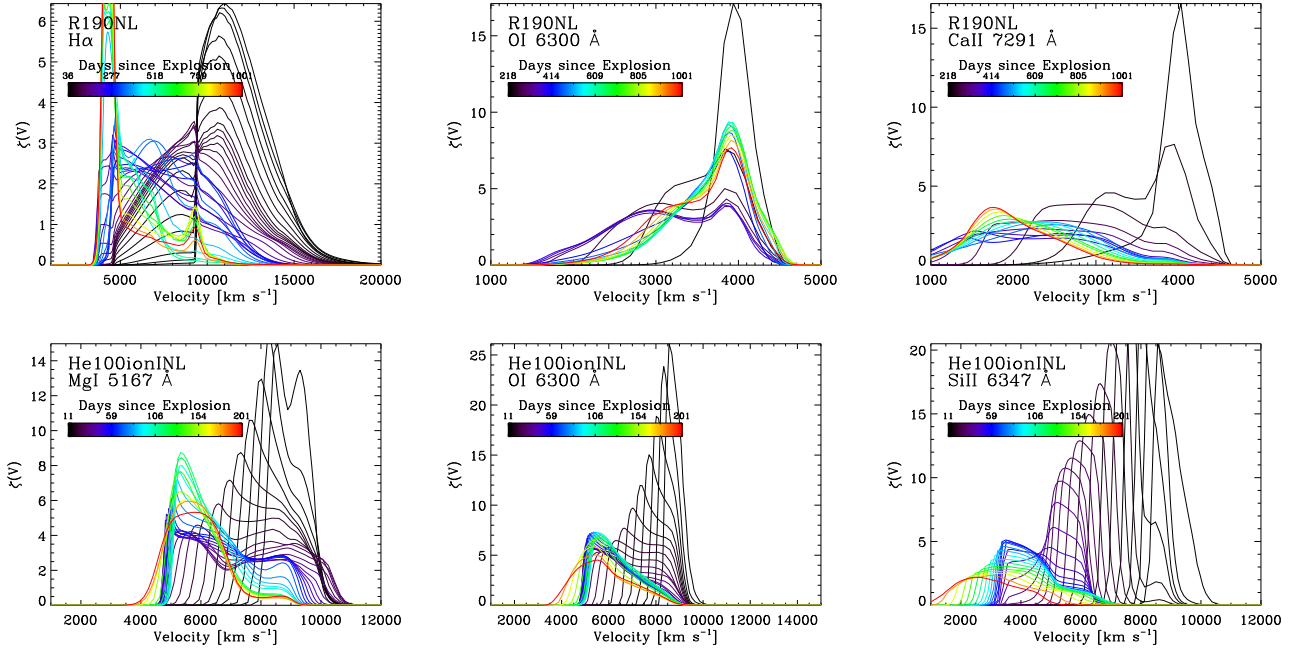


Figure 17. Illustration of the spatial distribution of emission for representative lines (for multiplets, we show the bluest component) of important ions in model R190NL (top row) and model He100ionINL (bottom row). The quantity $\xi(v)$ is defined such that the line flux is proportional to $\int \xi d(\log v)$ (Hillier 1987). The time coverage for each panel is adjusted to capture the time when the line is unambiguously present in the synthetic spectrum. We find that all lines are primarily segregated according to the chemical stratification.

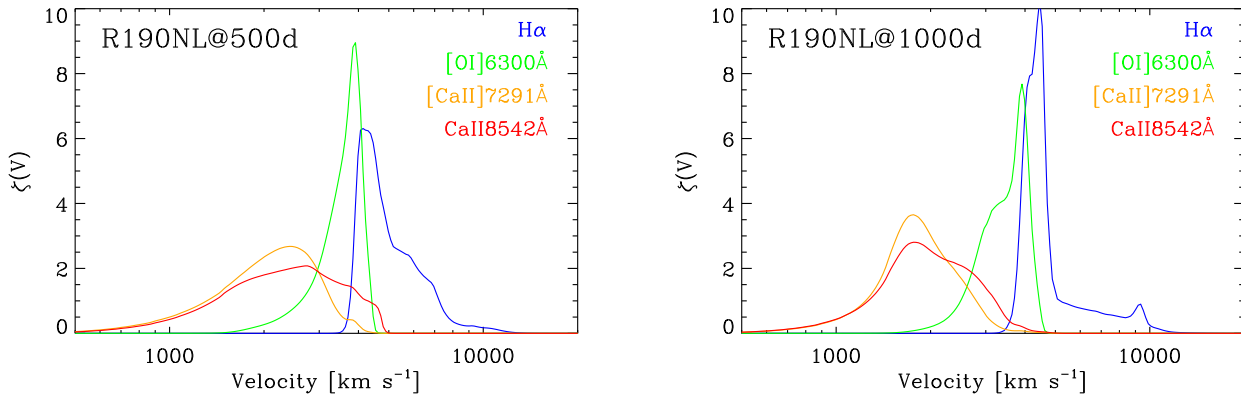


Figure 18. Comparison of the formation regions for $H\alpha$, $[O\text{I}] 6300 \text{ \AA}$, $[Ca\text{II}] 7291 \text{ \AA}$, and $Ca\text{II} 8542 \text{ \AA}$ at 500 d (left) and 1000 d (right) after explosion for model R190NL.

The observed light curve of SN 2007bi reveals a peak at $M_R \sim -21.3$ mag and a slowly decreasing nebular flux compatible with full γ -ray trapping (Gal-Yam et al. 2009). Our model He100 (or He100ionI; allowance for non-local energy deposition does not influence the results for this comparison) matches closely these light-curve properties, although our model is fainter by ~ 0.8 mag in the R band (Fig. 19). As discussed in Dessart et al. (2012c), the models He110 or He115 (corresponding to similar models to He100 but from 110 and 115 M_\odot Helium cores) match better the luminosity of SN 2007bi at and beyond the peak. However, their spectral properties are comparable to those of He100. Overall, the explosion and light-curve properties that we infer for model He100 are in agreement with the 100 M_\odot Helium-core mod-

els computed by other groups (Gal-Yam et al. 2009; Kasen et al. 2011).

Matching the light curve is a necessary step to validate a model, but it is not a sufficient test. Light-curve degeneracy is epitomized by the good quality fit obtained by Kasen & Bildsten (2010) and Kasen et al. (2011) using either a 20 M_\odot ejecta powered by a magnetar or a 100 M_\odot PISN powered by 5 M_\odot of ^{56}Ni . Modelling multi-epoch spectra is the critical next step to validate a proposed model.

For a RSG progenitor, the high-brightness phase of the PISN is during the plateau, when the spectra are crammed with H I lines. SN 2007bi is a Type Ic SN so it is unlikely to result from the explosion of a RSG star, even one endowed with few solar masses of ^{56}Ni

like our model R190. One may conceive of a contrived situation in which the SN 2007bi detection caught the ^{56}Ni bump that follows the plateau, at which time the H I lines may be weak, but why would the SN not have been detected during the preceding 200 d when the SN was even brighter in the optical?

For the BSG progenitor B190, the light curve shape is in agreement with the observations of SN 2007bi. The presence of hydrogen in the outer ejecta cannot be inferred from spectra at and beyond peak in this model (Fig. 12) so it would be at least in principle compatible with the observations of SN 2007bi and its Type Ic classification. Model B210 does show $\text{H}\alpha$ unambiguously at nebular times (Fig. 13),⁸ but it produces a too high luminosity for SN 2007bi. In model B190, the presence of an hydrogen envelope (not directly inferred from spectra at and beyond peak) leads to a smaller expansion rate of the He-core than in the He100 model. The broad line features seen in the optical spectra of SN 2007bi suggest fast expansion of the emitting layers and so, in this PISN context, would favor the lowest mass progenitor capable of producing 3–5 M_{\odot} of ^{56}Ni . Hence, our model He100 (He100ionI) seems the most suitable of all four for this PISN candidate and we therefore focus on this below.

The main spectral signatures for model He100ionI are the dominance of absorption and emission processes from IMEs in the spectra up to the peak, and a hardening of the spectrum on the rise to peak (Fig. 14). After the peak, the spectrum formation region is located within the Si/S/Fe-rich layers. The high metal content together with the cooling of the photosphere, leads to strong blanketing in the blue and a severe reddening of the spectrum. This alone is the most fundamental disagreement with the observations of SN 2007bi (Fig 19; Dessart et al. 2012c), and in fact of other superluminous SNe which seem to be systematically blue after the peak (Quimby et al. 2011). Our PISN simulations are in contradiction with this observed property. Indeed, it would be surprising for PISN explosions to retain hot photospheres free of blanketing few hundred days after explosion.

On the rise to peak, the photosphere feels the heat wave powered by decay and diffusing from greater depth, and consequently cannot feel the blanketing effects of these buried IGE; the spectra before peak are bluer. After the peak, the photosphere cools and recedes to IGE-rich layers, feeling the full effect of metal-line blanketing. The comparison made by Young et al. (2010) between typical SN Ia spectra and those of SN 2007bi reveals a striking similarity, but this similarity suggests SN 2007bi is not a PISN. In the best fitting model He100 of a 100 M_{\odot} ejecta, the ^{56}Ni mass is 5.02 M_{\odot} , thus 5% of the total mass. This is closer to the value of $\sim 1\%$ characterizing SNe II-P than the value of $\sim 50\%$ characterizing SNe Ia. As discussed in Dessart et al. (2012c), models with increasing ^{56}Ni -to-ejecta-mass ratios have bluer colors but even in the most extreme case of PISN model He125, this ratio is 0.26 and the colors are still too red to match those of SN 2007bi — this He125 model is also much too bright with its ^{56}Ni mass of 32 M_{\odot} . In the models He100–He115, which match quite well the SN 2007bi light curve, the amount of energy released per unit mass is not so favorable to produce a hot emitting ejecta at and beyond the peak of the light curve, as suggested by SN 2007bi. And indeed, our nebular-phase synthetic spectra are systematically cool and suffer severe line-blanketing dwarfing the flux short ward of $\sim 5000 \text{ \AA}$. This color mismatch can be inferred by comparing the

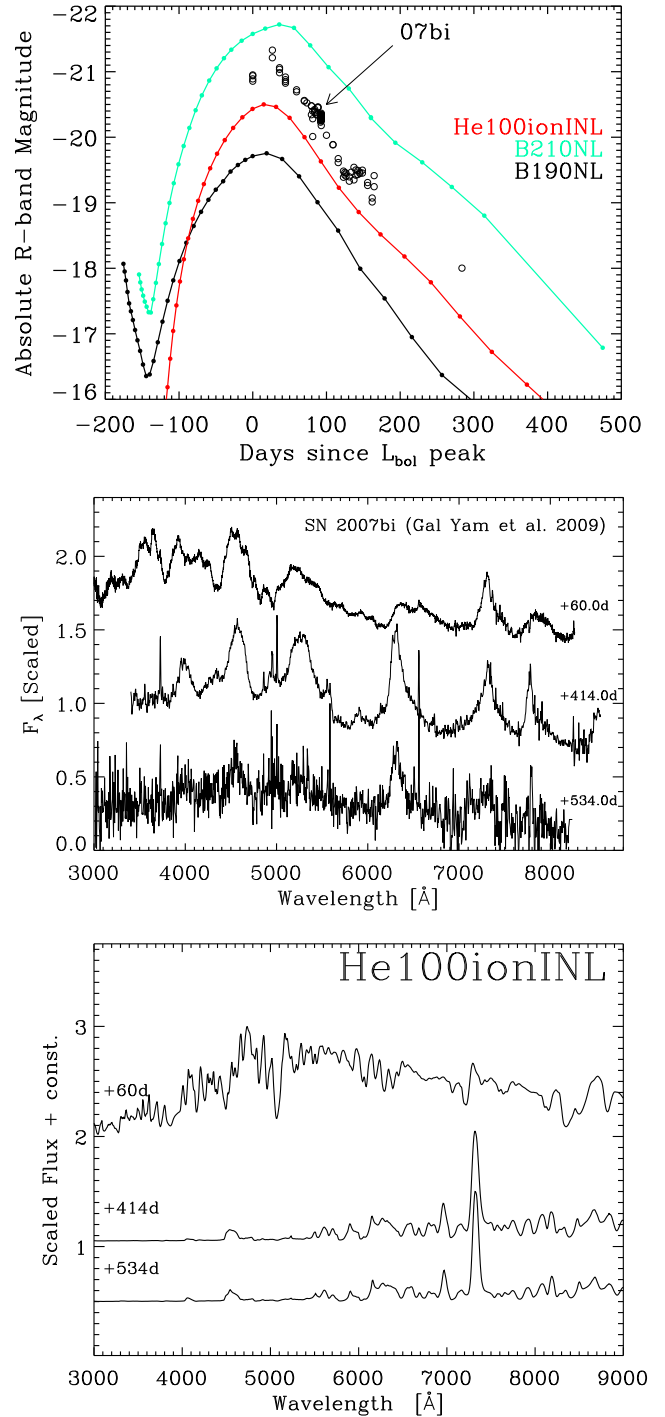


Figure 19. *Top:* R-band light curves for PISN models B190, B210, and He100, together with the observed R-band light curve of SN 2007bi (adjusted horizontally for convenience). The abscissa is the time since bolometric maximum — it differs by merely a few days from the time of R-band maximum used below. No correction for reddening is applied. *Middle:* Montage of observed spectra of SN 2007bi (Gal-Yam et al. 2009), stacked arbitrarily for visibility. Labels refer to the time since R-band maximum. *Bottom:* Montage of synthetic spectra for model He100ionINL at contemporaneous epochs.

⁸ This results from the huge ^{56}Ni production combined with non-thermal ionization and excitation, as well as non-local γ -ray-energy deposition

model He100 color $B - R$ with the observations of SN 2007bi. In the model, it is ~ 0.55 at the light curve peak and subsequently, it steadily rises to reach 2.5–3 after 200 d (Fig. 8). In contrast, the observations of SN 2007bi show a $B - R$ of ~ 0.23 mag (0.9 mag) 54 d (150 d) after peak (Young et al. 2010), hence a much bluer colour.

A further problem with the similarity between SNe Ia spectra and SN 2007bi illustrated by Young et al. (2010) is that in a PISN explosion, the ^{56}Ni is produced in the hottest and densest regions of the ejecta. In model He100, these regions are ejected at a speed $\lesssim 4000 \text{ km s}^{-1}$, while in SNe Ia these layers reach up to 15000 km s^{-1} . This strong contrast in expansion rate for the $^{56}\text{Co}/^{56}\text{Fe}$ -rich layers conflicts with this spectral similarity: metal lines in SNe Ia are broad while those in PISNe are narrow. It is also illustrated by the inconsistency of the PISN model presented in Gal-Yam et al. (2009): inferring a mass-weighted mean velocity of 8000 km s^{-1} and an ejecta mass of $100 M_{\odot}$, the explosion has to deliver $\sim 100 \text{ B}$ (note that $\sim 10 \text{ B}$ is needed to just unbind such a super-massive compact star), which is then incompatible with the inferred $3\text{--}10 M_{\odot}$ of ^{56}Ni synthesized in the explosion. For comparison, the extreme model B210 presented here releases “only” 75 B through burning, producing an ejecta with a kinetic energy of 65 B.

Kasen et al. (2011) have compared one synthetic spectrum for their He100 model at 50 d before peak with the spectrum of SN 2007bi at 54 d after peak. They do reproduce the blue spectrum but this stems from the fact that they have a 100-d mismatch. At 50 d after explosion, the color is no longer blue and the spectra are strongly line blanketed, in contradiction with the observations.

It thus seems unlikely that SN 2007bi is a PISN explosion. In addition with the issues raised by star formation (Hosokawa et al. 2011) and stellar evolution (Langer et al. 2007) for such super-massive star progenitors,⁹ we have provided independent arguments that suggest that even if PISN ejecta existed, their radiative properties would conflict in numerous ways with the observations of SN 2007bi. As we propose in Dessart et al. (2012c), we instead favor a magnetar scenario for SN 2007bi, as well as for superluminous SNe characterized by blue colors.

6.2 SN 2006gy

The spectral evolution of our H-rich PISN models (i.e., R190, B190, B210) can also be compared to that of PISN candidate SN 2006gy, whose superluminous display was associated with ^{56}Ni -power or CSM interaction (Ofek et al. 2007; Smith et al. 2007). This superluminous Type II_{in} SN reveals a spectrum dominated noticeably by H I Balmer and Fe II lines with narrow and broad velocity components (Smith et al. 2010). Its spectral morphology suggests a slow cooling of the emitting region, with little signs of line blanketing, and, surprisingly, no emission of the usual [Ca II] and [O I] nebular lines seen in massive-star explosions.

The ^{56}Ni -power vs. CSM-interaction models can be discussed further in light of our simulations. The explosion of a RSG progenitor is directly rejected from the bell-shape light-curve morphology of SN 2006gy, while the presence of hydrogen would require a blue or a yellow supergiant (in agreement with the expectations from stellar evolutionary calculations; Langer et al. 2007). However, our simulations, wherein the luminosity is powered by radioactive decay primarily, indicate that by the time the SN reaches

its peak brightness, the photosphere is in the Helium core and radiates a spectrum that contains little sign for the presence of hydrogen (models B190 and B210). The bulk of that energy arises from the core and the emission is channeled for a sizable part into those fine structure lines, which should thus be observable. The fact that SN 2006gy retained a Type II spectral morphology for hundreds of days with no signs of blanketing short ward of 5000 Å and no forbidden line emission from [Ca II] and [O I] invalidates the ^{56}Ni -power model for SN 2006gy.

7 PISN AS METALLICITY INDICATORS IN THE UNIVERSE

Being so luminous, PISN explosions represent attractive probes of the young Universe where the first stars formed. In particular, those that die as RSG stars would sustain a high luminosity in the optical from early after breakout until the transition to the nebular phase about a year later (in the SN frame). As discussed earlier (Sect. 5.1), the representative model R190 has a nearly pure H I spectrum (with small contributions from He I) with no sign of line blanketing from either IMEs or IGEs for $\gtrsim 250$ d after explosion. During that extended time, which may last a few years for an observer on earth depending on the redshift, spectroscopic observations could reveal the environmental metallicity out of which the PISN progenitor formed. At large redshift, this determination is generally done from analysis of nebular lines (Osterbrock 1989), but doing this task using the SN spectrum offers a very interesting alternative. In the present case reported, the metallicity is so low that no metal lines are seen at early times, which would be an unambiguous signature that the metallicity is extremely low. For higher metal abundances, one expects a gradual rise in associated line strengths (Kasen et al. 2011).

As we discussed in detail, in particular for model He100ionI, on the rise to peak the photosphere probes the He-rich and O-rich envelope above the IGE-rich inner ejecta and thus still reflects the primordial abundances for IGEs. After the peak, this information is all lost since we see emission/absorption from the ashes produced by steady and explosive burning. This still leaves an extended window for determining iron abundances, for example, for the primordial gas out of which the star formed.

In Fig. 20, we show how the iron mass fraction varies at the photosphere for all models, with horizontal lines indicating the levels corresponding to the SMC, the LMC, and the solar iron mass fraction. Over a few hundred days, the iron mass fraction varies in all cases over 7 orders of magnitude, i.e. from the iron-deficient outer ejecta to the pure iron layers of the inner ejecta. Note however that the primordial metallicity is preserved at the photosphere of model R190 for ~ 200 d (because the thermalization region is much deeper than the electron-scattering photosphere, metals influence the emergent spectrum of model R190 before 250 d; see Fig. 9).

8 CONCLUSION

In this paper, we have explored the radiative properties of PISNe arising from the explosion of RSG, BSG, and WR star progenitors at a very low metallicity of $10^{-4} Z_{\odot}$ and without rotation. Our approach is based on physically-consistent modeling of the evolution from the main sequence until the onset of the pair-production instability using the stellar evolution code MESA, the explosion phase

⁹ On possible way to overcome the evolution argument is through mergers in a dense star cluster, as recently discussed by Pan et al. (2012b).

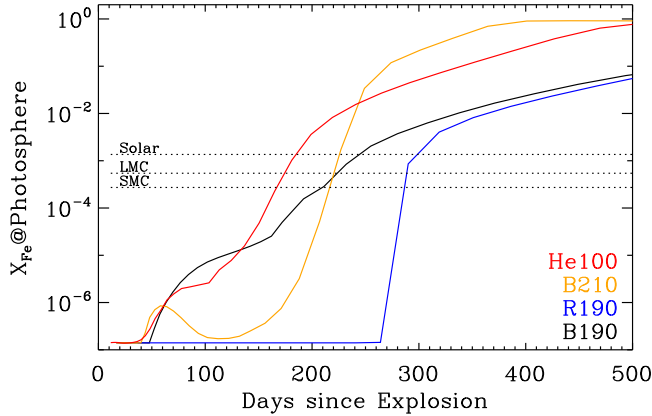


Figure 20. Illustration of the iron mass fraction at the electron-scattering photosphere versus time since explosion for each model. Two competing effects cause this quantity to generally increase with time, i.e., the photosphere recession to IGE-rich layers as time proceeds and the decay with time of ^{56}Ni and ^{56}Co isotopes. We draw a dotted horizontal line to represent the iron mass fraction in the SMC, LMC, and in the solar neighborhood. More generally, RSG-star explosions constitute an attractive probe to constrain the metallicity, especially those occurring in the early Universe.

and the evolution of the ejecta with the radiation-hydrodynamics code *Id* (with allowance for explosive burning), and the non-LTE time-dependent radiative-transfer modeling with *CMFGEN* for the multi-band light-curves and spectra from the photospheric to the nebular phase. In this paper, we have focused on this last step, while the former two steps will be described in Waldman et al. (in prep.). In practice, we focus on a $190 M_{\odot}$ RSG star (model R190), a 190 and $210 M_{\odot}$ BSG stars (models B190 and B210), and a $100 M_{\odot}$ WR star (model He100).

The exceptional progenitor and explosion properties of the PISNe we modeled set them apart from the SNe we routinely observe in the local Universe. With ejecta masses of $\gtrsim 100 M_{\odot}$, ejecta kinetic energies of few tens of B, ^{56}Ni yields of a few M_{\odot} , their luminosity peaks at $\sim 10^{10} L_{\odot}$ about 150–200 d after explosion, remaining above $\sim 10^9 L_{\odot}$ for $\gtrsim 100$ d. Their large ejecta mass ensures full γ -ray-trapping so that the ^{56}Co decay rate gives the distinctive $\sim 0.01 \text{ mag d}^{-1}$ nebular decline rate up to ~ 500 d after explosion (~ 300 d after bolometric maximum). Over the next 500 d, the fading rate slowly steepens in the lower ejecta-mass model He100 but stays the same in the more massive ejecta models.

The ingredients ruling the evolution of “standard” SNe in the local Universe apply to PISNe directly. The influence of the progenitor radius is key in yielding the high-luminosity plateau of the RSG model R190, while the more compact BSG and WR progenitors are characterized by a single highly luminous ^{56}Ni -powered peak. Furthermore, the large progenitor radius of model R190 yields a hot ionized photosphere for weeks after explosion. In the BSG model B190, recombination turns on much more quickly, as in SN 1987A. In the helium-rich model He100, the re-brightening phase to the bolometric peak corresponds to a photospheric residence in the O-rich core, with inefficient non-thermal excitation of the outer helium. Hence, our model R190 would be classified unambiguously as a SN II-P. Models B190/B210, despite having a sizable amount of H and He, would be Type IIc if observed early on (Dessart et al. 2012b) but most probably a Ic if discovered at peak or beyond.

Finally, model He100 would definitely be a Type Ic despite the $\sim 8 M_{\odot}$ of helium in its outer ejecta.

Despite these significant spectral and light-curve differences up to the bolometric peak, all models reveal very similar light-curve and spectral properties beyond it. This naturally stems from the comparable core properties of the progenitor stars — here, differences in cumulative mass for O or ^{56}Ni change little the temperature or ionization controlling the radiative properties from the core and conspire to produce this degeneracy.

Two fundamental properties emerge from PISN simulations (see also Kasen et al. 2011). First, homologous expansion in such massive ejecta implies that while the outer layers may be traveling fast, as witnessed early on from the width of the Balmer lines in the SN II-P model R190, the inner ejecta travels at relatively small speeds and should therefore lead to rather modest nebular line widths. The ^{56}Ni rich core travels at $\lesssim 2000 \text{ km s}^{-1}$ in model B190/R190 and at $\lesssim 4000 \text{ km s}^{-1}$ in models B210/He100. Hence, although these objects are thermonuclear explosions, their chemical stratification is closer to that of core-collapse SNe than SNe Ia. In practice, we find all our PISN simulations to follow this principle and reveal nebular lines with a narrow width, in particular arising from the O-rich and Ca-rich shell on top of the ^{56}Ni -rich core.

The second, perhaps counterintuitive, property of these PISNe is the relatively modest ejecta and photospheric temperatures of $\lesssim 5000 \text{ K}$ at and beyond the bolometric maximum. What controls the ejecta ionization and temperature is not just the mass of ^{56}Ni , which is admittedly large, but instead the ratio of ^{56}Ni mass to ejecta mass, which is typically quite small in these PISNe, again more typical of core-collapse SNe than SNe Ia. Indeed, the large ejecta mass means that the energy released is to be shared. This is an inevitable property of PISNe since pair-production can only occur in stars with super-massive He/CO cores. Indirectly, this increases the diffusion time of the ejecta, which becomes transparent late, at $\lesssim 200$ d in this set. By then, the ejecta has expanded to 10^{16} cm , corresponding to an increase in radius of 10^5 for the core material at that time. At such late times, ^{56}Co decay dominates, with a weaker heating rate compared to ^{56}Ni . Consequently, the PISN spectra at and beyond bolometric maximum are red, i.e., little flux is emitted shortward of $\sim 5000 \text{ \AA}$, and strongly blanketed by Fe II and eventually Fe I. This is in stark contrast with any known superluminous SN today. As we emphasize in Dessart et al. (2012c), these properties are at odds with the observations of the PISN candidate SN 2007bi (Gal-Yam et al. 2009). An attractive alternative, which needs further study, is the magnetar model whereby energy is added to a SN ejecta but without the compromising blanketing effects of metals.

The current status of PISNe today is rather grim. Recent numerical simulations indicate that super-massive stars are hard to form (Hosokawa et al. 2011). If they did form, we do not currently expect them to explode as Type Ic PISNe unless at very low Z (Langer et al. 2007). If they did form and exploded at $Z_{\odot}/3$ as a Type Ic SN, we do not expect them to resemble SN 2007bi at all, as demonstrated here, but rather display red colors and lines with a modest width at all times.

A more attractive scenario for producing blue weakly-blanketed broad-lined superluminous SNe is by the magnetar scenario, or any similar setup in which a large energy is fed into the ejecta once it has expanded to a SN size (Dessart et al. 2012c). Two effects suggest that this scenario is more amenable to explain these events. First, the formation of a magnetar involves the fast rotation of the progenitor Fe core prior to col-

lapse (Hirschi et al. 2004b; Woosley & Heger 2006; Georgy et al. 2009), which can be produced in a wide range of massive stars at LMC-like metallicities or less. We expect a diversity both in the magnetar properties and in the associated SN ejecta. Importantly, a large magnetar radiation is function of the magnetar properties and can therefore occur in combination with low- or moderate-mass ejecta. In contrast, a large ^{56}Ni mass in a PISN requires by essence a larger mass progenitor. The snow-plow effect from magnetar energy injection can thus easily alter the dynamics of the inner ejecta and lead to the formation of broad lines at nebular times (Kasen & Bildsten 2010; Woosley 2010; Dessart et al. 2012c). Mistaking such a magnetar-powered ejecta for a PISN (in homologous expansion and showing a ^{56}Ni -powered LC) would lead to a poor estimate of the ejecta mass and kinetic energy. Such inconsistencies have arisen for SN 2005bf and SN 2007bi if one assumes a super-massive ^{56}Ni -powered SN (Folatelli et al. 2006; Gal-Yam et al. 2009; Kasen et al. 2011) rather than a magnetar-powered SN (Maeda et al. 2007; Kasen & Bildsten 2010). What we demonstrate in this work is that distinguishing the two models should be done through detailed spectroscopic modeling.

Our simulations give the fundamental properties we expect for PISNe in the early Universe and stemming from non-rotating progenitor stars. Proposed PISN candidates have all been observed in the nearby Universe, at metallicities close to the solar value. At smaller metallicities, the evolution of the progenitor massive star will be altered, in ways that depend considerably on the mass loss rate. Exploratory calculations by Langer et al. (2007) suggest that H-rich PISNe are possible at metallicities as high as $Z_{\odot}/3$, but that H-deficient (Type Ic) PISNe may be limited to lower-metallicity environments. Besides the impact on the progenitor properties (and its propensity to lead to core collapse or pair production), variations in the metallicity will tend to modulate the effects of line blanketing. Based on our results, we anticipate this will play a role at early times (plateau phase in SNe II-P, pre-peak phase in SNe II-pec and Ib/c), before the photosphere recedes to the inner ejecta rich in explosively-synthesized IGEs.

A potential caveat of our simulations, to be remedied in the future, is the neglect of stellar rotation for the pre-SN evolution. The PISN channel for rotating massive Pop III stars has been recently studied by Chatzopoulos & Wheeler (2012) and Yoon et al. (2012). By increasing the stellar core mass, fast rotation can lower the minimum main-sequence mass needed to encounter the pair-production instability. Neglecting mass loss entirely, Chatzopoulos & Wheeler (2012) suggest a lower mass limit of $\sim 65 M_{\odot}$; allowing for radiation-driven mass loss from optically-thick lines of CNO elements, Yoon et al. (2012) give a lower main-sequence mass limit of $\sim 90 M_{\odot}$, corresponding to a final mass of $\sim 70 M_{\odot}$. Rotation can thus permit to produce lower mass PISN ejecta, about 30% less massive than our He100 model. Lowering the ejecta mass reduces the rise time to light-curve peak, although this shift will depend on the explosion energy and ^{56}Ni mass produced. This will diversify the PISN light-curve and spectral properties, introducing a range of peak luminosities and spectral properties. In Dessart et al. (2012c), we presented results for PISNe from He cores between 100 and 125 M_{\odot} (evolved without mass loss). These covered a huge range of ^{56}Ni mass between 5.0 and 32.4 M_{\odot} , ejecta kinetic energy between 37.6 and 74.2 B. More energetic models produced higher peak luminosities with broader spectral lines at any given epoch. However, as emphasized in Dessart et al. (2012c), the ejecta richer in ^{56}Ni have larger temperatures but suffer stronger blanketing from IGEs so that the range of colors is limited and the resulting PISN spectra are rather red. To conclude, the variations of

a few tens of percent in ejecta mass permitted by the inclusion of progenitor rotation will likely have only a modest impact on PISN radiative properties.

Ongoing and future deep systematic surveys of the sky may eventually detect unambiguously the explosion of the first stars. Given their longer high-brightness light curve and bluer colours, the explosion of RSG stars should be prime targets. Their extended and massive hydrogen-envelope would also allow the inference of the environmental metallicity in which they form. Furthermore, such RSG-star explosions could be used to determine distances out to large redshifts using the Expanding Photosphere Method (Kirshner & Kwan 1974; Eastman et al. 1996; Dessart & Hillier 2005a).

ACKNOWLEDGMENTS

LD and SB acknowledge financial support from the European Community through an International Re-integration Grant, under grant number PIRG04-GA-2008-239184, and from “Agence Nationale de la Recherche” grant ANR-2011-Blanc-SIMI-5-6-007-01. DJH acknowledges support from STScI theory grants HST-AR-11756.01.A and HST-AR-12640.01, and NASA theory grant NNX10AC80G. This work was granted access to the HPC resources of CINES under the allocation 2011-c2011046608 and c2012046608 made by GENCI (Grand Equipement National de Calcul Intensif). A subset of the computations were also performed at Caltech’s Center for Advanced Computing Research on the cluster Zwicky funded through NSF grant no. PHY-0960291 and the Sherman Fairchild Foundation.

APPENDIX A: EJECTA PROPERTIES

In this section, we present more quantitatively the photospheric and ejecta properties. We give tabulated values (Tables A1–A4) corresponding to Fig. 5 discussed in Section 4. Specifically, we give the time evolution for the radius, velocity, temperature, and overlying mass at the electron-scattering photosphere, together with the base ejecta electron-scattering optical depth.

Concerning the latter, we note that ejecta recombination induces a decline of the optical depth that is steeper than the $1/t^2$ scaling corresponding to homologous expansion. Nonetheless, the electron-scattering optical depth remains $\gtrsim 1$ for about 600 d in all four simulations. This is a rather unique property of PISN explosions, inherent to the huge progenitor/ejecta masses involved. This property may be misleading because by the time the ejecta base is optically thin, the outer ejecta has a much lower density and may thus be in a nebular regime. This hybrid configuration is reflected spectroscopically by the concomitant presence of P-Cygni profiles (associated with transitions that remain optically thick for years) and forbidden emission lines (such as the [Ca II] 7300 Å doublet). There is thus continued interaction between the radiation and the gas, but the depletion of the radiation field at short wavelength (in the bound-free continua of H/He/CNO/IMEs) is very weak and thus unable to cause much photo-ionization. At late times, γ -rays travel some distance before being absorbed, inducing non-local energy deposition. The corresponding thermal energy, and the associated non-thermal excitation and ionization, may cause the ionization to rise again.

We note that the huge energy release from decay (and the diffusion of that heat) prevent the formation of a sharp drop in

Table A1. Evolution of important quantities at the electron-scattering photosphere for model B190. By definition, these are limited to so-called photospheric epochs. They are also primarily illustrative since electron scattering becomes irrelevant as metal-line opacity increase and eventually dominate at late times.

B190					
Age	$\tau_{\text{base,es}}$	R_{phot}	V_{phot}	T_{phot}	ΔM_{phot}
[d]		[10^{15} cm]	[km s $^{-1}$]	[K]	[M_{\odot}]
16.7	8456.35	3.06	21224	5589	0.313
18.3	6805.03	3.18	20058	5318	0.412
20.2	5436.70	3.25	18627	5101	0.563
22.2	4317.84	3.23	16870	4863	0.801
24.4	3436.37	3.14	14874	4680	1.152
26.9	2754.18	2.97	12821	4549	1.650
29.5	2226.68	2.80	10954	4456	2.485
32.5	1810.37	2.66	9462	4411	7.520
35.7	1471.41	2.51	8143	4446	13.200
39.3	1180.57	2.34	6876	4453	18.964
43.2	940.03	2.03	5432	4308	28.061
47.6	750.98	1.78	4325	4225	44.386
52.3	605.75	1.86	4104	4250	50.383
57.6	493.08	1.98	3978	4376	54.026
63.3	403.21	2.12	3878	4557	56.901
69.7	329.64	2.28	3795	4752	59.300
76.6	268.23	2.47	3727	4946	61.280
84.3	219.36	2.68	3675	5128	62.839
92.7	179.38	2.91	3637	5294	63.989
102.0	146.02	3.18	3607	5447	64.867
112.0	118.34	3.46	3579	5583	65.699
122.0	96.86	3.75	3554	5688	66.461
132.0	80.21	4.02	3522	5769	67.447
142.0	66.94	4.27	3479	5830	68.769
152.0	56.06	4.50	3424	5871	70.493
162.0	46.49	4.59	3276	5855	75.231
172.0	38.57	4.70	3163	5866	78.905
182.0	31.97	4.81	3057	5869	82.450
192.0	26.73	4.89	2949	5850	86.025
211.0	19.27	5.01	2750	5735	92.428
232.0	13.32	5.18	2584	5432	97.182
255.0	9.19	5.43	2465	4938	100.306
280.0	6.41	5.71	2359	4552	102.933
308.0	4.52	5.98	2247	4277	105.600
338.0	3.43	6.24	2135	4029	108.257
371.0	2.82	6.47	2017	3677	110.939
408.0	2.31	6.66	1890	3225	113.995
448.8	1.88	6.78	1748	3037	117.161
493.7	1.51	6.78	1590	2934	120.450
543.0	1.19	6.84	1458	2835	123.780
597.0	0.96	6.80	1318	2780	127.295
657.0	0.78	5.87	1034	2891	130.894

optical depth at any time, something that is most dramatically seen in “standard” SNe II-P simulations at the end of the plateau phase (Dessart & Hillier 2011a). In that case, the transition to this nebular regime often coincides with a sharp rise in polarization (Leonard et al. 2006; Dessart & Hillier 2011b).

We also show the ionization state of the gas in Fig. A1, as it indicates which species contribute opacity at depth (thus controlling the diffusion of heat) and at the photosphere (affecting the spectrum formation). We restrict the illustration to models R190, B210, and He100ionI, and the dominant species H and/or He, O, and Fe. A generic property of these ejecta is their low ionization. This result may seem counter intuitive given the large amount of ^{56}Ni but

Table A2. Same as Table A1, but now showing the photospheric properties for model R190. Note that in the radiative-transfer model R190 the total ejecta mass is 7% more massive than the original non-homologously expanding \dot{M} input at 30 d (see Footnote 2 for details).

R190					
Age	$\tau_{\text{base,es}}$	R_{phot}	V_{phot}	T_{phot}	ΔM_{phot}
[d]		[10^{15} cm]	[km s $^{-1}$]	[K]	[M_{\odot}]
36.7	2568.10	4.35	13698	12742	0.348
40.4	2087.00	4.70	13454	11137	0.409
44.4	1699.22	5.07	13209	10240	0.483
48.9	1357.41	5.47	12960	9346	0.573
53.8	1060.76	5.90	12700	8522	0.688
59.1	827.13	6.36	12442	7851	0.829
65.0	661.70	6.85	12195	7340	0.994
71.6	541.43	7.40	11966	6945	1.177
78.7	438.99	8.00	11755	6563	1.383
86.6	348.97	8.64	11546	6149	1.627
95.2	276.88	9.31	11312	5742	1.957
104.0	217.71	9.90	11014	5507	2.488
114.0	164.08	10.44	10597	5359	3.469
124.0	127.94	10.77	10054	5198	5.015
136.0	99.02	10.97	9336	4965	9.677
150.0	73.83	11.06	8530	5028	16.744
165.0	56.21	10.75	7543	5038	21.750
181.0	40.87	10.50	6714	5049	26.307
199.0	29.22	10.29	5982	4867	29.889
218.9	19.41	10.06	5316	4466	33.147
240.8	11.69	9.69	4655	4139	38.840
264.0	7.30	6.96	3052	4610	130.108
290.0	4.70	6.44	2569	4416	144.765
319.0	3.31	6.49	2353	4131	150.075
350.9	2.67	6.66	2196	3734	153.387
386.0	2.18	6.86	2057	3395	156.586
424.6	1.78	7.07	1926	3097	159.586
467.0	1.44	7.26	1798	2956	163.258
513.7	1.15	7.38	1661	2891	166.955
565.0	0.92	7.24	1483	2897	170.969
621.5	0.75	5.68	1058	3060	175.209

it stems from the large ejecta mass which increases the diffusion time, making the SN evolve on very long time scales and turning transparent after few hundred days when the decay energy rate is small. This large mass also means this decay energy is to be shared, so that the energy released per unit mass is in fact quite comparable to what obtains in standard core-collapse SNe. Combined with the huge explosion energies, the small initial radius implies a very large expansion, associated with strong cooling from PdV work.

These curves reproduce the general morphology of ionization profiles in “standard” SN ejecta (e.g., Dessart & Hillier 2010). The fast-expanding low-density outer regions maintain a high ionization – this ionization freeze-out is in a large part a time-dependent effect (Dessart & Hillier 2008). At low velocity, radioactive decay contributes significant heating, weakly affected by radiative cooling due to the larger optical depth of the inner ejecta layers. The photosphere (marked as a filled circle in the figure) is by essence a tracer of the region bridging thick and thin conditions, and thus delimits the higher ionization ejecta at depth from the recombined conditions immediately above it. The minimum ionization is found at the photosphere up to the peak of the light curve because it suf-

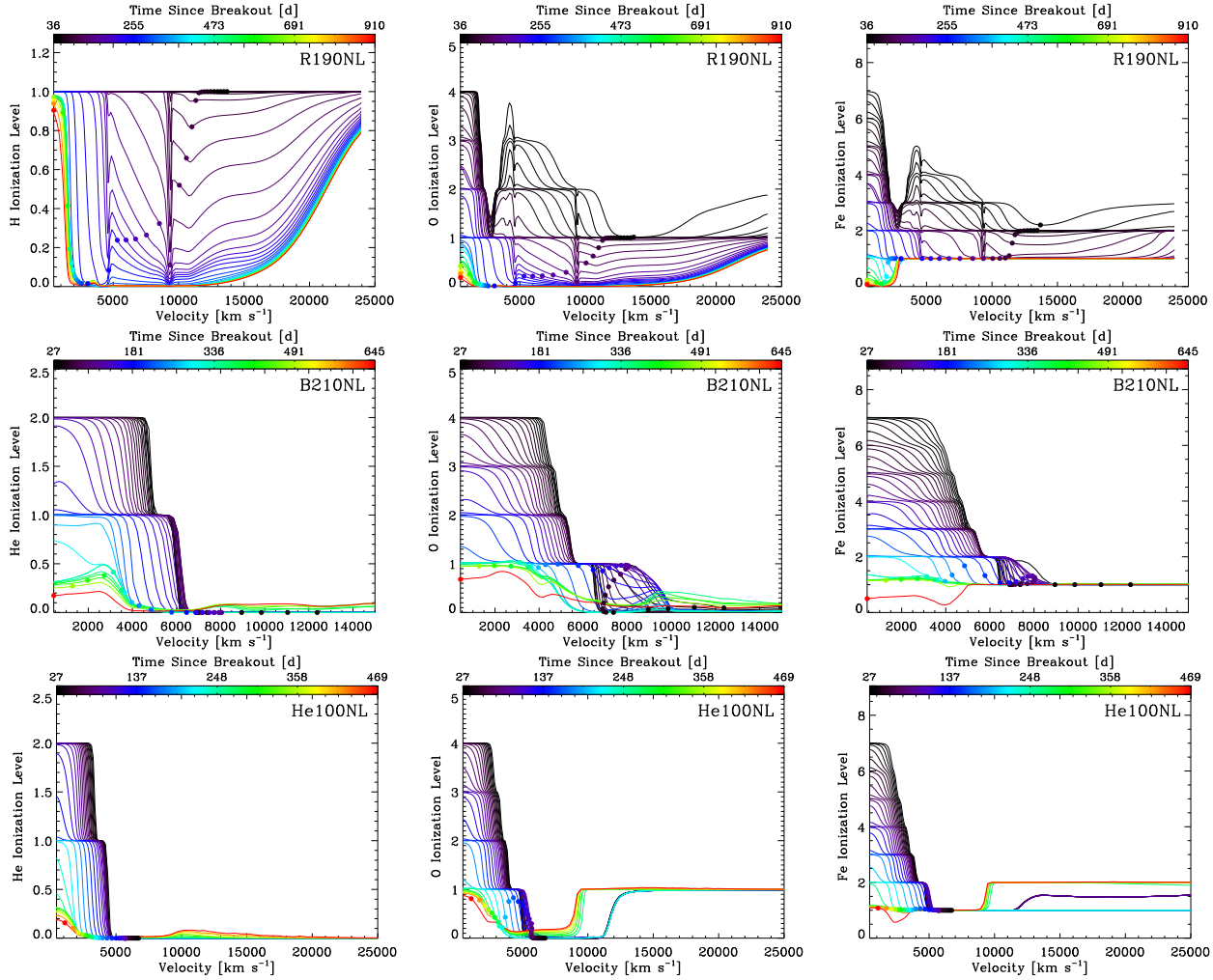


Figure A1. Evolution of the ionization state of selected species versus time (color coding) and velocity (equivalent to the depth in the ejecta) for models R190NL (top row; we show H, O, and Fe), B210NL (middle row; He, O, and Fe), and He100NL (bottom row; He, O, and Fe). An ionization level n , where n is a positive real number, for a species X means that this species X is found at that location primarily in its n^{th} -time ionized form (i.e., the ionization level is equal to $\sum_i iX^{i+} / \sum_i X^{i+}$). Along each curve, a dot represents the photospheric location at each epoch.

fers strong radiative cooling, fast expansion cooling, and weaker heating.¹⁰

Finally, we illustrate in Fig. A2 the temperature evolution of the B210 model ejecta, and in particular the presence of a reversal in the trajectory of the photosphere in velocity/mass space. This reversal is also seen in the ionization of oxygen, for example (Fig. A1). This occurs here because of the strong heating from decay. Early on, the photosphere recedes in mass until the heat wave from greater depth halts its recession, and in the present (but rare) situation, reverses that recession to outward migration. We obtained such an effect in SNe Ib/c models in which no macroscopic mixing of ^{56}Ni was applied (Dessart et al. 2011). Observationally, this may occur if a strong heat source is turned on, as in a magnetar. SN 2005bf may well have been influenced by such a delayed heat-

ing, given the observed double-peaked light curve, the reversal of the velocity at maximum absorption in He 15875 Å, and the blue colors of the spectra at late times (Maeda et al. 2007; Dessart et al. 2012c).

APPENDIX B: ATOMIC DATA SOURCES AND MODEL ATOMS

The model atoms adopted for all simulations in this work are identical to that used in Dessart & Hillier (2011a). The sources of atomic data are varied, and in many cases multiple data sets for a given ion are available. In some cases these multiple data sets represent an evolution in data quality and/or quantity, while in other cases they represent different sources and/or computational methods. Comparisons of models calculated with different data sets and atomic models potentially provide insights into the sensitivity of our results to the adopted model atoms and hydrodynamical inputs (although such calculations have yet to be undertaken for SNe).

Oscillator strengths for CNO elements were originally taken from Nussbaumer & Storey (1983, 1984). These authors also provide transition probabilities to states in the ion continuum. The

¹⁰ We note that species tend to be over-ionized when subdominant so these plots have to be interpreted with the chemical stratification in mind (Fig. 2). We also note a peculiar dip in ionization at 2000–4000 km s^{−1} in model R190, which is associated with the O-rich shell: This shell is highly-bound but ^{56}Ni deficient so that at early times when diffusion is inhibited the corresponding layers evolve adiabatically and cool tremendously by expanding from their small original radius.

Table A3. Same as Table A1, but now showing the photospheric properties for model B210.

B210					
Age	$\tau_{\text{base,es}}$	R_{phot}	V_{phot}	T_{phot}	ΔM_{phot}
[d]		[10^{15} cm]	[km s $^{-1}$]	[K]	[M_{\odot}]
16.8	3806.45	3.08	21214	5453	0.491
18.5	3090.62	3.12	19555	5155	0.605
20.3	2496.34	3.07	17476	4934	0.786
22.4	2009.13	2.98	15414	4741	1.362
24.6	1631.11	2.93	13793	4645	2.656
27.1	1329.80	2.90	12380	4601	5.131
29.8	1085.34	2.84	11041	4582	7.947
32.8	876.82	2.79	9849	4565	11.126
36.1	707.42	2.79	8951	4550	14.555
39.7	572.21	2.53	7373	4704	26.563
43.6	461.90	2.65	7031	5102	35.364
48.0	373.02	2.87	6922	5421	39.163
52.8	302.94	3.15	6894	5699	40.280
58.1	246.63	3.47	6920	5935	39.177
63.9	199.83	3.87	7002	6117	36.066
70.3	160.92	4.34	7152	6245	31.235
77.3	129.92	4.94	7393	6360	25.803
85.0	105.40	5.66	7695	6526	21.755
93.6	85.15	6.41	7929	6687	19.797
102.0	69.46	7.08	8038	6776	19.035
112.0	55.20	7.78	8038	6823	19.055
122.0	44.78	8.36	7933	6820	19.792
132.0	36.76	8.81	7728	6715	21.504
142.0	30.26	9.20	7495	6589	24.283
156.0	22.26	9.68	7181	6387	30.617
171.0	17.00	10.15	6873	6242	41.190
188.0	13.15	10.49	6455	6264	58.370
207.0	9.81	10.33	5777	6502	80.717
227.0	6.83	9.51	4849	6785	100.010
249.0	4.90	9.23	4288	6405	110.797
273.9	3.79	9.40	3971	5895	117.728
301.3	2.81	9.47	3639	5578	124.344
331.4	1.77	8.98	3136	5502	130.862
364.5	1.42	7.92	2515	5454	136.697
401.0	1.16	6.78	1956	5294	141.143
441.1	0.95	5.46	1432	5099	144.326
485.2	0.78	3.69	881	4880	146.294
533.7	0.63	2.00	433	4621	146.849
587.1	0.51	2.20	433	4320	146.833

largest source of oscillator data is from Kurucz (2009, 2010); its principal advantage over many other sources (e.g., Opacity Project) is that LS coupling is not assumed. More recently, non-LS oscillator strengths have become available through the Iron Project (Hummer et al. 1993), and work done by the atomic-data group at Ohio State University (Nahar 2010). Other important sources of radiative data for Fe include Becker & Butler (1992, 1995a,b), Nahar (1995). Atomic data from the opacity project comes from TOPBASE (Cunto et al. 1993). Energy levels have generally been obtained from National Institute of Standards and Technology. Collisional data is sparse, particularly for states far from the ground state. The principal source for collisional data among low lying states for a variety of species is the tabulation by Mendoza (1983); other sources include Berrington et al. (1985), Lennon et al. (1985), Lennon & Burke (1994), Shine & Linsky (1974), Tayal (1997a,b), Zhang & Pradhan (1995a; 1995b; 1997). Photoionization data is taken from the Opacity Project (Seaton

Table A4. Same as Table A1, but now showing the photospheric properties for model He100.

He100					
Age	$\tau_{\text{base,es}}$	R_{phot}	V_{phot}	T_{phot}	ΔM_{phot}
[d]		[10^{15} cm]	[km s $^{-1}$]	[K]	[M_{\odot}]
11.6	6433.32	0.90	8977	5183	8.295
12.7	5215.37	0.96	8746	4992	9.262
14.0	4236.04	1.03	8535	4926	10.345
15.4	3449.59	1.10	8284	4861	11.927
16.9	2816.45	1.17	7979	4791	14.178
18.6	2300.95	1.23	7650	4742	16.979
20.5	1875.86	1.29	7319	4699	20.203
22.5	1524.64	1.37	7046	4598	23.147
24.8	1237.52	1.47	6855	4435	25.342
27.2	1005.06	1.58	6726	4275	26.909
30.0	818.25	1.71	6604	4207	28.425
33.0	666.34	1.85	6475	4237	30.085
36.3	541.71	1.99	6351	4327	31.746
39.9	438.67	2.14	6218	4465	33.583
43.9	355.25	2.31	6084	4621	35.513
48.3	288.98	2.48	5953	4800	37.467
53.1	235.24	2.68	5828	4984	39.364
58.4	190.65	2.90	5746	5166	40.677
64.3	153.97	3.16	5683	5333	41.662
70.7	124.85	3.47	5685	5470	41.650
77.8	101.46	3.82	5684	5597	41.661
85.6	81.86	4.22	5706	5704	41.316
94.1	65.21	4.64	5700	5804	41.418
103.5	51.21	4.95	5532	5876	44.158
113.0	41.30	5.28	5409	5954	46.228
124.3	32.20	5.62	5235	6022	49.186
136.7	24.34	5.91	5002	6075	53.297
150.4	17.93	6.10	4691	6150	58.696
165.0	13.51	6.15	4314	6189	64.763
181.0	10.05	6.20	3962	6055	69.968
199.0	7.04	6.35	3691	5704	73.820
219.0	5.10	6.56	3464	5286	76.981
240.9	3.80	6.74	3236	4953	80.037
265.0	2.79	6.86	2995	4750	83.083
291.5	2.05	6.90	2741	4641	86.162
320.6	1.68	6.89	2488	4575	89.257
352.7	1.38	6.80	2230	4518	92.417
388.0	1.13	6.44	1919	4466	95.531
426.8	0.93	5.47	1482	4435	98.325
469.5	0.76	3.68	906	4398	100.230
516.5	0.62	2.03	455	4240	100.789
568.1	0.50	2.23	455	3970	100.789
624.9	0.40	2.46	455	3701	100.789

1987; Cunto et al. 1993), the Iron Project (Hummer et al. 1993; Nahar & Pradhan 1996), and Nahar & Pradhan (1993). Unfortunately Ni and Co photoionization data is generally unavailable, and we have utilized crude approximations. Charge exchange cross-sections are from the tabulation by Kingdon & Ferland (1996). Atomic data for C IV was obtained from Leibowitz (1972); Peach et al. (1988), and for the carbon isoelectronic sequence from Luo & Pradhan (1989). Collision strengths for Ar II are from Tayal & Henry (1996). The LS Ne I photoionization cross-sections were modified according to Seaton (1998). The same procedure was applied to using Ar I mixing coefficients computed at <http://aphysics2.lanl.gov/tempweb/lanl>. Additional data for Ne I was obtained from the MCHF/MCDHF web site: <http://nlte.nist.gov/MCHF>.

Table B1. Summary of the model atoms used in our PISN calculations with CMFGEN (H is not included in model He100). N_f refers to the number of full levels, N_s to the number of super levels, and N_{trans} to the corresponding number of bound-bound transitions. The last column refers to the upper level for each ion treated. At late times, we exclude the high ionization stages and simultaneously increase the number of levels for Fe I and Fe II. After a few hundred days, we also split the lower 5, 10, or 15 super-levels to account explicitly for more processes between low-lying states of IGEs. nw^2W refers to a state with principal quantum number n (all l states combined into a single state), and spin 2. Similarly, $8z^1Z$ refers to the $n = 8$ state with high l states (usually $l = 4$ and above) combined and spin 1.

Species	N_f	N_s	N_{trans}	Upper Level
H I	30	20	435	$n = 30$
He I	51	40	374	$n = 11$
He II	30	13	435	$n = 30$
C I	26	14	120	$2s2p^3\ ^3P^o$
C II	26	14	87	$2s^24d\ ^2D_{5/2}$
C III	112	62	891	$2s8f\ ^1F_o$
C IV	64	59	1446	$n = 30$
O I	51	19	214	$2s^22p^3(^4S^o)4f\ ^3F_3$
O II	111	30	1157	$2s^22p^2(^3P)4d\ ^2D_{5/2}$
O III	86	50	646	$2p4f\ ^1D$
O IV	72	53	835	$2p^2(^3P)3p\ ^2P^o$
Ne I	139	70	1587	$2s^22p^5(^2P^o_{3/2})6d\ ^2[5/2]_3^o$
Ne II	91	22	1106	$2s^22p^4(^3P)4d\ ^2P_{3/2}$
Ne III	71	23	460	$2s^22p^3(^2D^o)3d\ ^3S_1$
Na I	71	22	1614	$30w\ ^2W$
Mg I	122	39	1486	$3s15w\ ^1W$
Mg II	65	22	1452	$30w\ ^2W$
Mg III	99	31	775	$2p^57s\ ^1P$
Si I	187	100	4329	$3s^23p(^2P^o_{3/2})6g\ ^2[5/2]_2^o$
Si II	59	31	354	$3s^27g\ ^2G_{7/2}$
Si III	61	33	310	$3s5g\ ^1G_4$
Si IV	48	37	405	$10f\ ^2F_o$
S I	322	106	8540	$3s^23p^3(^4S)10f\ ^3F_4$
S II	324	56	8208	$3s3p^3(^5S^o)4p\ ^6P$
S III	98	48	837	$3s3p^2(^2D)3d\ ^3P$
S IV	67	27	396	$3s3p(^3P^o)4p^2D_{5/2}$
Ar I	110	56	1541	$3s^23p^5(^2P^o_{3/2})7p\ ^2[3/2]_2$
Ar II	415	134	20197	$3s^23p^4(^3P_1)7i\ ^2[6]_{11/2}$
Ar III	346	32	6898	$3s^23p^3(^2D^o)8s\ ^1D^o$
Ca I	98	76	688	$4s8z\ ^1Z$
Ca II	77	21	1736	$3p^630w\ ^2W$
Ca III	40	16	108	$3s^23p^55s\ ^1P$
Ca IV	69	18	335	$3s3p^3(^3P^o)3d\ ^4D^o_{1/2}$
Fe I	136	44	1900	$3d^6(^5D)4s4p\ ^5F^o_3$
Fe II	827	275	44831	$3d^5(^6S)4p^2(^3P)\ ^4P_{1/2}$
Fe III	607	69	9794	$3d^5(^4D)6s^3D_2$
Fe IV	1000	100	72223	$3d^4(^3G)4f\ ^4P_{5/2}$
Fe V	191	47	3977	$3d^3(^4F)4d\ ^5F_3$
Fe VI	433	44	14103	$3p^5(^2P)3d^4(^1S)^2P_{3/2}$
Fe VII	153	29	1753	$3p^5(^2P)3d^3(^3D)\ ^1P^o_1$
Co II	1000	81	61986	$3d^7(^4F)4f\ ^5F^o_4$
Co III	1000	72	68462	$3d^6(^5D)5f\ ^4F_{9/2}$
Co IV	1000	56	69425	$3d^5(^2D)5s\ ^1D_2$
Co V	387	32	13605	$3d^4(^3F)4d\ ^2H_{9/2}$
Co VI	323	28	9608	$3d^3(^2D)4d\ ^1S_0$
Co VII	319	31	9096	$3p^5(^2P^o)3d^4(^3F)\ ^2D^o_{3/2}$
Ni II	1000	59	51707	$3d^8(^3F)7f\ ^4I^o_{9/2}$
Ni III	1000	47	66486	$3d^7(^2D)4d\ ^3S_{b1}$
Ni IV	1000	54	72898	$3d^6(^5D)6p\ ^6F_{11/2}$
Ni V	183	46	3065	$3d^5(^2D)3d\ ^3F^o_3$
Ni VI	314	37	9569	$3d^4(^5D)4d\ ^4F_{9/2}$
Ni VII	308	37	9225	$3d^3(^2D)4d\ ^3P_2$

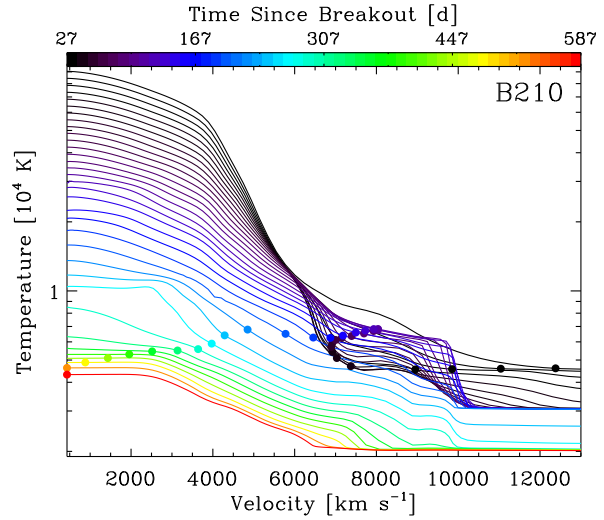


Figure A2. Evolution of the ejecta temperature for model B210 from 25 until ~ 600 d after explosion. The dots refer to the location of the electron-scattering photosphere and highlight the non-monotonic behavior of the photospheric location within the ejecta. Indeed, the strong heat wave powered by the decay energy from $21.3 M_{\odot}$ of ^{56}Ni causes the photosphere to migrate outwards in mass (or velocity) between 50 and 100 d after explosion. This behavior, unique to model B210, is seen in both mass and velocity at the photosphere in Fig. 5. Note that despite the huge ^{56}Ni mass, the temperature at a few hundred days after explosion is $\lesssim 5000$ K throughout the ejecta.

APPENDIX C: DEPENDENCY ON MODEL ATOMS

The main impact of increasing the size of the model atoms in our simulations, in particular for metals, is to enhance the magnitude of line blanketing, which tends to make the SED redder. This effect is generally weaker than obtained here through variations in composition between models or versus time (i.e., H vs. IMEs, IMEs vs. IGEs etc.), although it noticeably alters the colors after the light-curve peak.

For the early-time simulations of models R190, B190, and B210, the photosphere is located in essentially a pure Hydrogen/Helium plasma. Line blanketing effects are negligible and there is no concern with the opacity of IMEs and IGEs and the completeness of our model atoms at such early times.

However, as the photosphere recedes to deeper layers in the ejecta where IMEs and IGEs are abundant the completeness of model atoms becomes a central concern for the reliability of our predictions. After much experimentation in past simulations (Dessart & Hillier 2010, 2011a; Li et al. 2012; Dessart et al. 2012d), we have converged to an adequate assignment for the number of full and super levels to include (for a discussion on our super-level approach, see Hillier & Miller 1998). Recently, we emphasized the critical need of including Fe I in simulations of Type II SNe (Li et al. 2012), while earlier on we found that Sc and Ti play a critical role in optical spectra of SNe II-P (Dessart & Hillier 2011a).

In ejecta dominated by metals, the situation is more complicated than in type II SNe. To reach a reliable radiative-transfer result, we first find that more levels need to be included. Secondly, while we typically include in the non-LTE solver all the metal line transitions with a statistical weight greater than 0.002, we find that we now need to go down to 10^{-4} .¹¹ This means treating many

¹¹ This cut only applies to elements beyond Ne in the periodic table, does

more lines in total, which increases the computation time. Finally, in the course of this study started with models R190, B190, B210, and He100, we found that the ejecta were rather cold at the nebular phase, and for the compact progenitors, these conditions were also cold prior to re-brightening at early times. Because of the dominance of IMEs in the corresponding emitting layers, we have run a companion model, named He100ionI, identical to He100 (which has the same model atoms as R190 etc), but now including the neutral states for species Mg, Si, S, and Ca. We compare these two sequences at selected post-explosion times in Fig. C1.

The bolometric light curve is largely insensitive to the addition of these neutral atoms. We understand this from the fact that the light curve is primarily conditioned by the diffusion of heat through the optically-thick layers of the ejecta. These shells tend to be ionized and hot, and thus dominated by more ionized species. The only slight change occurs at very early times, prior to re-brightening, when the photosphere is very cold (i.e., ~ 4000 K; Fig. 5). At such times, the blanketing from neutral species is actually huge, because of the IME-rich photosphere, but also because the IGEs are under abundant compared to their solar-metallicity value. Hence, these neutral species act as an overlying blanketing layer, modifying the blocking power of the last-scattering layer. The blanketing is in part due to lines, especially in the optical and the near-IR, but more importantly stems from bound-free opacity from the ground and excited states (note in particular the photo-ionization edge of Mg I at 3757 \AA) of the corresponding ions (see also the continuum curve in Fig. 14). As the photosphere heats up on the rise to peak, species become once-ionized and the difference between models He100 and He100ionI weakens, essentially limited to the presence of the strong Mg I 5173 \AA line.

However, as the SN light curve passes its peak, the color reddens again and the photosphere cools down to 4000 K within $100\text{--}200$ d. The SN becomes nebular and blanketing from neutral species turns back on. At nebular times, additional blanketing reddens the SED below 5500 \AA , but also impacts the long wavelength range. This stems indirectly from the impact on the blanketed radiation field. It also arises directly from additional optically-thick lines from Mg I, Si I or S I.

As discussed above, metal line blanketing is irrelevant up to the peak because the composition really becomes IGE dominated at the photosphere only then. So, to expedite our very time consuming simulations, we have used modest-sized iron model atoms up to the peak (Fe I [136,44] and Fe II [115,50]), improved it early after the peak (Fe I [136,44] and Fe II [827,275]), and finally used huge model atoms for both at later times (Fe I [1142,413] and Fe II [827,275]) — the numbers in square brackets represent the number of full and super levels. This choice of model atoms yields converged results in our SNe Ia simulations (Dessart et al. 2012a) and we expect the same level of accuracy to be reached in those similarly metal-rich PISN ejecta at late times.

not apply to the lowest n levels (n is typically 9), and we only cut a transition when there is at least m (m is typically 9) stronger downward transitions from the level. Thus, this procedure does not cut important transitions to ground levels, and forbidden and semi-forbidden transitions among low-lying states.

APPENDIX D: LOG OF MAGNITUDES FOR EACH PISN MODEL

To complement the discussion on the colors of our PISN simulations, we present in Tables D1–D4 the magnitudes and luminosities (bolometric and UVOIR, i.e., integrated flux from the blue edge of the U band to the red edge of the I band). From these, one can easily infer various bolometric corrections and compare to observations.

REFERENCES

- Arnett, W. D., Bahcall, J. N., Kirshner, R. P., & Woosley, S. E. 1989, *ARA&A*, 27, 629
- Baraffe, I., Heger, A., & Woosley, S. E. 2001, *ApJ*, 550, 890
- Barkat, Z., Rakavy, G., & Sack, N. 1967, *Phys. Rev. Lett.*, 18, 379
- Becker, S. R. & Butler, K. 1992, *A&A*, 265, 647
- . 1995a, *A&A*, 294, 215
- . 1995b, *A&A*, 301, 187
- Berrington, K. A., Burke, P. G., Dufton, P. L., & Kingston, A. E. 1985, *Atomic Data and Nuclear Data Tables*, 33, 195
- Blinnikov, S., Lundqvist, P., Bartunov, O., Nomoto, K., & Iwamoto, K. 2000, *ApJ*, 532, 1132
- Bonnell, I. A. & Bate, M. R. 2005, *MNRAS*, 362, 915
- Bromm, V., Coppi, P. S., & Larson, R. B. 2002, *ApJ*, 564, 23
- Caffau, E., Bonifacio, P., François, P., Spite, M., Spite, F., Zaggia, S., Ludwig, H.-G., Steffen, M., Mashonkina, L., Monaco, L., Sbordone, L., Molaro, P., Cayrel, R., Plez, B., Hill, V., Hammer, F., & Randich, S. 2012, *A&A*, 542, A51
- Castor, J. I., Abbott, D. C., & Klein, R. I. 1975, *ApJ*, 195, 157
- Cayrel, R., Depagne, E., Spite, M., Hill, V., Spite, F., François, P., Plez, B., Beers, T., Primas, F., Andersen, J., Barbuy, B., Bonifacio, P., Molaro, P., & Nordström, B. 2004, *A&A*, 416, 1117
- Chatzopoulos, E. & Wheeler, J. C. 2012, *ApJ*, 748, 42
- Chen, K. J., Heger, A., & Almgren, A. 2012, in *Astronomical Society of the Pacific Conference Series*, Vol. 453, *Advances in Computational Astrophysics: Methods, Tools, and Outcome*, ed. R. Capuzzo-Dolcetta, M. Limongi, & A. Tornambè, 115
- Chieffi, A. & Limongi, M. 2004, *ApJ*, 608, 405
- Clark, P. C., Glover, S. C. O., Klessen, R. S., & Bromm, V. 2011, *ApJ*, 727, 110
- Cohen, J. G., Christlieb, N., McWilliam, A., Sheckman, S., Thompson, I., Melendez, J., Wisotzki, L., & Reimers, D. 2008, *ApJ*, 672, 320
- Cox, J. P. & Giuli, R. T. 1968, *Principles of stellar structure*
- Crowther, P. A., Schnurr, O., Hirschi, R., Yusof, N., Parker, R. J., Goodwin, S. P., & Kassim, H. A. 2010, *MNRAS*, 408, 731
- Cunto, W., Mendoza, C., Ochsnein, F., & Zeppen, C. J. 1993, *A&A*, 275, L5
- Davidson, K. & Humphreys, R. M. 1997, *ARA&A*, 35, 1
- de Jager, C., Nieuwenhuijzen, H., & van der Hucht, K. A. 1988, *A&AS*, 72, 259
- Dessart, L., Blondin, S., Brown, P. J., Hicken, M., Hillier, D. J., Holland, S. T., Immler, S., Kirshner, R. P., Milne, P., Modjaz, M., & Roming, P. W. A. 2008, *ApJ*, 675, 644
- Dessart, L., Hillier, D., Blondin, S., & Khokhlov, A. 2012a, *MNRAS*, in preparation
- Dessart, L. & Hillier, D. J. 2005a, *A&A*, 439, 671
- . 2005b, *A&A*, 437, 667
- . 2008, *MNRAS*, 383, 57
- . 2010, *MNRAS*, 405, 2141
- . 2011a, *MNRAS*, 410, 1739

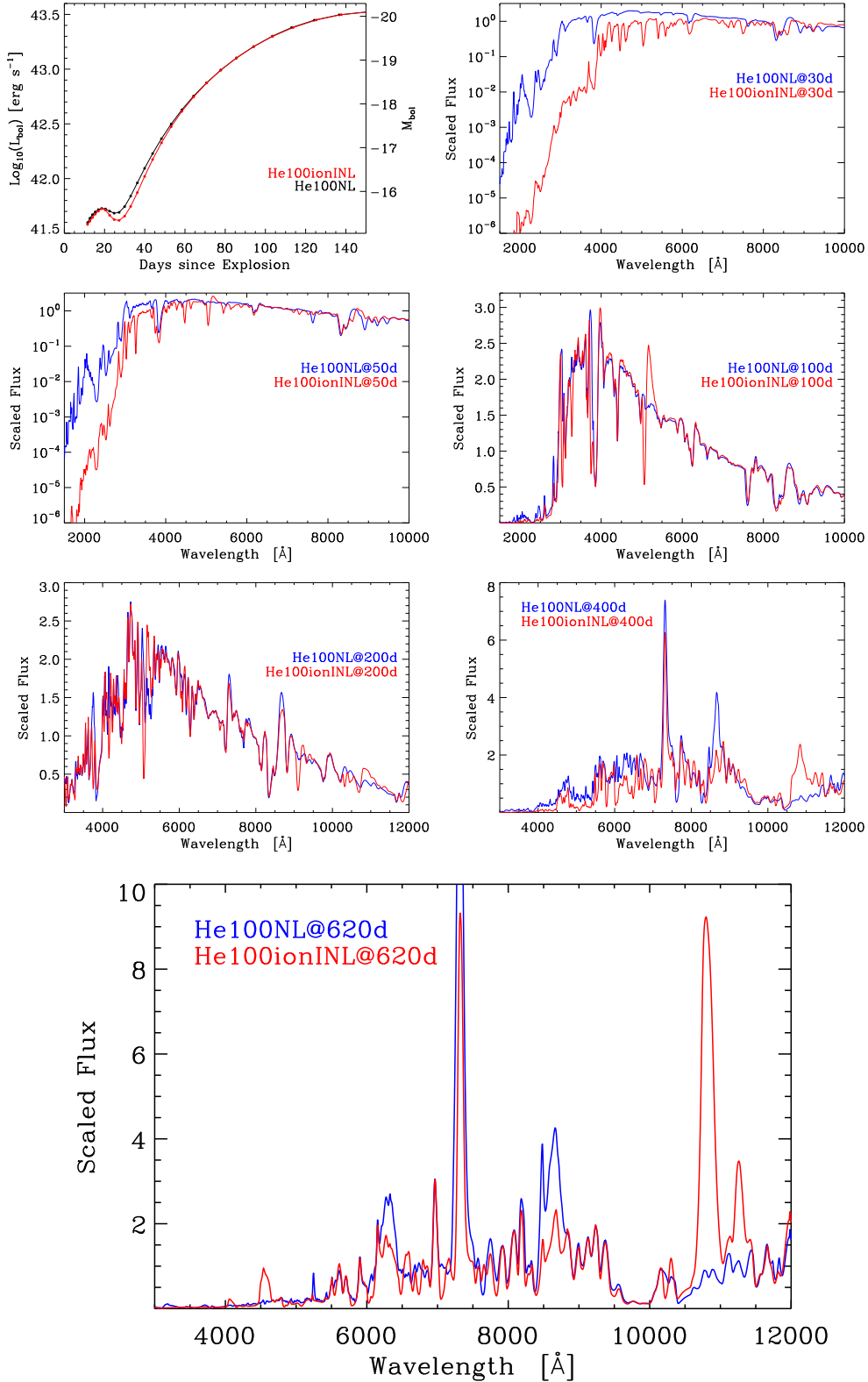


Figure C1. Illustration of the changes to the bolometric light curve (top left) and the spectra (subsequent panels, showing snapshots at 30, 50, 100, 200, 400, and 620 d after explosion) for the ejecta model He100ionINL, which treats the neutral species Mg I, Ca I, Si I, and S I, with model He100NL, which ignores them. Under favorable ionization conditions, these additional neutral states can increase the magnitude of line blanketing and bound-free opacity. Notice at nebular times the impact on the strength of the [Ca II] 7300 \AA doublet (He100NL), reduced by the overlap with Ca I lines at 7148 and 7326 \AA (He100ionNL). Opacity effects are associated with line blanketing and photo-ionization cross sections, and are strongly modulated by the ionization state at the photosphere.

Table D1. Bolometric and UVOIR luminosities as well as synthetic magnitudes for PISN model B190NL. The UVOIR luminosity corresponds to the integrated flux over the wavelength interval 3000–9200 Å, i.e., from the blue edge of the U band to the red edge of the I band.

Age (d)	L_{bol} (erg s ⁻¹)	L_{UVOIR} (erg s ⁻¹)	M_{bol} (mag)	M_{U} (mag)	M_{B} (mag)	M_{V} (mag)	M_{R} (mag)	M_{I} (mag)	M_{J} (mag)	M_{H} (mag)	M_{K} (mag)
16.67	3.4929e+42	2.2666e+42	-17.651	-16.568	-16.938	-17.578	-18.068	-18.129	-18.560	-18.677	-18.926
18.34	3.0239e+42	1.9194e+42	-17.495	-16.028	-16.691	-17.401	-17.951	-18.011	-18.506	-18.618	-18.900
20.17	2.6104e+42	1.6095e+42	-17.335	-15.449	-16.419	-17.207	-17.814	-17.876	-18.429	-18.534	-18.849
22.19	2.1978e+42	1.3107e+42	-17.148	-14.824	-16.111	-16.960	-17.638	-17.701	-18.310	-18.408	-18.755
24.41	1.8688e+42	1.0867e+42	-16.972	-14.222	-15.816	-16.764	-17.464	-17.540	-18.176	-18.274	-18.633
26.85	1.6860e+42	9.7437e+41	-16.860	-13.851	-15.654	-16.661	-17.344	-17.458	-18.068	-18.187	-18.528
29.54	1.5034e+42	8.6590e+41	-16.736	-13.739	-15.543	-16.501	-17.210	-17.338	-17.935	-18.081	-18.403
32.49	1.3165e+42	7.5756e+41	-16.592	-13.666	-15.430	-16.344	-17.058	-17.181	-17.784	-17.944	-18.254
35.74	1.1436e+42	6.6064e+41	-16.439	-13.570	-15.324	-16.189	-16.901	-17.018	-17.624	-17.788	-18.093
39.32	9.6780e+41	5.7329e+41	-16.258	-13.577	-15.206	-16.009	-16.739	-16.842	-17.428	-17.480	-17.826
43.25	7.5661e+41	4.7465e+41	-15.990	-13.855	-14.965	-15.849	-16.531	-16.629	-17.056	-17.097	-17.410
47.58	6.6828e+41	4.3700e+41	-15.856	-14.454	-14.928	-15.837	-16.355	-16.518	-16.850	-16.976	-17.177
52.34	7.2292e+41	4.8332e+41	-15.941	-14.920	-15.111	-15.981	-16.380	-16.608	-16.907	-17.071	-17.229
57.57	9.0472e+41	6.1748e+41	-16.184	-15.382	-15.452	-16.244	-16.584	-16.840	-17.113	-17.286	-17.426
63.33	1.2072e+42	8.4140e+41	-16.498	-15.860	-15.854	-16.561	-16.870	-17.130	-17.373	-17.551	-17.682
69.66	1.6449e+42	1.1691e+42	-16.833	-16.338	-16.261	-16.897	-17.185	-17.436	-17.652	-17.830	-17.958
76.63	2.2447e+42	1.6236e+42	-17.171	-16.804	-16.656	-17.231	-17.504	-17.740	-17.931	-18.108	-18.235
84.29	3.0375e+42	2.2306e+42	-17.499	-17.248	-17.031	-17.554	-17.815	-18.033	-18.203	-18.375	-18.503
92.72	4.0579e+42	3.0184e+42	-17.814	-17.664	-17.383	-17.859	-18.110	-18.314	-18.464	-18.630	-18.758
102.00	5.3415e+42	4.0149e+42	-18.112	-18.050	-17.712	-18.146	-18.389	-18.581	-18.715	-18.870	-18.997
112.00	6.8734e+42	5.2077e+42	-18.386	-18.394	-18.009	-18.408	-18.645	-18.829	-18.947	-19.090	-19.215
122.00	8.5088e+42	6.4832e+42	-18.618	-18.679	-18.258	-18.630	-18.861	-19.042	-19.147	-19.278	-19.398
132.00	1.0182e+43	7.7896e+42	-18.813	-18.911	-18.466	-18.817	-19.045	-19.223	-19.319	-19.437	-19.551
142.00	1.1816e+43	9.0680e+42	-18.974	-19.098	-18.637	-18.973	-19.199	-19.378	-19.464	-19.572	-19.677
152.00	1.3333e+43	1.0257e+43	-19.105	-19.241	-18.776	-19.103	-19.328	-19.508	-19.585	-19.685	-19.780
162.00	1.4574e+43	1.1338e+43	-19.202	-19.264	-18.910	-19.280	-19.476	-19.642	-19.672	-19.772	-19.853
172.00	1.5608e+43	1.2171e+43	-19.277	-19.290	-18.988	-19.374	-19.576	-19.740	-19.748	-19.847	-19.916
182.00	1.6339e+43	1.2731e+43	-19.326	-19.271	-19.029	-19.442	-19.654	-19.824	-19.808	-19.908	-19.968
192.00	1.6723e+43	1.2992e+43	-19.351	-19.206	-19.033	-19.485	-19.712	-19.891	-19.849	-19.952	-20.007
211.00	1.6321e+43	1.2504e+43	-19.325	-18.946	-18.920	-19.485	-19.755	-19.956	-19.873	-19.999	-20.051
232.00	1.4259e+43	1.0593e+43	-19.178	-18.465	-18.617	-19.341	-19.668	-19.902	-19.822	-19.998	-20.049
255.00	1.0714e+43	7.5083e+42	-18.868	-17.487	-18.050	-18.991	-19.403	-19.687	-19.684	-19.894	-19.951
280.00	7.4220e+42	4.9189e+42	-18.469	-16.488	-17.413	-18.480	-19.008	-19.372	-19.417	-19.659	-19.726
308.00	5.1085e+42	3.2255e+42	-18.064	-15.741	-16.787	-17.925	-18.575	-19.050	-19.170	-19.355	-19.420
338.00	2.9760e+42	1.9662e+42	-17.477	-15.067	-16.157	-17.303	-17.993	-18.651	-18.520	-18.585	-18.589
371.00	2.0821e+42	1.1506e+42	-17.089	-12.730	-14.573	-16.445	-17.540	-18.301	-18.504	-18.796	-18.364
408.00	1.5414e+42	7.0200e+41	-16.763	-11.737	-13.546	-15.679	-16.950	-17.896	-18.429	-18.752	-18.164
448.80	1.1270e+42	4.3687e+41	-16.423	-11.322	-12.889	-15.005	-16.371	-17.447	-18.214	-18.598	-18.050
493.70	7.7498e+41	3.0059e+41	-16.016	-11.055	-12.425	-14.518	-15.943	-17.060	-17.850	-18.163	-17.612
543.10	4.9505e+41	2.1863e+41	-15.530	-10.741	-11.976	-14.087	-15.596	-16.734	-17.380	-17.374	-16.675

—, 2011b, MNRAS, 415, 3497

Dessart, L., Hillier, D. J., Li, C., & Woosley, S. 2012b, MNRAS, 424, 2139

Dessart, L., Hillier, D. J., Livne, E., Yoon, S.-C., Woosley, S., Waldman, R., & Langer, N. 2011, MNRAS, 565

Dessart, L., Hillier, D. J., Waldman, R., Livne, E., & Blondin, S. 2012c, MNRAS, 426, L76

Dessart, L., O'Connor, E., & Ott, C. D. 2012d, ApJ, 754, 76

Eastman, R. G., Schmidt, B. P., & Kirshner, R. 1996, ApJ, 466, 911

Ensman, L. M. & Woosley, S. E. 1988, ApJ, 333, 754

Falk, S. W. & Arnett, W. D. 1977, ApJS, 33, 515

Figer, D. F., Najarro, F., Gilmore, D., Morris, M., Kim, S. S., Serabyn, E., McLean, I. S., Gilbert, A. M., Graham, J. R., Larkin, J. E., Levenson, N. A., & Teplitz, H. I. 2002, ApJ, 581, 258

Folatelli, G., Contreras, C., Phillips, M. M., Woosley, S. E., Blinnikov, S., & et al. 2006, ApJ, 641, 1039

Gal-Yam, A., Mazzali, P., Ofek, E. O., Nugent, P. E., Kulkarni, S. R., Kasliwal, M. M., Quimby, R. M., & et al. 2009, Nature, 462, 624

Georgy, C., Meynet, G., Walder, R., Folini, D., & Maeder, A. 2009, A&A, 502, 611

Heger, A. & Woosley, S. E. 2002, ApJ, 567, 532

—, 2010, ApJ, 724, 341

Hillier, D. J. 1987, ApJS, 63, 965

Hillier, D. J., Davidson, K., Ishibashi, K., & Gull, T. 2001, ApJ, 553, 837

Hillier, D. J. & Dessart, L. 2012, MNRAS, 424, 252

Hillier, D. J. & Miller, D. L. 1998, ApJ, 496, 407

Hirschi, R. 2007, A&A, 461, 571

Hirschi, R., Meynet, G., & Maeder, A. 2004a, A&A, 425, 649

—, 2004b, A&A, 425, 649

Hosokawa, T., Omukai, K., Yoshida, N., & Yorke, H. W. 2011, Science, 334, 1250

Table D2. Bolometric and UVOIR luminosities as well as synthetic magnitudes for PISN model R190NL.

Age (d)	L_{bol} (erg s ⁻¹)	L_{UVOIR} (erg s ⁻¹)	M_{bol} (mag)	M_{U} (mag)	M_{B} (mag)	M_{V} (mag)	M_{R} (mag)	M_{I} (mag)	M_{J} (mag)	M_{H} (mag)	M_{K} (mag)
36.72	1.3795e+44	4.3057e+43	-21.642	-21.330	-20.380	-20.354	-20.440	-20.374	-20.329	-20.346	-20.454
40.39	1.0017e+44	3.6363e+43	-21.295	-21.066	-20.193	-20.247	-20.348	-20.317	-20.317	-20.348	-20.469
44.43	7.6372e+43	3.2061e+43	-21.000	-20.843	-20.055	-20.176	-20.297	-20.292	-20.333	-20.375	-20.507
48.87	6.1774e+43	2.9380e+43	-20.770	-20.660	-19.958	-20.136	-20.279	-20.292	-20.368	-20.418	-20.558
53.76	5.2790e+43	2.7743e+43	-20.600	-20.509	-19.894	-20.116	-20.283	-20.308	-20.415	-20.472	-20.617
59.14	4.7693e+43	2.6861e+43	-20.489	-20.390	-19.857	-20.114	-20.304	-20.338	-20.472	-20.536	-20.685
65.05	4.4163e+43	2.6210e+43	-20.406	-20.278	-19.827	-20.112	-20.328	-20.370	-20.534	-20.606	-20.758
71.56	4.1327e+43	2.5494e+43	-20.334	-20.160	-19.790	-20.101	-20.347	-20.401	-20.599	-20.684	-20.841
78.72	3.7587e+43	2.4079e+43	-20.231	-19.984	-19.716	-20.056	-20.341	-20.411	-20.654	-20.755	-20.920
86.59	3.3955e+43	2.2317e+43	-20.120	-19.754	-19.616	-19.991	-20.320	-20.413	-20.702	-20.822	-20.999
95.25	3.0894e+43	2.0488e+43	-20.018	-19.491	-19.502	-19.909	-20.284	-20.401	-20.738	-20.878	-21.073
104.00	2.8994e+43	1.9156e+43	-19.949	-19.300	-19.412	-19.825	-20.248	-20.374	-20.749	-20.900	-21.122
114.00	2.5779e+43	1.6759e+43	-19.821	-18.996	-19.247	-19.662	-20.147	-20.265	-20.703	-20.855	-21.111
124.00	2.1881e+43	1.3864e+43	-19.643	-18.562	-19.006	-19.449	-19.995	-20.101	-20.616	-20.759	-21.044
136.00	1.8206e+43	1.1264e+43	-19.444	-18.040	-18.722	-19.235	-19.835	-19.906	-20.491	-20.605	-20.933
150.00	1.5858e+43	9.8104e+42	-19.294	-17.617	-18.512	-19.131	-19.735	-19.766	-20.364	-20.443	-20.791
165.00	1.6326e+43	1.0444e+43	-19.325	-17.749	-18.571	-19.250	-19.793	-19.828	-20.334	-20.419	-20.724
181.00	1.8889e+43	1.2586e+43	-19.484	-18.362	-18.813	-19.461	-19.931	-19.990	-20.388	-20.483	-20.746
199.00	2.2135e+43	1.5332e+43	-19.656	-18.908	-19.058	-19.673	-20.080	-20.155	-20.478	-20.520	-20.749
218.90	2.4176e+43	1.7416e+43	-19.752	-19.229	-19.179	-19.816	-20.181	-20.312	-20.509	-20.434	-20.652
240.80	2.1726e+43	1.6053e+43	-19.636	-19.020	-19.031	-19.747	-20.132	-20.327	-20.306	-20.272	-20.420
264.00	1.4704e+43	1.0458e+43	-19.212	-18.029	-18.347	-19.314	-19.788	-20.038	-19.960	-20.107	-20.212
290.00	8.4332e+42	5.6610e+42	-18.608	-16.730	-17.494	-18.622	-19.171	-19.543	-19.522	-19.757	-19.820
319.00	4.6253e+42	3.0791e+42	-17.956	-15.695	-16.669	-17.858	-18.506	-19.064	-18.915	-19.104	-19.060
350.90	2.8228e+42	1.7351e+42	-17.420	-13.735	-15.362	-16.999	-17.978	-18.674	-18.665	-18.840	-18.545
386.00	1.9654e+42	1.0575e+42	-17.027	-12.129	-14.173	-16.242	-17.434	-18.289	-18.551	-18.723	-18.176
424.60	1.3801e+42	6.3219e+41	-16.643	-11.844	-13.372	-15.471	-16.804	-17.823	-18.352	-18.624	-17.880
467.00	9.9485e+41	3.9880e+41	-16.288	-11.553	-12.780	-14.843	-16.263	-17.359	-18.089	-18.417	-17.823
513.70	6.4897e+41	2.8621e+41	-15.824	-11.402	-12.400	-14.435	-15.894	-17.012	-17.635	-17.752	-17.030
565.00	4.1263e+41	2.0683e+41	-15.332	-11.179	-11.974	-13.990	-15.546	-16.680	-17.128	-16.889	-15.982
621.50	2.5179e+41	1.4186e+41	-14.796	-10.926	-11.484	-13.454	-15.148	-16.295	-16.542	-15.925	-14.811
683.70	1.4502e+41	9.0849e+40	-14.197	-10.580	-10.909	-12.810	-14.678	-15.842	-15.859	-14.876	-13.560
752.10	7.8231e+40	5.5235e+40	-13.527	-10.144	-10.213	-12.202	-14.167	-15.324	-15.121	-13.415	-11.947
827.30	3.9231e+40	2.9709e+40	-12.777	-9.623	-9.482	-11.362	-13.492	-14.689	-14.243	-12.345	-10.831
910.00	1.8103e+40	1.4445e+40	-11.938	-8.989	-8.676	-10.413	-12.699	-13.940	-13.244	-11.334	-9.784
1001.00	7.6570e+39	6.2713e+39	-11.003	-8.277	-7.828	-9.424	-11.785	-13.052	-12.178	-10.366	-8.765

Hummel, J. A., Pawlik, A. H., Milosavljević, M., & Bromm, V. 2012, *ApJ*, 755, 72

Hummer, D. G., Berrington, K. A., Eissner, W., Pradhan, A. K., Saraph, H. E., & Tully, J. A. 1993, *A&A*, 279, 298

Joggerst, C. C. & Whalen, D. J. 2011, *ApJ*, 728, 129

Joss, P. C., Salpeter, E. E., & Ostriker, J. P. 1973, *ApJ*, 181, 429

Kasen, D. & Bildsten, L. 2010, *ApJ*, 717, 245

Kasen, D., Woosley, S. E., & Heger, A. 2011, *ApJ*, 734, 102

Kingdon, J. B. & Ferland, G. J. 1996, *ApJS*, 106, 205

Kirshner, R. P. & Kwan, J. 1974, *ApJ*, 193, 27

Kudritzki, R. P., Pauldrach, A., & Puls, J. 1987, *A&A*, 173, 293

Kurucz, R. L. 2009, in *American Institute of Physics Conference Series*, Vol. 1171, American Institute of Physics Conference Series, ed. I. Hubeny, J. M. Stone, K. MacGregor, & K. Werner, 43–51

Kurucz, R. L. 2010

Langer, N., Norman, C. A., de Koter, A., Vink, J. S., Cantiello, M., & Yoon, S.-C. 2007, *A&A*, 475, L19

Leibowitz, E. M. 1972, *Journal of Quantitative Spectroscopy and Radiative Transfer*, 12, 299

Lennon, D. J. & Burke, V. M. 1994, *A&AS*, 103, 273

Lennon, D. J., Dufton, P. L., Hibbert, A., & Kingston, A. E. 1985, *ApJ*, 294, 200

Leonard, D. C., Filippenko, A. V., Ganeshalingam, M., Serduke, F. J. D., Li, W., Swift, B. J., Gal-Yam, A., Foley, R. J., Fox, D. B., Park, S., Hoffman, J. L., & Wong, D. S. 2006, *Nature*, 440, 505

Li, C., Hillier, D. J., & Dessart, L. 2012, *MNRAS*, 426, 1671

Livne, E. 1993, *ApJ*, 412, 634

Lucy, L. B. 1991, *ApJ*, 383, 308

Luo, D. & Pradhan, A. K. 1989, *Journal of Physics B Atomic Molecular Physics*, 22, 3377

Maeda, K., Tanaka, M., Nomoto, K., Tominaga, N., Kawabata, K., & et al. 2007, *ApJ*, 666, 1069

Maeder, A. & Meynet, G. 2000, *A&A*, 361, 159

Maguire, K., Jerkstrand, A., Smartt, S. J., Fransson, C., Pastorello, A., Benetti, S., Valenti, S., Bufano, F., & Leloudas, G. 2012, *MNRAS*, 420, 3451

Martins, F., Hillier, D. J., Paumard, T., Eisenhauer, F., Ott, T., & Genzel, R. 2008, *A&A*, 478, 219

Mendoza, C. 1983, in *IAU Symposium*, Vol. 103, Planetary Nebulae, ed. D. R. Flower, 143–172

Moriya, T., Tominaga, N., Tanaka, M., Maeda, K., & Nomoto, K.

Table D3. Bolometric and UVOIR luminosities as well as synthetic magnitudes for PISN model B210NL

Age (d)	L_{bol} (erg s ⁻¹)	L_{UVOIR} (erg s ⁻¹)	M_{bol} (mag)	M_{U} (mag)	M_{B} (mag)	M_{V} (mag)	M_{R} (mag)	M_{I} (mag)	M_{J} (mag)	M_{H} (mag)	M_{K} (mag)
16.80	2.8082e+42	1.7870e+42	-17.414	-15.893	-16.499	-17.346	-17.905	-17.961	-18.404	-18.519	-18.822
18.48	2.4868e+42	1.5465e+42	-17.282	-15.344	-16.264	-17.196	-17.785	-17.864	-18.346	-18.464	-18.783
20.33	2.2713e+42	1.3845e+42	-17.184	-14.879	-16.090	-17.080	-17.677	-17.792	-18.295	-18.416	-18.740
22.36	2.1097e+42	1.2687e+42	-17.104	-14.625	-15.982	-16.974	-17.582	-17.719	-18.240	-18.365	-18.688
24.60	1.9644e+42	1.1713e+42	-17.026	-14.490	-15.904	-16.881	-17.491	-17.639	-18.178	-18.308	-18.622
27.10	1.8524e+42	1.1017e+42	-16.962	-14.421	-15.865	-16.813	-17.413	-17.574	-18.121	-18.259	-18.559
29.81	1.7287e+42	1.0242e+42	-16.887	-14.350	-15.817	-16.721	-17.329	-17.495	-18.051	-18.202	-18.491
32.79	1.7152e+42	1.0362e+42	-16.879	-14.460	-15.856	-16.762	-17.325	-17.494	-18.031	-18.141	-18.421
36.07	2.0198e+42	1.2960e+42	-17.056	-15.322	-16.131	-17.068	-17.527	-17.684	-18.110	-18.214	-18.452
39.68	2.6317e+42	1.7885e+42	-17.344	-16.396	-16.587	-17.421	-17.777	-17.924	-18.263	-18.408	-18.585
43.65	3.6298e+42	2.5640e+42	-17.693	-17.200	-17.073	-17.773	-18.064	-18.213	-18.499	-18.659	-18.807
48.01	5.0858e+42	3.6894e+42	-18.059	-17.824	-17.547	-18.121	-18.370	-18.517	-18.768	-18.931	-19.063
52.81	7.1644e+42	5.2956e+42	-18.431	-18.370	-17.999	-18.467	-18.687	-18.825	-19.048	-19.208	-19.329
58.09	9.9973e+42	7.4758e+42	-18.793	-18.861	-18.417	-18.797	-18.997	-19.121	-19.325	-19.475	-19.590
63.90	1.3780e+43	1.0351e+43	-19.141	-19.307	-18.797	-19.111	-19.298	-19.407	-19.597	-19.732	-19.843
70.29	1.8721e+43	1.4037e+43	-19.474	-19.711	-19.141	-19.408	-19.587	-19.686	-19.864	-19.980	-20.085
77.32	2.5052e+43	1.8614e+43	-19.790	-20.067	-19.452	-19.690	-19.866	-19.954	-20.126	-20.223	-20.319
85.05	3.3223e+43	2.4331e+43	-20.097	-20.394	-19.736	-19.962	-20.142	-20.219	-20.382	-20.460	-20.542
93.56	4.3745e+43	3.1614e+43	-20.395	-20.719	-20.009	-20.228	-20.412	-20.480	-20.624	-20.683	-20.751
102.00	5.5049e+43	3.9495e+43	-20.645	-20.995	-20.241	-20.454	-20.639	-20.706	-20.827	-20.868	-20.927
112.00	6.8640e+43	4.9270e+43	-20.885	-21.263	-20.477	-20.682	-20.865	-20.934	-21.026	-21.051	-21.101
122.00	8.1394e+43	5.8866e+43	-21.070	-21.471	-20.671	-20.868	-21.051	-21.123	-21.193	-21.200	-21.242
132.00	9.0999e+43	6.7721e+43	-21.191	-21.626	-20.831	-21.024	-21.206	-21.278	-21.330	-21.316	-21.356
142.00	9.9900e+43	7.5971e+43	-21.292	-21.747	-20.968	-21.154	-21.336	-21.404	-21.440	-21.403	-21.439
156.00	1.0871e+44	8.5119e+43	-21.384	-21.850	-21.118	-21.296	-21.473	-21.532	-21.544	-21.468	-21.503
171.00	1.1360e+44	9.1407e+43	-21.432	-21.873	-21.240	-21.418	-21.577	-21.621	-21.591	-21.476	-21.497
188.00	1.1249e+44	9.2770e+43	-21.421	-21.757	-21.304	-21.530	-21.658	-21.674	-21.552	-21.420	-21.399
207.00	1.0145e+44	8.4987e+43	-21.309	-21.362	-21.173	-21.563	-21.721	-21.725	-21.387	-21.329	-21.209
227.00	8.2998e+43	6.8282e+43	-21.091	-20.638	-20.732	-21.424	-21.669	-21.764	-21.131	-21.375	-21.172
249.00	6.2501e+43	4.8175e+43	-20.783	-19.744	-20.100	-21.052	-21.402	-21.641	-20.986	-21.474	-21.250
273.90	4.7246e+43	3.3740e+43	-20.479	-18.700	-19.510	-20.610	-21.069	-21.460	-20.955	-21.445	-21.193
301.30	3.6861e+43	2.4050e+43	-20.210	-17.791	-18.959	-20.155	-20.744	-21.227	-21.109	-21.474	-21.290
331.40	2.4510e+43	1.6278e+43	-19.766	-17.175	-18.460	-19.670	-20.304	-20.901	-20.665	-20.942	-20.625
331.40	2.4371e+43	1.6453e+43	-19.760	-17.516	-18.467	-19.627	-20.293	-20.940	-20.685	-20.864	-20.575
364.50	1.6297e+43	1.1526e+43	-19.323	-16.990	-17.944	-19.133	-19.916	-20.659	-20.243	-20.270	-19.774
401.00	1.1467e+43	8.4434e+42	-18.942	-16.434	-17.419	-18.704	-19.617	-20.388	-19.953	-19.815	-19.169
441.10	7.9475e+42	5.7846e+42	-18.544	-15.721	-16.647	-18.145	-19.241	-20.065	-19.759	-19.545	-18.684
485.20	5.6956e+42	3.8594e+42	-18.182	-15.033	-15.792	-17.542	-18.803	-19.720	-19.604	-19.458	-18.379
645.80	1.0517e+42	5.9927e+41	-16.348	-12.727	-13.115	-15.085	-16.787	-17.795	-18.048	-17.577	-16.151

2010, ApJL, 717, L83

Nahar, S. N. 1995, A&A, 293, 967

—. 2010, NORAD-Atomic-Data

Nahar, S. N. & Pradhan, A. K. 1993, Journal of Physics B Atomic Molecular Physics, 26, 1109

—. 1996, A&AS, 119, 509

Nomoto, K., Tominaga, N., Umeda, H., Kobayashi, C., & Maeda, K. 2006, Nuclear Physics A, 777, 424

Nussbaumer, H. & Storey, P. J. 1983, A&A, 126, 75

—. 1984, A&AS, 56, 293

Ofek, E. O., Cameron, P. B., Kasliwal, M. M., Gal-Yam, A., Rau, A., Kulkarni, S. R., Frail, D. A., Chandra, P., Cenko, S. B., Soderberg, A. M., & Immler, S. 2007, ApJL, 659, L13

Osterbrock, D. E. 1989, Astrophysics of gaseous nebulae and active galactic nuclei

Owocki, S. P., Gayley, K. G., & Shaviv, N. J. 2004, ApJ, 616, 525

Pan, T., Kasen, D., & Loeb, A. 2012a, MNRAS, 422, 2701

Pan, T., Loeb, A., & Kasen, D. 2012b, MNRAS, 423, 2203

Pastorello, A., Sauer, D., Taubenberger, S., Mazzali, P. A.,

Nomoto, K., Kawabata, K. S., Benetti, S., Elias-Rosa, N., Harutyunyan, A., Navasardyan, H., Zampieri, L., Iijima, T., Botticella, M. T., Di Rico, G., Del Principe, M., Dolci, M., Gagliardi, S., Ragni, M., & Valentini, G. 2006, MNRAS, 370, 1752

Paxton, B., Bildsten, L., Dotter, A., Herwig, F., Lesaffre, P., & Timmes, F. 2011, ApJS, 192, 3

Peach, G., Saraph, H. E., & Seaton, M. J. 1988, Journal of Physics B Atomic Molecular Physics, 21, 3669

Quimby, R. M., Kulkarni, S. R., Kasliwal, M. M., Gal-Yam, A., Arcavi, I., & et al. 2011, Nature, 474, 487

Quimby, R. M., Wheeler, J. C., Höflich, P., Akerlof, C. W., Brown, P. J., & Rykoff, E. S. 2007, ApJ, 666, 1093

Rakavy, G. & Shaviv, G. 1967, ApJ, 148, 803

Scannapieco, E., Madau, P., Woosley, S., Heger, A., & Ferrara, A. 2005, ApJ, 633, 1031

Scannapieco, E., Schneider, R., & Ferrara, A. 2003, ApJ, 589, 35

Seaton, M. J. 1987, Journal of Physics B Atomic Molecular Physics, 20, 6363

—. 1998, MNRAS, 300, L1

Table D4. Bolometric and UVOIR luminosities as well as synthetic magnitudes for PISN model He100ionINL.

Age (d)	L_{bol} (erg s ⁻¹)	L_{UVOIR} (erg s ⁻¹)	M_{bol} (mag)	M_{U} (mag)	M_{B} (mag)	M_{V} (mag)	M_{R} (mag)	M_{I} (mag)	M_{J} (mag)	M_{H} (mag)	M_{K} (mag)
11.55	3.8088e+41	2.4709e+41	-15.245	-14.431	-14.649	-15.228	-15.529	-15.811	-16.213	-16.496	-16.632
12.71	4.0804e+41	2.6687e+41	-15.320	-14.324	-14.760	-15.332	-15.631	-15.902	-16.317	-16.611	-16.750
13.98	4.4089e+41	2.8803e+41	-15.404	-14.359	-14.834	-15.418	-15.717	-15.996	-16.415	-16.720	-16.850
15.38	4.7409e+41	3.0781e+41	-15.483	-14.392	-14.887	-15.495	-15.798	-16.083	-16.514	-16.827	-16.942
16.92	5.0436e+41	3.2326e+41	-15.550	-14.355	-14.917	-15.556	-15.870	-16.157	-16.613	-16.935	-17.036
18.61	5.3148e+41	3.3305e+41	-15.607	-14.207	-14.922	-15.598	-15.931	-16.218	-16.716	-17.051	-17.142
20.47	5.1565e+41	3.0544e+41	-15.574	-13.646	-14.761	-15.505	-15.886	-16.202	-16.774	-17.130	-17.225
22.52	4.6197e+41	2.4974e+41	-15.455	-12.646	-14.403	-15.264	-15.719	-16.098	-16.766	-17.151	-17.268
24.77	4.2201e+41	2.0684e+41	-15.356	-11.833	-14.031	-15.005	-15.546	-16.000	-16.760	-17.167	-17.315
27.25	4.1484e+41	1.8889e+41	-15.338	-11.393	-13.795	-14.849	-15.463	-15.975	-16.800	-17.217	-17.393
29.98	4.5362e+41	2.0219e+41	-15.435	-11.333	-13.814	-14.903	-15.543	-16.068	-16.913	-17.331	-17.518
32.99	5.5622e+41	2.5671e+41	-15.656	-11.642	-14.116	-15.193	-15.801	-16.291	-17.106	-17.521	-17.701
36.29	7.4467e+41	3.7020e+41	-15.973	-12.327	-14.628	-15.649	-16.185	-16.613	-17.358	-17.764	-17.923
39.92	1.0462e+42	5.6987e+41	-16.342	-13.543	-15.244	-16.165	-16.620	-16.981	-17.634	-18.026	-18.153
43.91	1.4940e+42	8.8947e+41	-16.729	-14.972	-15.857	-16.664	-17.043	-17.342	-17.907	-18.280	-18.376
48.30	2.1214e+42	1.3572e+42	-17.110	-16.011	-16.404	-17.119	-17.433	-17.681	-18.168	-18.524	-18.592
53.13	2.9774e+42	2.0116e+42	-17.478	-16.779	-16.898	-17.533	-17.798	-18.003	-18.419	-18.765	-18.805
58.44	4.1165e+42	2.8960e+42	-17.829	-17.396	-17.350	-17.909	-18.137	-18.306	-18.661	-18.999	-19.015
64.28	5.5664e+42	4.0347e+42	-18.157	-17.873	-17.758	-18.256	-18.457	-18.592	-18.899	-19.216	-19.220
70.71	7.4557e+42	5.5287e+42	-18.474	-18.337	-18.136	-18.572	-18.754	-18.864	-19.130	-19.430	-19.424
77.78	9.8045e+42	7.3869e+42	-18.772	-18.748	-18.474	-18.860	-19.029	-19.124	-19.359	-19.639	-19.623
85.56	1.2666e+43	9.6485e+42	-19.050	-19.115	-18.777	-19.124	-19.285	-19.373	-19.584	-19.841	-19.818
94.12	1.6074e+43	1.2345e+43	-19.308	-19.438	-19.050	-19.368	-19.526	-19.615	-19.803	-20.032	-20.006
103.50	1.9896e+43	1.5376e+43	-19.540	-19.705	-19.293	-19.589	-19.748	-19.844	-20.006	-20.205	-20.182
113.90	2.4051e+43	1.8705e+43	-19.746	-19.922	-19.512	-19.790	-19.956	-20.056	-20.191	-20.349	-20.340
125.30	2.8126e+43	2.1992e+43	-19.916	-20.065	-19.700	-19.973	-20.142	-20.244	-20.351	-20.473	-20.474
137.80	3.1465e+43	2.4699e+43	-20.038	-20.101	-19.836	-20.128	-20.304	-20.407	-20.474	-20.561	-20.573
151.60	3.3367e+43	2.6215e+43	-20.101	-20.008	-19.887	-20.238	-20.432	-20.545	-20.550	-20.616	-20.637
166.80	3.2851e+43	2.5632e+43	-20.085	-19.741	-19.790	-20.272	-20.501	-20.645	-20.561	-20.651	-20.670
183.50	2.9521e+43	2.2540e+43	-19.968	-19.291	-19.517	-20.188	-20.463	-20.652	-20.504	-20.670	-20.680
201.90	2.4249e+43	1.7783e+43	-19.755	-18.653	-19.089	-19.970	-20.296	-20.540	-20.382	-20.662	-20.669
222.10	1.8562e+43	1.2748e+43	-19.465	-17.772	-18.535	-19.611	-20.001	-20.335	-20.276	-20.625	-20.637
244.30	1.3665e+43	8.6887e+42	-19.132	-16.763	-17.921	-19.141	-19.631	-20.064	-20.171	-20.515	-20.528
268.70	9.8105e+42	5.8724e+42	-18.772	-15.845	-17.315	-18.618	-19.229	-19.768	-19.980	-20.275	-20.280
295.60	7.0062e+42	4.0058e+42	-18.407	-14.530	-16.574	-18.024	-18.858	-19.512	-19.756	-19.943	-19.930
325.20	5.1579e+42	2.9173e+42	-18.074	-13.678	-15.976	-17.526	-18.517	-19.266	-19.536	-19.565	-19.545
357.70	3.8206e+42	2.1646e+42	-17.748	-13.057	-15.354	-17.030	-18.180	-19.033	-19.311	-19.220	-19.095
393.50	2.7860e+42	1.5224e+42	-17.406	-12.583	-14.638	-16.490	-17.786	-18.740	-19.044	-18.961	-18.641
432.90	1.9716e+42	9.6298e+41	-17.030	-12.173	-13.989	-15.826	-17.265	-18.306	-18.727	-18.776	-18.224
476.20	1.3480e+42	5.8865e+41	-16.617	-11.785	-13.451	-15.171	-16.724	-17.770	-18.399	-18.288	-17.846
523.80	8.3169e+41	3.6854e+41	-16.093	-11.441	-13.000	-14.608	-16.224	-17.256	-17.869	-17.442	-17.066
576.20	4.9389e+41	2.2191e+41	-15.527	-11.048	-12.511	-14.036	-15.685	-16.693	-17.273	-16.518	-16.173
633.80	2.7777e+41	1.2231e+41	-14.902	-10.618	-11.972	-13.398	-15.044	-16.029	-16.626	-15.610	-15.245
697.20	1.4668e+41	6.0678e+40	-14.209	-10.131	-11.369	-12.681	-14.274	-15.251	-15.931	-14.773	-14.267
766.90	7.4843e+40	2.7223e+40	-13.479	-9.560	-10.688	-11.886	-13.385	-14.359	-15.217	-14.035	-13.202

Shine, R. A. & Linsky, J. L. 1974, *Sol. Phys.*, 39, 49
 Smith, N., Chornock, R., Silverman, J. M., Filippenko, A. V., & Foley, R. J. 2010, *ApJ*, 709, 856
 Smith, N., Li, W., Foley, R. J., Wheeler, J. C., Pooley, D., Chornock, R., Filippenko, A. V., Silverman, J. M., Quimby, R., Bloom, J. S., & Hansen, C. 2007, *ApJ*, 666, 1116
 Spencer, L. V. & Fano, U. 1954, *Physical Review*, 93, 1172
 Stacy, A., Bromm, V., & Loeb, A. 2011, *MNRAS*, 413, 543
 Stacy, A., Greif, T. H., & Bromm, V. 2010, *MNRAS*, 403, 45
 —. 2012, *MNRAS*, 2508
 Tayal, S. S. 1997a, *ApJS*, 111, 459
 —. 1997b, *ApJ*, 481, 550
 Tayal, S. S. & Henry, R. J. W. 1996, *Journal of Physics B Atomic*

Molecular Physics, 29, 3443
 Umeda, H. & Nomoto, K. 2002, *ApJ*, 565, 385
 Utrobin, V. P. 2007, *A&A*, 461, 233
 Utrobin, V. P. & Chugai, N. N. 2005, *A&A*, 441, 271
 Vanbeveren, D., Belkus, H., van Bever, J., & Mennekens, N. 2009, *Ap&SS*, 324, 271
 Vink, J. S., de Koter, A., & Lamers, H. J. G. L. M. 2001, *A&A*, 369, 574
 Waldman, R. 2008, *ApJ*, 685, 1103
 Woosley, S. E. 1993, *ApJ*, 405, 273
 —. 2010, *ApJL*, 719, L204
 Woosley, S. E., Blinnikov, S., & Heger, A. 2007a, *Nature*, 450, 390

- . 2007b, *Nature*, 450, 390
- Woosley, S. E. & Heger, A. 2006, *Astrophys. J.*, 637, 914
- Yoon, S.-C., Dierks, A., & Langer, N. 2012, *A&A*, 542, A113
- Young, D. R., Smartt, S. J., Valenti, S., Pastorello, A., Benetti, S.,
Benn, C. R., Bersier, D., & et al. 2010, *A&A*, 512, A70
- Zhang, H. L. & Pradhan, A. K. 1995a, *A&A*, 293, 953
- . 1995b, *Journal of Physics B Atomic Molecular Physics*, 28,
3403
- . 1997, *A&AS*, 126, 373